Experimental closed-loop control of SCR aftertreatment systems using NOx sensors cross-sensitive to NH3

Anthony Bonfils

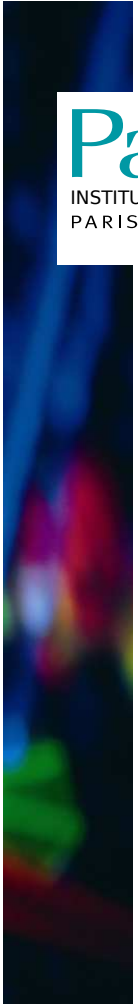

ParisTech
INSTITUT DES SCIENCES ET TECHNOLOGIES
PARIS INSTITUTE OF TECHNOLOGY

MINES ParisTech

École doctorale n°432 : Sciences des Métiers de l'Ingénieur

Doctorat ParisTech

PhD THESIS

to obtain the Doctor's degree from

l'École nationale supérieure des mines de Paris

Specialty "Mathematics and Control"

defended in public by

Anthony BONFILS

December 11th, 2013

Experimental closed-loop control of SCR aftertreatment systems using NO_x sensors cross-sensitive to NH_3

Commande expérimentale en boucle fermée des systèmes de post-traitement SCR en utilisant des sondes à NO_x sensibles au NH_3

Advisor: **M. Nicolas PETIT**
Supervisor: **M. Yann CREFF**

Committee

M. Jean-Pierre CORRIOU, Professor, LRGP-CNRS, ENSIC	Referee
M. Yann LE GORREC, Professor, FEMTO-ST/AS2M, ENSMM	Referee
Mme Madiha NADRI WOLF, Associate professor, LAGEP, UCBL	Examiner
M. Nicolas PETIT, Professor, CAS, MINES ParisTech	Examiner
M. Yann CREFF, Doctor, IFPEN	Examiner

THÈSE

MINES ParisTech
Centre Automatique et Systèmes, Unité Mathématiques et Systèmes
60 Bd Saint-Michel, 75006 Paris

Résumé

Le problème étudié dans cette thèse est la commande en boucle fermée d'un système SCR (Réduction Sélective Catalytique) par l'urée tel qu'utilisé dans les systèmes de dépollution des gaz d'échappement des moteurs diesel automobiles.

Une première contribution du manuscrit est en un modèle détaillé de la SCR, soulignant de la nature distribuée (1D) du système considéré, et plusieurs réductions successives de ce modèle de simulation conduisant à un modèle plus simple, utilisable à des fins de synthèse de contrôleur.

Une seconde contribution consiste à prendre en compte la sensibilité au NH_3 du capteur de NO_x utilisé pour la rétroaction lors du développement d'algorithmes de commande (observateur d'état, boucle de rétroaction, séquencement de gain, interprétation du signal capteur). L'observateur-contrôleur présenté possède plusieurs points d'équilibre dues à la sensibilité du capteur de sortie. On montre que seul le point d'intérêt pratique est asymptotiquement stable, les autres étant instables naturellement, rendus instables par une implémentation spécifique ou aisément détectés comme indésirables.

Ces deux contributions ont été testées expérimentalement et validées. En résumé, la méthode de contrôle proposée dans cette thèse permet, à partir d'un moteur conforme aux exigences Euro 5 et avec une procédure de pré-conditionnement du catalyseur, de satisfaire la norme Euro 6.

Mots-clefs Commande en boucle fermée, observateur, émissions automobiles, moteur diesel, Réduction Sélective Catalytique par l'urée, sonde à NO_x, sensibilité croisée.

Summary

The problem studied in this thesis is the closed-loop control of a urea-SCR (urea Selective Catalytic Reduction) as used in aftertreatment systems of diesel vehicles.

A first contribution of the thesis is a detailed model for the SCR, highlighting the distributed (1D) nature of the considered system, and several successive reductions of this simulation model leading to a simpler one, better-suited for control design purposes.

A second contribution consists in considering the sensitivity to NH_3 of the NO_x sensor used in a feedback loop, in the development of the control algorithms (state observer, feedback, gain scheduling, measurement interpretation). The ambiguity of the output measurement could be detrimental to the closed loop response, as it generates multiple equilibrium points (artefacts), besides the point of practical interest. A study of the closed-loop dynamics is performed in the vicinity of each point, which shows that the closed loop system naturally converges to the point of interest not to the artefacts.

Both contributions have been tested and validated experimentally. In summary, the method proposed in this thesis might allow an engine equipped with Euro 5 hardware to satisfy Euro 6 standard using a preconditioning procedure of the catalyst.

Keywords Closed-loop control, observer, automotive emissions, diesel engines, urea Selective Catalytic Reduction, NO_x sensor, cross-sensitivity.

Remerciements

En tout premier lieu, je souhaite remercier mes encadrants de thèse, Nicolas Petit et Yann Creff. Nicolas, mon directeur de thèse, pour ses conseils scientifiques, son soutien, sa disponibilité et sa grande réactivité. Je le remercie également pour l'intérêt et l'enthousiasme dont il a fait preuve face aux idées et travaux qui lui ont été soumis, ainsi que pour la confiance et les conseils qu'il m'a apportés pendant ces trois ans. Yann, mon encadrant et le promoteur de cette thèse, pour m'avoir poussé devant les difficultés et pour son soutien inconditionnel. Son intérêt et son implication, ainsi que son expertise scientifique et technique ont été une contribution inestimable à la qualité et à l'aboutissement de mes travaux. Merci à tous les deux pour votre patience et vos encouragements, j'ai énormément appris pendant cette thèse et surtout en travaillant avec vous.

J'exprime ma gratitude à Messieurs Jean-Pierre Corriou et Yann Le Gorrec, rapporteurs de ma thèse, pour l'intérêt qu'ils ont montré pour mes travaux et pour leurs commentaires avisés sur mon mémoire et lors de ma présentation. Je remercie Madame Madiha Nadri Wolf, examinatrice, de m'avoir fait l'honneur d'évaluer mes travaux.

J'adresse également mes sincères remerciements à tous les collègues de R105 et R113 qui ont contribué à la mise en oeuvre et à la réussite de ce projet. Merci notamment à Olivier Lepreux, Luc Voise, Arnaud Frobert, Stéphane Raux, François Kerdelhue, Bruno Bourry, Carole Querel, Olivier Grondin, Jacques Lavy, Charlotte Kieffer et David Berthout pour la réussite de ces travaux et des essais.

Merci aux collègues que j'ai côtoyés quotidiennement et qui ont contribué à rendre ce travail convivial et agréable. Je pense notamment à Mimmo, Paolo, Philippe, Matthieu, Bilal, Florent, Maxime, Daniel et Florian. Merci aux doctorants, post-doctorants (actuels et anciens), et notamment à Johan, Viet-Dung, François, Matthieu et Jérémy.

Enfin, merci à tous les proches qui m'ont encouragé dans ce travail et sans qui

je n'en serais pas là aujourd'hui, mes parents, grand-parents, toute ma famille et belle-famille. Je remercie Isabelle pour sa patience, sa compréhension et son soutien inconditionnel et mon fils Axel, ma joie de vivre.

Introduction générale

Parmi les polluants les plus nocifs produits par les moteurs diesel, figurent les oxydes d'azote (NO_x). Les nombreux développements technologiques des moteurs au cours des vingt dernières années ont permis de limiter considérablement les émissions de NO_x des véhicules particuliers diesel. Cependant, les futures réglementations (normes d'émissions) s'avérant de plus en plus strictes, on considère que ces efforts seront insuffisants à l'avenir et qu'il sera indispensable de recourir à des systèmes de dépollution (post-traitement) dédiés. Parmi les technologies possibles pour lutter contre les NO_x, la réduction catalytique sélective par l'urée (SCR à l'urée) est l'une des approches les plus intéressantes. En effet, par rapport à l'alternative principale, le piège à NO_x (Lean NO_x Trap, LNT), la SCR par l'urée permet de traiter de grandes quantités de NO_x à un coût relativement faible.

La SCR par l'urée utilise un long catalyseur tubulaire parcouru par les gaz d'échappement du moteur diesel. On utilise de l'ammoniac (NH_3) comme agent réducteur, ce dernier étant généré par la décomposition d'une solution d'urée injectée dans la ligne d'échappement, en amont du catalyseur. Les molécules de NH_3 sont adsorbées sur la surface catalytique, et réagissent avec les NO_x contenus dans les gaz d'échappement. La quantité totale de NH_3 adsorbé, également appelée couverture, est régie par les flux d'entrée de NH_3 passés et est influencée par l'évolution de la température (variations subies, imposées par l'utilisation du moteur). Le rôle de la stratégie de commande dans un système SCR est de maintenir constamment en adéquation la valeur de la couverture du catalyseur (variable non mesurée) et la valeur instantanée de NO_x présents à l'entrée du catalyseur (polluants à traiter), en prenant en compte que l'efficacité de traitement obtenue est une fonction de la température. Dans le langage du contrôle des systèmes, la quantité de NO_x à traiter, la température des gaz d'échappement et leur vitesse sont des perturbations mesurées et bornées, la couverture est une variable d'état gouvernée par la commande qu'est le débit d'injection de NH_3. La mesure utilisable en boucle fermée est délivrée par un capteur de NO_x situé à la sortie du catalyseur SCR. On recherche, en boucle fermée, à assurer une bonne efficacité de traitement (conversion des NO_x) tout en limitant les émissions de NH_3 dans l'atmosphère (NH_3-slip).

À première vue, on pourrait imaginer que la configuration décrite ci-dessus est

suffisante pour aisément piloter la couverture en NH_3 adsorbé et ainsi garantir un fonctionnement optimal de la SCR. Malheureusement, les capteurs NO_x disponibles industriellement (en fabrication série) sont tous sensibles à la concentration de NH_3. Cela devient naturellement critique lorsque du NH_3 est présent en sortie du catalyseur SCR, par exemple lorsque la réaction de réduction se passe mal. Les conséquences de l'utilisation de tels capteurs dans des stratégies de contrôle de la SCR à l'urée n'ont pas été étudiées jusqu'ici. C'est le sujet de cette thèse.

La thèse propose une stratégie de commande pour les systèmes SCR, utilisant un observateur de la couverture, mis en cascade avec un contrôleur dont l'objectif est d'atteindre une cible dépendant de la température (afin de prévenir un risque de désorption subi). Comme discuté, l'utilisation du signal de capteur NO_x engendre des difficultés spécifiques. La mesure est ambiguë : deux valeurs de l'état sont possibles pour une mesure donnée. Un observateur de Luenberger classique peut devenir instable, ce qui naturellement remet en cause la stabilité de l'ensemble du système en boucle fermée. Ce problème n'a pas été étudié jusqu'à présent, car les travaux dans ce domaine ne considèrent pas l'usage de capteurs industriels, mais supposent disponibles des capteurs idéaux mesurant seulement les NO_x. La stratégie de commande proposée utilise la mesure du capteur de NO_x en aval du SCR pour estimer la couverture en NH_3 par un observateur d'état (composé de la dynamique du système en boucle ouverte avec injection de sortie). Ensuite un contrôleur est utilisé pour forcer l'estimation de la couverture à suivre une consigne (calculée pour toutes les conditions opératoires). L'observateur-contrôleur ainsi défini possède plusieurs points d'équilibre. On montre que seul le point d'intérêt pratique est asymptotiquement stable, les autres étant instables naturellement, rendus instables par une implémentation spécifique ou aisément détectés comme indésirables.

Des résultats expérimentaux obtenus pendant cette thèse montrent les bonnes performances de la stratégie au travers de campagnes d'essais représentatives des besoins industriels. Plus précisément, deux cycles NEDC avec démarrage à chaud sont réalisés avec deux catalyseurs différents (zéolites échangées au Fer et au Cuivre). Ils permettent d'établir qu'avec la méthode de contrôle proposée dans cette thèse nous sommes en mesure, à partir d'un moteur conforme aux exigences Euro 5 et avec une procédure de pré-conditionnement du catalyseur, de satisfaire la norme Euro 6.

Aperçu de la thèse Le manuscrit est organisé comme suit. Dans le chapitre 1, après avoir rappelé le cadre normatif relatif à l'usage des moteurs diesel, une description physico-chimique du système SCR est présentée. Dans la suite du chapitre, un modèle détaillé de la SCR est exposé en utilisant les résultats de la littérature, puis analysé afin de souligner certains aspects liés à la nature distribuée (1D) du

système considéré. Plusieurs réductions successives du modèle de simulation sont proposées et conduisent à un modèle plus simple, utilisable à des fins de synthèse de contrôleur. Dans le chapitre 2, on expose les principales difficultés rencontrées lors de la définition de la stratégie de commande. On décrit la technologie des capteurs existants et on en déduit un modèle du capteur. On explique ensuite le choix de la valeur cible de la couverture. Au chapitre 3, on expose la stratégie de commande proposée dans la thèse. Elle est basée sur une dynamique en boucle fermée couplée à une équation algébrique (définissant le contrôleur stabilisant). On étudie les propriétés de stabilisation. Le schéma de contrôle proposé tient compte de perturbations mesurées : variations des NO_x amont, variations de la vitesse des gaz d'échappement et conditions de température. Une règle simple de calibration obtenue à partir de l'analyse de la stabilité en boucle fermée est proposée. Pour valider la pertinence de l'approche, les résultats expérimentaux de l'application de la commande sont présentés dans le chapitre 4. Enfin, des extensions sont détaillées dans le chapitre 5.

Les travaux de cette thèse ont fait l'objet de publications :

- **Journaux internationaux avec comité de lecture**

  1. A. Bonfils, Y. Creff, O. Lepreux, & N. Petit. Closed-loop control of a SCR system using a NO_x sensor cross-sensitive to NH_3. *Journal of Process Control*, 2013. To appear, DOI : 10.1016/j.jprocont.2013.08.010.

- **Conférences internationales avec comité de lecture**

  1. A. Bonfils, Y. Creff, O. Lepreux, & N. Petit. Closed-loop control of a SCR system using a NO_x sensor cross-sensitive to NH_3. In *Advanced Control of Chemical Processes*, pages 738–743, 2012.
  2. C. Quérel, A. Bonfils, O. Grondin, & Y. Creff. Control of a SCR system using a virtual NO_x sensor. In *7^{th} IFAC Symposium on Advances in Automotive Control*, Tokyo, Japan, Sept. 4-7, 2013.

General introduction

Numerous recent technological developments have yielded substantial improvements in terms of nitrogen oxides (NO_x) emissions for passenger cars using diesel engines. To meet the future and more stringent emission standards, the use of dedicated aftertreatment devices will be required. Among the variety of encountered technologies, the urea selective catalytic reduction (urea-SCR) is one of the most appealing approaches. Indeed, compared to its main alternative, which is the lean NO_x trap (LNT), the urea-SCR can treat larger amounts of NO_x at a reasonable cost.

The urea-SCR requires the use of an elongated tubular catalyst fed by the exhaust gas flowing out from the diesel engine. The system considered in this thesis uses ammonia (NH_3) as the reducing agent, which is generated by the decomposition of an urea solution, injected in the exhaust line, upstream of the catalyst. The molecules of NH_3 adsorbed onto the catalytic surface react with NO_x coming from the exhaust gases. The amount of adsorbed NH_3, also called coverage ratio, depends on histories of the NH_3 input flow and is influenced by the uncontrolled changes in temperature (variations driven by the engine). The role of the control strategy for the SCR system is to match constantly the value of catalyst coverage ratio (unmeasured variable) and the instantaneous value of inlet NO_x (pollutants to be treated), keeping in mind that a target for the efficiency has to be defined by temperature. The amount of inlet NO_x, the temperature of the exhaust gases as well as their velocity are bounded and measured disturbances. The coverage ratio is a state variable governed by a control: the injection of NH_3. The measurement used in the closed-loop control is a NO_x sensor located at the outlet of the SCR catalyst. In closed-loop, it is desired to guarantee a high level of NO_x reduction while limiting NH_3 emissions into the atmosphere (NH_3-slip).

One can imagine that this setup should allow easy control solutions for the control of the coverage ratio and thus ensure an optimum operation of the SCR. Unfortunately, a particular difficulty is that available embedded NO_x sensors are cross-sensitive to NH_3. This becomes critical when NH_3 is present downstream of the SCR catalyst. The aftereffects of their use in feedback control strategies have not been fully discussed so far. In this thesis, this topic is addressed.

The thesis proposes a control method for SCR systems using an observer of the coverage ratio, cascaded on a controller seeking to reach a temperature-dependent target to prevent the risk of undesirable desorption. In the case of a standard observer-controller scheme, the use of the NO_x sensor signal would induce problems of stability. Due to the ambiguity of the measurement (two values of the state variable can correspond to the same output measurement), the observer may become unstable. In the literature, the aftereffects on the stability of the closed-loop system have not been investigated so far. Rather, research works in this area do not consider industrial sensors in their setup, and use ideal (non cross-sensitive) sensors. The proposed strategy uses the NO_x sensor measurement to estimate the NH_3 coverage ratio by a state observer (open loop dynamics with output injection). The estimate of the coverage ratio is dynamically forced by the control to track a set point (calculated for each operating condition). Measurement errors induce observer bias, that can be limited by a proper choice of the gains, resulting from a scheduling methodology. Additionally, a mechanism is introduced to prevent large NH_3-slip that could result from misinterpretation of data produced by the sensor.

Finally, experimental results are presented and show the good performance of this strategy over a range of scenarios covering realistic application needs. More specifically, two warm start NEDC cycles are performed with two different catalysts (Fe-zeolite and Cu-zeolite). We consider that the method proposed in this thesis might allow an engine equipped with Euro 5 hardware to satisfy Euro 6 standard using a preconditioning procedure of the catalyst.

Thesis outline The problem of the urea-SCR control as used in automotive application with diesel engines is studied in this thesis. The manuscript is organized as follows. In Chapter 1, we recall the European standards relative to diesel engines emissions, and provide a chemical engineers' description of the SCR system. A detailed model for the SCR using results from the literature is exposed and analyzed in order to sketch some issues related to the distributed (1D) nature of the considered system. Several successive reductions of this simulation model are proposed and lead to a simpler one, better-suited for control design purposes. In Chapter 2, the main difficulties encountered in the control design are exposed. An analysis and a model of the actual sensors technology is given. The choice of the coverage ratio target is defined. In chapter 3, the control strategy based on a closed-loop dynamics coupled to an algebraic equation (defining the stabilizing controller) is presented. The proposed control scheme is scheduled to account for variations of inlet NO_x, gas velocity and temperature conditions. A simple calibration rule obtained from the analysis of the closed-loop stability is proposed. To stress the relevance of the contribution, experimental control results are presented in Chapter 4. Finally, some extensions are detailed in chapter 5.

The works presented in this manuscript have appeared in the following publications:

- **Journals**

  1. A. Bonfils, Y. Creff, O. Lepreux, & N. Petit. Closed-loop control of a SCR system using a NO_x sensor cross-sensitive to NH_3. *Journal of Process Control*, 2013. To appear, DOI: 10.1016/j.jprocont.2013.08.010.

- **Conferences**

  1. A. Bonfils, Y. Creff, O. Lepreux, & N. Petit. Closed-loop control of a SCR system using a NO_x sensor cross-sensitive to NH_3. In *Advanced Control of Chemical Processes*, pages 738–743, 2012.
  2. C. Quérel, A. Bonfils, O. Grondin, & Y. Creff. Control of a SCR system using a virtual NO_x sensor. In *7th IFAC Symposium on Advances in Automotive Control*, Tokyo, Japan, Sept. 4-7, 2013.

Contents

Nomenclature

Acronyms

BGR Burned Gas Ratio

CAN Controller Area Network

CI Compression Ignition

DOC Diesel Oxidation Catalyst

DPF Diesel Particulate Filter

ECU Engine Control Unit

EGR Exhaust Gas Recirculation

HMI Human Machine Interface

NEDC New European Driving Cycle

PWM Pulse Width Modulation

SCR Selective Catalytic Reduction

SI Spark Ignited

UDP User Datagram Protocol

Chemical Species

CO carbon monoxide

CO_2 carbon dioxide

HC hydrocarbon

HNCO isocyanic acid

H_2O water

N_2 nitrogen

NH_3 ammonia

$(NH_2)_2CO$ urea

NH_4NO_3 ammonium nitrate

NO nitrogen monoxide

NO_2 nitrogen dioxide

NO_x nitrogen oxides ($NO + NO_2$)

N_2O nitrous oxide

O_2 oxygen

Parameters

A_{cell} cell cross-sectional area [m^2]

C_i^m mass concentration of the species i [$kg.m^{-3}$]

C_i molar concentration of the species i [$mol.m^{-3}$]

Cp specific gas heat [$J.kg^{-1}.K^{-1}$]

Cp_s specific heat of monolith [$J.kg^{-1}.K^{-1}$]

E_a activation energy in NH_3 adsorption reaction rate [$kJ.mol^{-1}$]

E_d activation energy in NH_3 desorption reaction rate [$kJ.mol^{-1}$]

E_f activation energy in “fast” SCR reaction rate [$kJ.mol^{-1}$]

E_o activation energy in direct oxidation of adsorbed NH_3 by O_2 reaction rate [kJ.mol^{-1}]

E_r activation energy in "global" NO_x reduction reaction rate [kJ.mol^{-1}]

E_s activation energy in "standard" SCR reaction rate [kJ.mol^{-1}]

ϵ_r void ratio: ratio of gas volume to total volume of catalyst [-]

F gas mass flow rate [kg.s^{-1}]

F_i mass flow rate of species i [kg.s^{-1}]

γ_{ij} stoichiometric coefficient of each species i in the reaction j [-]

G_a geometric surface area-to-volume ratio [m^{-1}]

Γ_i exchange between gas and active surface term for each species i [mol.m^{-3}.s^{-1}]

Γ_e^sp torque setpoint [N.m]

h_g convective heat transfer coefficient between gas and solid [W.m^{-2}.K^{-1}]

Δh_j enthalpy of the reaction j [J.mol^{-1}]

$\eta_{\mathrm{NO_x}}$ NO_x reduction efficiency [-]

k_I controller integral gain [-]

k_L observer gain [-]

k_P controller proportional gain [-]

k_a^0 constant factor in NH_3 adsorption reaction rate [kg.m^3.mol^{-2}.s^{-1}]

k_d^0 constant pre-exponential factor in NH_3 desorption reaction rate [kg.mol^{-1}.s^{-1}]

k_f^0 constant pre-exponential factor in "fast" SCR reaction rate [kg.m^6.mol^{-3}.s^{-1}]

k_o^0 constant pre-exponential factor in direct oxidation of adsorbed NH_3 by O_2 reaction rate [kg.m^3.mol^{-2}.s^{-1}]

k_r^0 constant pre-exponential factor in "global" NO_x reduction reaction rate [kg.m^3.mol^{-2}.s^{-1}]

k_s^0 constant pre-exponential factor in "standard" SCR reaction rate [kg.m^3.mol^{-2}.s^{-1}]

k_g thermal conductivity of gas [W.m^{-1}.K^{-1}]

L length of the catalyst [m]

m mass of exhaust gas [kg]

m_i mass of the species i [kg]

M molecular mass of exhaust gas [kg.mol^{-1}]

M_i molecular mass of the species i [kg.mol^{-1}]

n number of moles of exhaust gas [mol]

n_i number of moles of the species i [mol]

N_e engine rotation speed [rpm]

ω inlet SCR NO_x molar concentration (disturbance variable) [mol.m^{-3}]

ω_1 inlet SCR NO molar concentration (disturbance variable) [mol.m^{-3}]

ω_2 inlet SCR NO_2 molar concentration (disturbance variable) [mol.m^{-3}]

Ω NH_3 storage capacity [mol.m^{-3}]

P Pressure [Pa]

r_j rate of reaction j [mol.m^{-3}.s^{-1}]

R universal gas constant ≈ 3.1415 [kJ.mol^{-1}.K^{-1}]

ρ_g exhaust gases density [kg.m^{-3}]

ρ_s monolith density [kg.m^{-3}]

s coordinate along the flow axis [m]

S useful cross-sectional surface of the catalyst [m^2]

T gas temperature [K]

T^{in} inlet SCR gas temperature (disturbance variable) [K]

T^{out} outlet SCR gas temperature [K]

T_s surface (or monolith) temperature [K]

u inlet SCR NH_3 molar concentration (control variable) [mol.m^{-3}]

v exhaust gas velocity (disturbance variable) [m.s^{-1}]

V volume of exhaust gases in the catalyst [m^3]

x NH_3 coverage ratio [-]

$\hat{x}$ estimation of the NH_3 coverage ratio [-]

x^{sp} NH_3 coverage ratio setpoint [-]

χ_i mass fraction of the species i [-]

y outlet SCR measurement [mol.m^{-3}]

y_i molar fraction of the species i [-]

Chapter 1

Description of urea selective catalytic reduction (urea-SCR)

1.1 Introduction

During the last twenty years, diesel engines have been increasingly promoted by the automotive industry. This trend which is particularly visible in Europe has

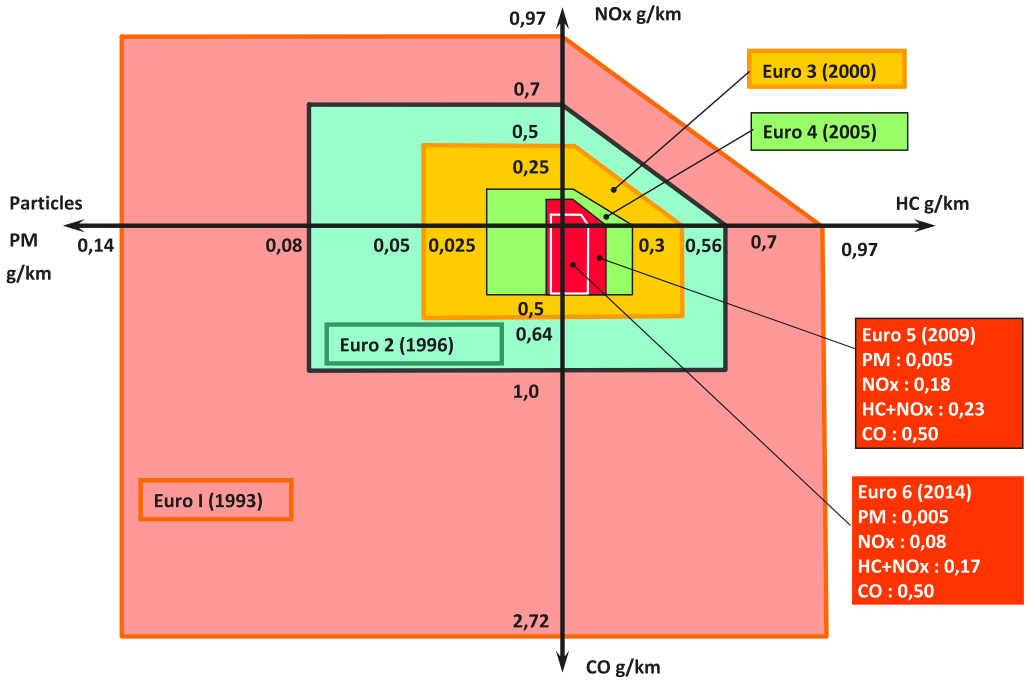

Figure 1.1: Evolution of European emission standards from 1993 to 2014 for light-duty diesel vehicles (Source: IFP training course - Fuels, lubricants and engines).

been spurred by their high energetic efficiency and the lower sale prices of diesel fuel compared to gasoline. As a result, in the European market, 55% of new registered passenger cars are diesel engines (compared to an average of 15% in the early 90's, see ACEA (2012))[1].

Starting in 1993 (in Europe), stringent emission standards have been introduced to reduce the pollutant emissions of automotive vehicles. These standards target four main pollutants: carbon monoxide (CO), hydrocarbons (HC), nitrogen oxides[2] (NO_x) and particulate matter (PM). They state quantitative maximum allowable levels for each category of vehicles (those equipped with compression ignition (CI) or spark ignited (SI) engine, passenger cars or trucks, e.g.). The successive European standards for the four regulated pollutants are pictured in Figure 1.1 and detailed in Table 1.1. This parallel view makes it visible how they have steadily become more stringent. To obtain commercialization rights in Europe, all the new diesel passenger vehicles must satisfy these emission limits, defined for a common normalized NEDC[3] cycle. Satisfying these standards has required significant and continuing efforts in technology improvements from car manufacturers.

	NO_x [g/km]	HC + NO_x [g/km]	CO [g/km]	PM [g/km]	Number of PM [Nb/km]
Euro 1 (1993)	-	0.97	2.72	0.14	
Euro 2 (1996)	-	0.70	1.00	0.08	
Euro 3 (2000)	0.50	0.56	0.64	0.05	
Euro 4 (2005)	0.25	0.30	0.50	0.025	
Euro 5 (2009)	0.18	0.23	0.50	0.005	
Euro 6 (2014)	0.08	0.17	0.50	0.005	$6\ 10^{11}$

Table 1.1: European emission standards for diesel passenger cars.

A part of these efforts bear on new embedded equipments called aftertreatment devices. Progressively, with the developments of the standards, these devices have been introduced by all manufacturers in the exhaust line of their diesel engine vehicles. These devices are of three (main) types: DOC, DPF and NO_x systems. In view of the 2005 Euro 4 standard, the diesel oxidation catalyst (DOC, refer to Stein (1996), Eastwood (2000), Lepreux (2009)) has appeared necessary to treat HC and CO. For the 2009 Euro 5 standard, a particulate filter (DPF) has been installed

[1] In comparison, the registration of new diesel engine passenger cars in France has increased from 33% in 1990 to 73% in 2012.

[2] This notation includes nitrogen oxide (NO) and nitrogen dioxide (NO_2).

[3] New European Driving Cycle.

on all[4] cars to treat PM (Van Nieuwstadt & Tennison (2006)). This situation is a bit different for the NO_x emissions as, so far, no aftertreatment system is required to meet the regulations which are, in some respect, too loose. Instead, numerous technological improvements in the internal combustion engines have been achieved (exhaust gas recirculation (EGR), combustion optimization, to name a few) and have allowed to meet current standards (Euro 5). To stress the need for limiting NO_x emissions, it suffices to briefly comment on the polluting role of NO_x, which are for the most part produced by road transportation (transportation represents 57% of French emissions in metropolitan areas in 2011, the first emitters being heavy duty vehicles, followed by diesel passenger cars). These pollutants are highly toxic, especially NO_2. Once released into the atmosphere, they cause acid rain, depletion of ozone and photochemical fog (CITEPA (2012)). The thresholds of lethal effects for a 60 minutes exposure to these gases are 70 ppm for NO_2, 600 ppm for NO and 3200 ppm for CO (INERIS (2004)). The evolution from 2009 Euro 5 to the upcoming 2014 Euro 6 standard will disrupt the plans as it consists in drastically reducing the acceptable level of NO_x emissions. To meet the Euro 6 requirements, most car manufacturers have introduced NO_x aftertreatment devices in their next generation of diesel engines. This appears as inescapable.

A possible layout of aftertreatment devices in an Euro 6 - capable exhaust line is pictured in Figure 1.2. Among the variety of encountered technologies envisioned for this task (including lean NO_x trap, e.g.), urea selective catalytic reduction (urea-SCR) is one of the most appealing approaches and is the subject studied in this thesis.

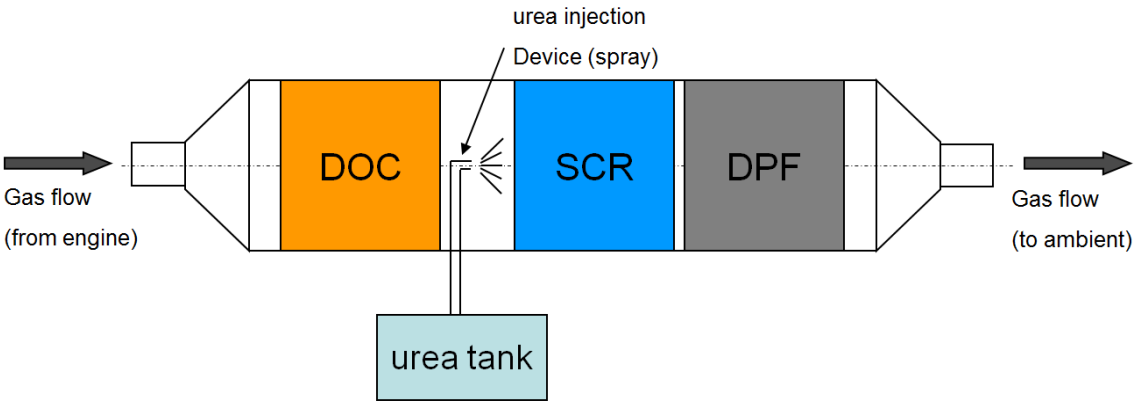

Figure 1.2: Aftertreatment devices in the exhaust line of diesel engine vehicles. The locations of the SCR catalyst and the DPF can be interchanged.

Historically, SCR has been employed for fixed industrial applications such as

[4]This aftertreatment device was already embedded in some vehicles from the 2000's.

thermal power plants, operating under steady conditions. Over the last decade, urea-SCR has been frequently embedded into heavy duty vehicles (since the 2000 Euro III standard) which also operate under relatively steady regimes. Notwithstanding its discussed appealing properties, urea-SCR has been implemented only in few passenger cars where operating conditions are vastly varying. Compared to other technologies (Lean NO_x Trap, HC-SCR,...), urea-SCR presents numerous advantages (Lambert et al. (2004), Johnson (2006)). One main advantage is that controlling it, using the urea injector, does not require any action on the engine itself, which permits to avoid disturbing the engine control management systems (air path, fuel path controllers, among others). A second and main advantage of urea-SCR is its ability to treat larger amounts of NO_x. A third is its reasonable cost.

1.2 A chemical engineer description of the urea-SCR

In the urea-SCR, the selective catalytic reduction is performed on a monolithic reactor coated with an active surface. This tubular reactor is fed by the exhaust gas flowing out from the diesel engine. The reactor consists of numerous thin and parallel channels with a geometry designed to maximize the mass and thermal transfer at the catalytic surface (see Figure 1.3). Commonly, these catalysts have a channel density of approx. 400 cpsi[5], each channel of the monolith being about 1 mm of width. The wall thickness is about 10^{-1} mm.

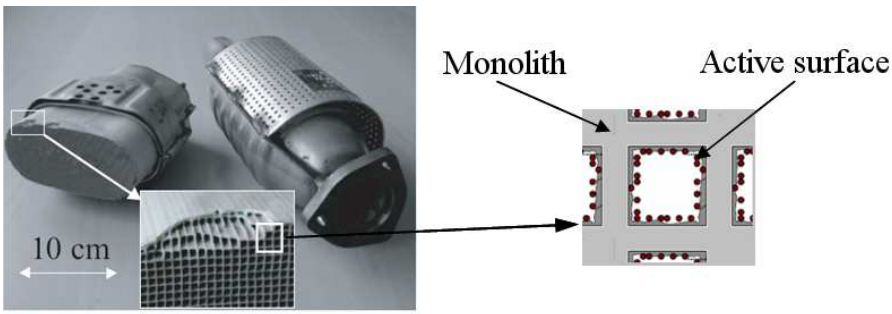

Figure 1.3: A SCR catalyst (with and without canning) used in a heavy duty vehicle application.

The operation principle of the SCR requires to inject (under the form of a spray) an aqueous solution of urea (e.g. AdBlue®: 32.5 wt%[6] of urea) in the gas flowing through the exhaust line of the diesel engine (see again Figure 1.2). This requires

[5]cells per square inch
[6]weight percent

an urea storage tank in the vehicle and a dedicated injection system capable of creating a spray of urea in the exhaust line. Urea is transformed into NH_3 by decomposition: one mole of urea $(NH_2)_2CO$ provides two moles of NH_3. Then, the produced NH_3 is stored onto the active phase of the catalyst through an adsorption process. There, the adsorbed NH_3 combines with gaseous NO_x according to various reduction reactions, producing nitrogen and water, and various side products. The key steps of this process are explained in the following subsections.

1.2.1 Urea decomposition

The decomposition of urea into NH_3 involves an evaporation followed by two chemical reactions. The evaporation is particularly sensitive to the temperature and to the spray droplets size. In certain implementations, a mixer (see Figure 1.4a) is introduced between the injector and the catalyst. The latter homogenizes the flow of urea over the whole upstream surface of the catalyst. It also reduces the droplets size.

(a) Urea mixer. (b) SCR catalyst with solid deposit.

Figure 1.4: An urea mixer and a solid deposit on the front face of the catalyst (source: IFPEN).

Then, the evaporated urea is decomposed into NH_3 and isocyanic acid (HNCO) by a first chemical reaction, the thermolysis process (1.1). This reaction occurs in the exhaust line (in gas phase). For this reaction to take place, it is required that the

temperature should remain above 180°C[7]. The reaction rate reaches its maximum for temperatures around 350°C (Way et al. (2009), Strots et al. (2009)).

In a second chemical reaction, the gaseous hydrolysis (1.2), the isocyanic acid is decomposed into NH_3 and carbon dioxide (CO_2). This reaction takes place in the upstream section (first few millimeters) of the SCR catalyst (Hsieh & Wang (2010b)).

$$(NH_2)_2CO_{(g)} \rightarrow HNCO_{(g)} + NH_{3(g)} \quad (1.1)$$

$$HNCO_{(g)} + H_2O_{(g)} \rightarrow NH_{3(g)} + CO_{2(g)} \quad (1.2)$$

The location of the injector in the exhaust line is a crucial parameter:

i. The injector must be situated sufficiently far from the catalyst to guarantee that the thermolysis reaction (1.1) is complete before gases enter the catalyst;

ii. It must also be close enough to the catalyst to prevent the formation of ammonium nitrate (NH_4NO_3) according to the side reaction detailed below in § 1.2.3, when the temperature lies within the [100, 250]°C range.

According to some studies reported in the literature (Fang & Da Costa (2003), Chi & Da Costa (2005), Hsieh & Wang (2010a)), the reaction mechanisms (1.1) and (1.2) can be simplified under the form (Hsieh & Wang (2010a)) of a first order system:

$$\tau_{urea}\frac{dC_{NH_3}}{dt} = -C_{NH_3} + 2C_{\text{urea}}\left(1 - \exp\frac{-x_{\text{urea}}}{l_{\text{urea}}}\right)\eta_{NH_3}$$

where τ_{urea} is the mixing time constant, l_{urea} is the characteristic mixing length, x_{urea} is the distance from the urea injection system to the catalyst upstream section, η_{NH_3} is the conversion efficiency of urea into NH_3. The variables C_{urea} and C_{NH_3} are the molar concentrations in urea (input) and NH_3 (state), respectively. Further, based on our own experimental results, we decided to neglect this dynamics and consider that the urea decomposition into NH_3 is always complete, provided that the injector is located sufficiently far from the catalyst.

1.2.2 NH_3 adsorption/desorption

The NH_3 produced by the above-described decomposition of urea is stored on the active surface of the catalyst (Ciardelli et al. (2004), Willems et al. (2007))

[7]For temperatures below 180°C, the decomposition of urea usually produces secondary products such as cyanuric acid, melamine and biuret (refer to Koebel & Strutz (2003) for further details). These compounds are deposited under the form of solid agglomerates in the exhaust line and on the front face of the catalyst (refer to Figure 1.4b). The are particularly difficult to remove while having a detrimental clog up effect on the catalyst.

where it will react with the NO_x contained in the nearby flowing exhaust gases. The adsorption mechanism commonly reported in the literature states that each molecule of NH_3 get adsorbed on the first available adsorption site it finds.

An equilibrium state of adsorption is established between the gas phase and the adsorbed surface. This defines an equilibrium value of the amount of absorbed NH_3. Alternatively, the adsorbed NH_3 molecules can be desorbed from the active surface and thus released into the gas flow. This undesirable phenomenon occurs on two different occasions: *i)* when the molar concentration of NH_3 in gas phase is lowered, the adsorption/desorption equilibrium state is disturbed, and some of the adsorbed NH_3 molecules change to the gas state, *ii)* when the temperature increases, the adsorption/desorption equilibrium is quickly modified toward the desorption process and adsorbed molecules move to the gas phase. This last scenario is referred to as "thermal desorption".

In some cases, other mechanisms and forms of adsorbed NH_3 must be considered (Olsson et al. (2008), Frobert et al. (2009)). Competitions exist among the various adsorption phenomena (for NH_3, and NH_4NO_3, e.g.), and also among several species contained in the exhaust gases (mainly water and HC). On zeolite catalysts, there also exists a competition on several acid sites (referred to as Brönsted and Lewis sites, see Skarlis et al. (2012) for further details) between two types of adsorption (physisorption or chemisorption). These competitions create a vast range of possibilities for the adsorption and the desorption.

In the sequel, we will use a simple description involving only one adsorbed species: the NH_3.

1.2.3 Reaction of the adsorbed NH_3: NO_x reduction and competing reactions

Among the possible types of NO_x reduction by adsorbed NH_3, two leading reactions are usually considered (Chatterjee et al. (2006), Grossale et al. (2008a,b)). These are called "fast" and "standard" SCR (Selective Catalytic Reduction), respectively:

$$4NH_{3(s)} + 2NO_{(g)} + 2NO_{2(g)} \rightarrow 4N_{2(g)} + 6H_2O_{(g)} \quad (\text{"fast" SCR}) \tag{1.3}$$

$$4NH_{3(s)} + 4NO_{(g)} + O_{2(g)} \rightarrow 4N_{2(g)} + 6H_2O_{(g)} \quad (\text{"standard" SCR}) \tag{1.4}$$

These are irreversible reactions limited by kinetics. Their efficiency depends on the conditions (the temperature and the competition between kinetics and transport of gases have an impact) where they operate.

There also exists a third reaction:

$$4NH_{3(s)} + 3NO_{2(g)} \rightarrow \frac{7}{2}N_{2(g)} + 6H_2O_{(g)} \quad (\text{"}NO_2\text{" SCR}) \tag{1.5}$$

It is generally not considered in the modeling of SCR systems because it is far slower than the other two (1.3)-(1.4).

Competing reactions Besides, a significantly competing phenomenon is the direct oxidation of the adsorbed NH_3 by oxygen (O_2). In diesel engines vehicles, O_2 is in excess in the exhaust gases (by definition diesel engines operate in lean[8] burn environment).

For temperatures above 400°C, the oxidation takes several forms. In Chatterjee et al. (2005), the theoretical competitions between oxidation reactions producing N_2 (1.6), N_2O (nitrous oxide), NO and NO_2 are discussed. In theory, the competitions have various non negligible consequences. The oxidation (1.6) simply leads to an increase in the urea consumption. The oxidation toward N_2O is particularly undesirable because N_2O is a strong greenhouse gas (200 times more impacting than CO_2, see Dore et al. (2003)). Finally, the oxidations toward NO and NO_2 yield an increase of urea (NH_3) consumption and generate additional pollutants to be treated. The four possible oxidation of adsorbed NH_3 reactions are

$$4NH_{3(s)} + 3O_{2(g)} \rightarrow 2N_{2(g)} + 6H_2O_{(g)} \tag{1.6}$$

$$\begin{aligned} 4NH_{3(s)} + 4O_{2(g)} &\rightarrow 2N_2O_{(g)} + 6H_2O_{(g)} \\ 4NH_{3(s)} + 5O_{2(g)} &\rightarrow 4NO_{(g)} + 6H_2O_{(g)} \\ 4NH_{3(s)} + 7O_{2(g)} &\rightarrow 4NO_{2(g)} + 6H_2O_{(g)} \end{aligned}$$

The selectivities of these reactions vary with the type of catalyst under consideration. In this thesis, we consider two kinds of catalysts: a Fe-zeolite and a Cu-zeolite. As shown in Devadas et al. (2005), the direct oxidation of $NH_{3(s)}$ is nearly 100% selective towards N_2 (only (1.6) takes place) when a Fe-zeolite catalyst is employed. Similar results with Cu-zeolite catalysts have been established in Gang (2002). In the sequel, we will therefore consider that only (1.6) takes place and that N_2 is the primary product of the adsorbed NH_3 direct oxidation by O_2. This leads us to neglect the other reactions.

Figure 1.5 reports the efficiency for the three reactions of NO_x reduction (1.3)-(1.4)-(1.5) and direct oxidation of adsorbed NH_3 by O_2 (1.6) as functions of the temperature. For each reaction, the efficiency (which can be viewed as a static parameter) is defined as the ratio $(C_i^{in} - C_i^{out})/C_i^{in}$, where C_i^{in} and C_i^{out} are the molar concentrations of species i ($i = NO_x$ for NO_x reduction and $i = NH_3$ for direct oxidation of adsorbed NH_3 by O_2) at the inlet and the outlet of the catalyst,

[8] A blend is lean when the Air/Fuel ratio exceeds the stoichiometry, and is rich below the stoichiometry.

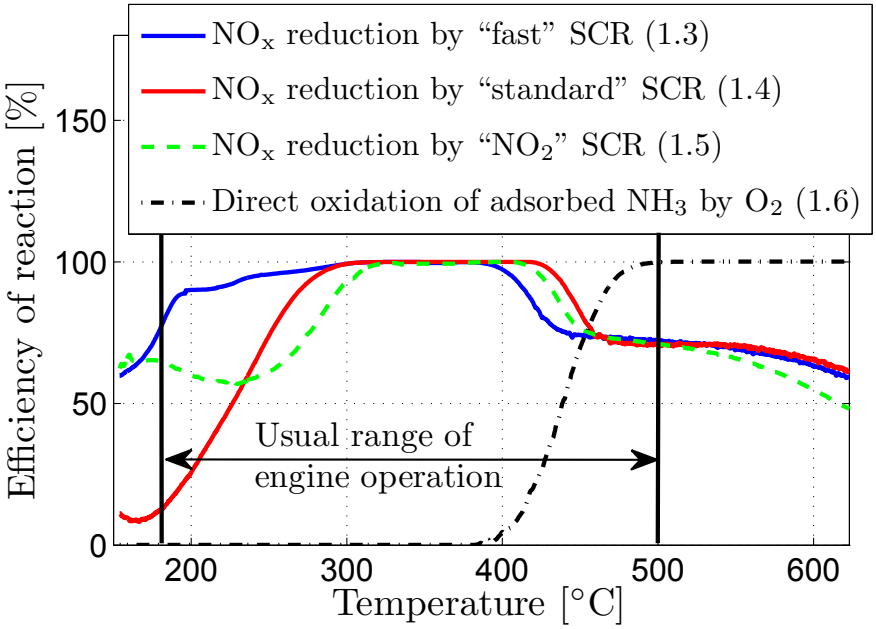

Figure 1.5: Efficiency of the NO_x reduction reactions ("fast", "standard" and "NO_2" SCR) and direct oxidation of adsorbed NH_3 by oxygen as function of the temperature. Experimental results obtained with a Fe-zeolite catalyst.

respectively. These curves plot experimental data obtained separately (one particular experiment gives one curve) on a Synthetic Gas Bench (SBG) with a Fe-zeolite catalyst. To isolate the various reactions, the following procedure is used. The gas flow is adapted with

- equimolar amounts of NO_x (50% NO and 50% NO_2) and NH_3 (without O_2) to promote the "fast" SCR (1.3) with respect to transport/transfer of gases.
- equimolar amounts of NO and NH_3 (in excess of O_2) to promote the "standard" SCR (1.4) with respect to transport/transfer of gases.
- equimolar amounts of NO_2 and NH_3 (without O_2) to promote the "NO_2" SCR (1.5) with respect to transport/transfer of gases;
- only NH_3 (in excess of O_2) to promote the direct oxidation of NH_3 by O_2 (1.6) with respect to transport/transfer of gases.

From Figure 1.5 several remarks can be formulated. The "fast" SCR reaction (1.3) is the dominant reaction of NO_x reduction, because of its wide range of optimum conversion temperature and its relatively high efficiency at low temperatures. The "standard" SCR reaction (1.4) is not very effective at low temperatures but

has a relatively wide range of optimum conversion. The "NO_2" SCR reaction (1.5) is relatively effective at low temperatures but has the smallest range of optimum conversion. The direct oxidation of NH_3 by O_2 (1.6) becomes non negligible near 370°C and seems to impact equivalently all the reactions of NO_x reduction at high temperature: from 425°C these three reactions are limited in the same way. Finally, one should note that, depending on the type of employed catalyst, the direct oxidation of adsorbed NH_3 by O_2 may occur earlier in temperature. This is the case with a Cu-zeolite catalyst.

In theory, when exhaust gases contain NO and no NO_2, only (1.4) takes place. When NO and NO_2 are present, (1.3) is predominant (faster reaction, better efficiency at low temperature and higher range of optimal conversion), until the exhaustion of one of the two species. The remaining NO is consumed by (1.4). The remaining NO_2 is consumed by (1.5) (slow process). Finally, according to the current engine operating ranges and with the current technology of DOC, there is rarely an excess of NO_2 (especially in the temperature range of optimum conversion for the "NO_2" SCR reaction), which leads us to neglect the reaction (1.5).

For sake of completeness, one shall also mention another competing reaction which is the formation of ammonium nitrate NH_4NO_3:

$$2NH_{3(s)} + 2NO_{2(g)} \rightarrow NH_4NO_{3(s)} + N_{2(g)} + H_2O_{(g)}$$

This reaction is thermally promoted when the temperature is below 200°C. This range of temperature is outside our area of considered engine operating conditions. The formed NH_4NO_3 is stored on the active sites of the catalyst and leads to a reversible inhibition. When ammonium nitrate decomposes at low temperatures (above 180°C), a competition between several reactions takes place to form NO_2, NH_3 or N_2O according to the following reactions (Ciardelli et al. (2007)):

$$\begin{aligned} NH_4NO_{3(s)} &\rightarrow NH_{3(g)} + HNO_{3(g)} \\ NH_4NO_{3(s)} &\rightarrow \frac{3}{4}N_{2(g)} + \frac{1}{2}NO_{2(g)} + 2H_2O_{(g)} \\ NH_4NO_{3(s)} &\rightarrow N_2O_{(g)} + 2H_2O_{(g)} \end{aligned}$$

These additional competing phenomena (the last four reactions) can be considered as disturbing dynamics as they consume NH_3 and create highly toxic new products. However, the amount of NH_3 involved in this reaction scheme is small and will be neglected in the sequel.

1.3 Derivation of dynamics

1.3.1 Kinetic laws

Summarizing the previous discussions and according to Chi & Da Costa (2005), Upadhyay & Van Nieuwstadt (2006), Schär et al. (2006), Herman et al. (2009), Hsieh & Wang (2009b), Devarakonda et al. (2009), modeling SCR systems operated in the [180, 500]°C range of temperatures (which is typical for our aftertreatment application) requires to consider the following phenomena: the NH_3 adsorption and desorption equilibrium, the NO_x reduction reactions ("fast" SCR (1.3) and "standard" SCR (1.4)) and the direct NH_3 oxidation towards N_2 reaction (1.6). These are the phenomena under consideration in this thesis.

Following Ciardelli et al. (2004), Kim et al. (2007), Hsieh & Wang (2010a), the rates of reactions of the considered phenomena can be modeled with Arrhenius kinetics (excepted for adsorption/desorption process) which are defined below, referring to Table 1.2 for notations.

Table 1.2: Summary of notations for equations (1.7) to (1.11).

x	coverage ratio	[-]
z_{11}	molar concentration of NO	$[\text{mol.m}^{-3}]$
z_{12}	molar concentration of NO_2	$[\text{mol.m}^{-3}]$
z_2	molar concentration of NH_3	$[\text{mol.m}^{-3}]$
C_{O_2}	molar concentration of O_2	$[\text{mol.m}^{-3}]$
Ω	NH_3 storage capacity	$[\text{mol.m}^{-3}]$
T_s	surface (or monolith) temperature	[K]
k_a^0	constant factor in NH_3 adsorption reaction rate	$[\text{kg.m}^3.\text{mol}^{-2}.\text{s}^{-1}]$
k_d^0, k_f^0, k_s^0, k_o^0	pre-exponential factors in NH_3 desorption, "fast" SCR, "standard" SCR and direct oxidation of NH_3 by O_2 reaction rates, respectively	$[\text{kg.mol}^{-1}.\text{s}^{-1}]$, $[\text{kg.m}^6.\text{mol}^{-3}.\text{s}^{-1}]$, $[\text{kg.m}^3.\text{mol}^{-2}.\text{s}^{-1}]$, $[\text{kg.m}^3.\text{mol}^{-2}.\text{s}^{-1}]$
E_d, E_f, E_s, E_o	activation energies in desorption, "fast" SCR, "standard" SCR and direct oxidation of NH_3 by O_2 reaction rates, respectively	$[\text{kJ.mol}^{-1}]$
M_{NH_3}, M_{NO_x}	molecular mass of NH_3 and NO_x, respectively	$[\text{kg.mol}^{-1}]$
ϵ_r	void ratio: ratio between gas volume and total volume	[-]
R	universal gas constant	$[\text{kJ.mol}^{-1}.\text{K}^{-1}]$
σ	tuning parameter	[-]

- NH_3 adsorption/desorption:

$$\begin{cases} r_{\mathrm{a}} = \underbrace{\dfrac{k_{\mathrm{a}}^0}{M_{\mathrm{NH_3}}}}_{\triangleq\, k_{\mathrm{a}}} z_2 \Omega (1-x) & (1.7) \\ r_{\mathrm{d}} = \underbrace{\dfrac{k_{\mathrm{d}}^0}{M_{\mathrm{NH_3}}} \exp\left(\dfrac{-E_{\mathrm{d}}(1-\sigma x)}{RT_s}\right)}_{\triangleq\, k_{\mathrm{d}}(T_s)} \Omega x & (1.8) \end{cases}$$

- "fast" SCR reduction (1.3):

$$r_{\mathrm{f}} = \underbrace{\frac{k_{\mathrm{f}}^0}{M_{\mathrm{NO_x}}} \exp\left(\frac{-E_{\mathrm{f}}}{RT_s}\right)}_{\triangleq\, k_{\mathrm{f}}(T_s)} z_{11} z_{12} \Omega x \tag{1.9}$$

- "standard" SCR reduction (1.4):

$$r_{\mathrm{s}} = \underbrace{\frac{k_{\mathrm{s}}^0}{M_{\mathrm{NO_x}}} \exp\left(\frac{-E_{\mathrm{s}}}{RT_s}\right)}_{\triangleq\, k_{\mathrm{s}}(T_s)} z_{11} \Omega x \tag{1.10}$$

- direct oxidation of NH_3 by O_2 producing N_2 (1.6):

$$r_{\mathrm{o}} = \underbrace{\frac{k_{\mathrm{o}}^0}{M_{\mathrm{NH_3}}} \exp\left(\frac{-E_{\mathrm{o}}}{RT_s}\right) C_{\mathrm{O_2}}}_{\triangleq\, k_{\mathrm{o}}(T_s)} \Omega x \tag{1.11}$$

The adimensional variable x (*coverage ratio*) appearing in all the rates of reaction above is the ratio between the number of occupied catalytic sites and the total number of catalytic sites:

$$x = \frac{C_{\mathrm{NH_3},s}}{\Omega} \tag{1.12}$$

where $\Omega = \Omega' \epsilon_r / (1-\epsilon_r)$ [mol/m^3] and Ω' is the NH_3 storage capacity. For sake of conciseness, we will call Ω the NH_3 storage capacity. Equations (1.8) to (1.11) imply coefficients depending on the monolith temperature $k_j(T_s)$, $j \in \{\mathrm{d}, \mathrm{f}, \mathrm{s}, \mathrm{o}\}$. The choice of these expressions for the reaction rates is a generally recognized assumption (Chatterjee et al. (2005, 2006), Olsson et al. (2008)).

Before closing the discussion, one can remark several facts. The expression (1.7) assumes non-activated adsorption of NH_3 onto the catalytic sites (no activation energy in the expression). Furthermore, in the NH_3 desorption reaction rate (1.8), the heterogeneity of the catalyst surface (porous material) is accounted for by considering the activation energy of the desorption process as a linear function of the coverage ratio x ($E_d(1-\sigma x)$ in (1.8)) as it is commonly done in the literature (Chatterjee et al. (2006), Grossale et al. (2008b), Schuler et al. (2008)). Gradually, when the coverage ratio is increased, deeper and deeper pores are used in the adsorption process, and the NH_3 adsorbed molecules get harder to desorb.

1.3.2 Spatially distributed material and energy balances (P-DE)

Based on the description of chemical reactions above, we now develop a 1-dimensional model of the catalyst converter. Classically, it is introduced following the approach presented in Oh & Cavendish (1982), Winkler et al. (2003), Kim

Table 1.3: Summary of notations for equations (1.13) to (1.16).

T, T_s	gas and surface (or monolith) temperature, respectively	[K]
$C_{i,g}$, $C_{i,s}$	gas and surface molar concentration of species i, respectively	[mol.m^{-3}]
F	gas mass flow rate	[kg.s^{-1}]
Γ_i	exchange between gas and active surface term for each species i	[mol.m^{-3}.s^{-1}]
Δh_j	enthalpy of the reaction j	[J.mol^{-1}]
r_j	rate of reaction j	[mol.m^{-3}.s^{-1}]
γ_{ij}	stoichiometric coefficient of each species i in the reaction j	[-]
ρ_g, ρ_s	gas and surface density, respectively	[kg.m^{-3}]
Cp, Cp_s	specific gas and monolith heat, respectively	[J.kg^{-1}.K^{-1}]
k_g	gas thermal conductivity	[W.m^{-1}.K^{-1}]
h_g	convective heat transfer coefficient between gas and solid	[W.m^{-2}.K^{-1}]
A_{cell}	cross-sectional area	[m^2]
L	length of the catalyst	[m]
G_a	geometric surface area-to-volume ratio	[m^{-1}]
N_M	number of species	[-]
N_R	number of reactions	[-]

et al. (2007). The variables are distributed along the axial direction of the catalyst (which abscissa is noted s) and the phenomena are represented by partial differential equations. Radial effects are neglected. The employed symbols are summarized in Table 1.3. In details, T, C and ρ refer to the gas temperature, the molar concentration and the density, respectively. The subscript s refers to the surface (or monolith) while the subscript g refers to the gas. Cp is the specific gas heat, Cp_s the specific monolith heat and F is the gas mass flow rate. A_{cell} is the cross-sectional area, k_g is the thermal conductivity of the gas, h_g is the convective heat transfer coefficient between gas and solid, G_a is the geometric surface area-to-volume ratio. N_M is the number of species. Γ_i is, for each specy i, the amount of exchange between the gas and the active surface. γ_{ij} is the stoichiometric coefficient of each species i in the reaction j. Finally r_j and Δh_j are, for each reaction j, the rate of reaction and the enthalpy of reaction, respectively.

The balance equations are

- Gas temperature dynamics

$$\underbrace{\epsilon_r \rho_g Cp \frac{\partial T}{\partial t}}_{\text{Gas storage}} + \underbrace{\frac{F}{A_{cell}} Cp \frac{\partial T}{\partial s}}_{\text{Gas transport}} = \underbrace{\frac{\partial}{\partial s}\left(\epsilon_r k_g \frac{\partial T}{\partial s}\right)}_{\text{Diffusion}} - \underbrace{h_g G_a \left(T - T_s\right)}_{\text{Exchange with monolith}} \tag{1.13}$$

- Monolith temperature dynamics

$$\underbrace{\left(1-\epsilon_r\right) \rho_s Cp_s \frac{\partial T_s}{\partial t}}_{\text{Monolith storage}} = \underbrace{\frac{\partial}{\partial s}\left(\left(1-\epsilon_r\right) k_s \frac{\partial T_s}{\partial s}\right)}_{\text{Solid diffusion}} + \underbrace{h_g G_a \left(T - T_s\right)}_{\text{Exchange with gas}} + \underbrace{\epsilon_r \sum_{j=1}^{N_R} r_j \Delta h_j}_{\substack{\text{Enthalpy flow of} \\ \text{chemical reactions}}} \tag{1.14}$$

- Mass balance for gas species

$$\underbrace{\epsilon_r \frac{\partial C_{i,g}}{\partial t}}_{\text{Gas storage}} + \underbrace{\frac{F}{\rho_g A_{cell}} \frac{\partial C_{i,g}}{\partial s}}_{\text{Gas transport}} = - \underbrace{\Gamma_i \left(C_{i,g}, C_{i,s}\right)}_{\substack{\text{Exchange with} \\ \text{the active surface}}} \quad i = 1, ..., N_M \tag{1.15}$$

- Mass balance for surface species (zero velocity)

$$\underbrace{\left(1-\epsilon_r\right) \frac{\partial C_{i,s}}{\partial t}}_{\text{Surface storage}} = \underbrace{\Gamma_i \left(C_{i,g}, C_{i,s}\right)}_{\text{Exchange with gas}} - \underbrace{\epsilon_r \sum_{j=1}^{N_R} \gamma_{ij} r_j}_{\substack{\text{Chemical} \\ \text{reaction}}} \quad i = 1, ..., N_M \tag{1.16}$$

1.3.3 Simplifying assumptions

For the development of the SCR "reference model", the following assumptions are made:

- The catalyst is viewed as one "average" channel (the channels are parallel, in large number and they are all similar). Instead of a possible collection of 1-dimensional systems, a simple 1-dimensional system is considered. Since the catalyst is thermally isolated, heat losses to the ambient are neglected.

- The diffusion effects are neglected (following Lepreux (2009) for a similar catalyst modeling).

- Without loss of generality, one can consider that the source term

$$\Psi(s,t) = \frac{\epsilon_r}{(1-\epsilon_r)\,\rho_s C p_s} \sum_{j=1}^{N_R} r_j(s,t,T_s(s,t)) \Delta h_j(s,t,T_s(s,t))$$

  is null, which is a common simplifying assumption (refer to Schär et al. (2004)). Indeed, given the low amount of gas to be treated, the influence of the energy released or consumed by the chemical reactions in the SCR cell is negligible compared to the temperature variations coming from the engine and propagating through the catalyst. Typically, a variation of 50°C for an exhaust gas mass flow of about 100 kg/h implies a thermal power of 1.4 kW. On the other hand, the consumption of 10 mg of NO_x, contained in the exhaust gas with a gas velocity of 4 m/s and an inlet temperature of 250°C, induces a thermal power of 5 W. Finally, the adsorption/desorption of 10 mg of NH_3, contained in the exhaust gas with a gas velocity of 4 m/s and an inlet temperature of 250°C, induces a thermal power of 70 W.

- Some species for which the variation of the material balance is negligible will be ignored, especially water (H_2O), nitrogen (N_2), oxygen (O_2) and carbon dioxide (CO_2) (these species are in excess in the exhaust gas).

- Following several works in the literature (Schär (2003), Kim et al. (2007), Devarakonda et al. (2008)), we neglect the surface storage term $\frac{\partial C_{i,s}}{\partial t}$ in the balance (1.16) for all species except for NH_3. Instead, we consider the algebraic equation

$$\Gamma_i\left(C_{i,g}, C_{i,s}\right) = \epsilon_r \sum_{j=1}^{N_R} \gamma_{ij} r_j$$

Then, the simplified surface balance equation is replaced in (1.15) to obtain the following mass balance equation for gas species

$$\frac{\partial C_{i,g}}{\partial t} + \frac{F}{\epsilon_r \rho_g A_{cell}} \frac{\partial C_{i,g}}{\partial s} = -\sum_{j=1}^{N_R} \gamma_{ij} r_j \tag{1.17}$$

where $i \in \{\mathrm{NO}, \mathrm{NO_2}\}$ and $j \in \{\mathrm{f}, \mathrm{s}\}$.

- The accumulation/depletion of NH_3 adsorbed onto the catalyst surface, which is typically the predominant phenomenon in the dynamics of SCR monolith reactors, has to be taken under consideration. Thus, we consider that NH_3 in gas phase as well as NH_3 in solid phase (using the definition of the coverage ratio (1.12)) are both involved in two separate dynamics derived from (1.15)-(1.16)

$$\frac{\partial C_{\mathrm{NH_3},g}}{\partial t} + \frac{F}{\epsilon_r \rho_g A_{cell}} \frac{\partial C_{\mathrm{NH_3},g}}{\partial s} = \underbrace{-\Omega k_\mathrm{a} C_{\mathrm{NH_3},g}(1 - x(s)) + \Omega k_\mathrm{d}(T_s) x(s)}_{-(r_\mathrm{a} - r_\mathrm{d})} \tag{1.18}$$

and

$$\Omega \frac{\partial x(s)}{\partial t} = \underbrace{\Omega k_\mathrm{a} C_{\mathrm{NH_3},g}(1 - x(s)) - \Omega k_\mathrm{d}(T_s) x(s)}_{r_\mathrm{a} - r_\mathrm{d}} - \sum_{j=1}^{N_R} \gamma_{ij} r_j \tag{1.19}$$

where $j \in \{\mathrm{f}, \mathrm{s}, \mathrm{o}\}$. In these two equations, to describe the exchange between the active surface and the gas phase, $\Gamma_{\mathrm{NH3}}\left(C_{\mathrm{NH_3},g}, C_{\mathrm{NH_3},s}\right)$ in (1.15) and (1.16) is replaced by a Temkin-type (Schuler et al. (2008)) NH_3 adsorption/desorption kinetics term $(r_\mathrm{a} - r_\mathrm{d})$.

To summarize, the number of species is $N_M = 3$ and the number of reactions is $N_R = 3$. Table 1.4 gives the stoichiometric coefficient γ_{ij} of each species i in the reaction j.

Table 1.4: Summary of the stoichiometric coefficients γ_{ij}. The following notations are used: f for "fast" SCR, s for "standard" SCR and o for direct oxidation of adsorbed NH_3 by O_2.

i \ j	f (1.3)	s (1.4)	o (1.6)
NO	1/2	1	0
NO_2	1/2	0	0
NH_3	1	1	1

1.3.4 Summary and "reference model"

Here, we present the distributed parameter model which will be used for simulations throughout the thesis. By introducing the following normalized parameters

$$\begin{cases} k_1 &= \dfrac{h_g G_a}{\epsilon_r \rho_g Cp} \\ k_2 &= \dfrac{h_g G_a}{(1-\epsilon_r)\,\rho_s Cp_s} \\ v(t) &= \dfrac{F(t)}{\epsilon_r \rho_g A_{cell}} \end{cases} \tag{1.20}$$

where v [m.s^{-1}] is the gas velocity, the mass balance equations derived from (1.17)-(1.18)-(1.19) and the energy balance (1.13)-(1.14) can be simply rewritten as

$$\begin{cases} \dfrac{\partial x}{\partial t} &= k_{\mathrm{a}} z_2\,(1-x) - k_{\mathrm{d}}(T_s)x - k_{\mathrm{s}}(T_s)z_{11}x - k_{\mathrm{f}}(T_s)z_{11}z_{12}x - k_{\mathrm{o}}(T_s)x \\ \dfrac{\partial z_{11}}{\partial t} + v\dfrac{\partial z_{11}}{\partial s} &= -\Omega k_{\mathrm{s}}(T_s)z_{11}x - \dfrac{1}{2}\Omega k_{\mathrm{f}}(T_s)z_{11}z_{12}x \\ \dfrac{\partial z_{12}}{\partial t} + v\dfrac{\partial z_{12}}{\partial s} &= -\dfrac{1}{2}\Omega k_{\mathrm{f}}(T_s)z_{11}z_{12}x \\ \dfrac{\partial z_2}{\partial t} + v\dfrac{\partial z_2}{\partial s} &= -\Omega k_{\mathrm{a}} z_2\,(1-x) + \Omega k_{\mathrm{d}}(T_s)x \\ \dfrac{\partial T}{\partial t} + v\dfrac{\partial T}{\partial s} &= -k_1\,(T - T_s) \\ \dfrac{\partial T_s}{\partial t} &= k_2\,(T - T_s) \end{cases} \tag{1.21}$$

where x, z_{11}, z_{12}, z_2, T and T_s depend on (s,t) and v depends on t (to improve clarity in (1.21), these dependencies are not explicitly mentioned). These equations hold for all $s \in [0, L]$ where L [m] is the length of the catalyst. k_1 and k_2 are constant parameters. The outlet SCR gas temperature is defined as $T^{out}(t) = T(L,t)$. The NO_x molar concentration at the inlet of the catalyst is defined as $\omega(t) = \omega_1(t) + \omega_2(t)$.

The system has 6 spatially distributed states x, z_{11}, z_{12}, z_2, T and T_s, 1 control $u(t)$ and 4 (measured) disturbances $\omega_1(t)$, $\omega_2(t)$, $v(t)$ and $T^{in}(t)$. The state variables and the boundary conditions are reported in Tables 1.5 and 1.6, respectively.

Table 1.5: State variables of the "reference model".

$x(s,t)$	adsorbed NH_3 coverage ratio at abscissa s, time t
$z_{11}(s,t)$	NO molar concentration in gas phase at abscissa s, time t
$z_{12}(s,t)$	NO_2 molar concentration in gas phase at abscissa s, time t
$z_2(s,t)$	NH_3 molar concentration in gas phase at abscissa s, time t
$T(s,t)$	gas temperature at abscissa s, time t
$T_s(s,t)$	monolith temperature at abscissa s, time t

Table 1.6: Boundary conditions of the "reference model".

$z_{11}(0,t) = \omega_1(t)$	NO molar concentration at the inlet of the SCR catalyst (disturbance variable)
$z_{12}(0,t) = \omega_2(t)$	NO_2 molar concentration at the inlet of the SCR catalyst (disturbance variable)
$\mathbf{z_2(0,t) = u(t)}$	NH_3 molar concentration at the inlet of the SCR catalyst (**NH_3 injection, control variable**)
$T(0,t) = T^{in}(t)$	gas temperature at the inlet of the SCR catalyst (disturbance variable)

1.3.5 Equilibrium of the "reference model"

As a first step of analysis, the SCR "reference model" (1.21) is now studied under steady state conditions. Equilibrium coverage ratio profiles are obtained by numerically solving the resulting ordinary differential equations (ODEs). These profiles are reported in Figures 1.6, 1.7 and 1.8 as function of the abscissa s, for several operating conditions and various inputs. In these cases, the amount of upstream NO_x is set to 300 ppm and the exhaust gas velocity $v(t)$ is set to 5 $m.s^{-1}$. This corresponds to a medium engine rotation speed Ne [rpm], medium load engine operating point. The inlet temperature is fixed and leads to a constant temperature profile ($T(L,t) = T(0,t)$ i.e. $T^{out} = T^{in}$), consistently with the steady solution of the two temperature equations in (1.21), see Lepreux (2009). The equilibrium coverage profile is reported for various injections of NH_3 (the constant value u is varied over a range depending on the operating conditions).

For any given injection u, the area under the curve $x(s)$ represents the total

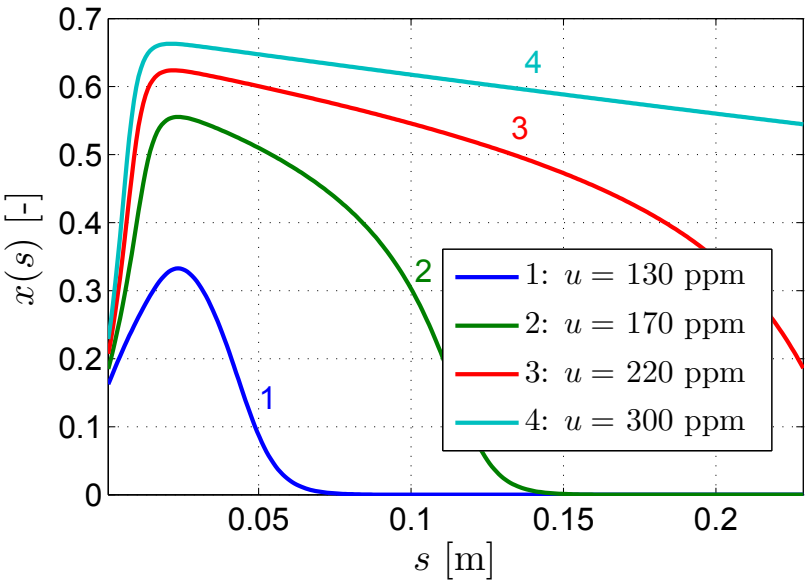

Figure 1.6: Equilibrium storage profile with $\omega_1 = 150$ ppm, $\omega_2 = 150$ ppm, $v = 5$ m.s^{-1}, $T^{in} = 200$°C and with several (constant) inputs u (130, 170, 220 and 300 ppm).

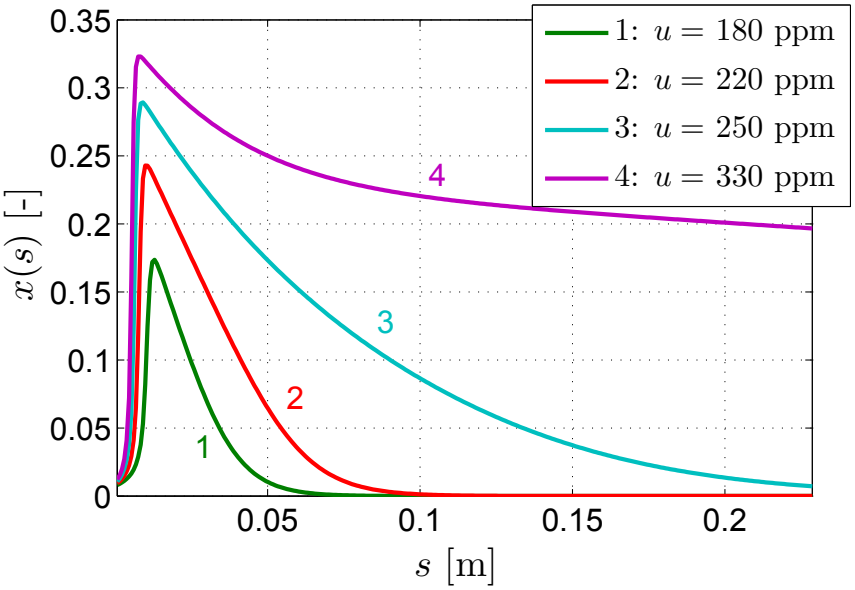

Figure 1.7: Equilibrium storage profile with $\omega_1 = 150$ ppm, $\omega_2 = 150$ ppm, $v = 5$ m.s^{-1}, $T^{in} = 300$°C and with several (constant) inputs u (180, 220, 250 and 330 ppm).

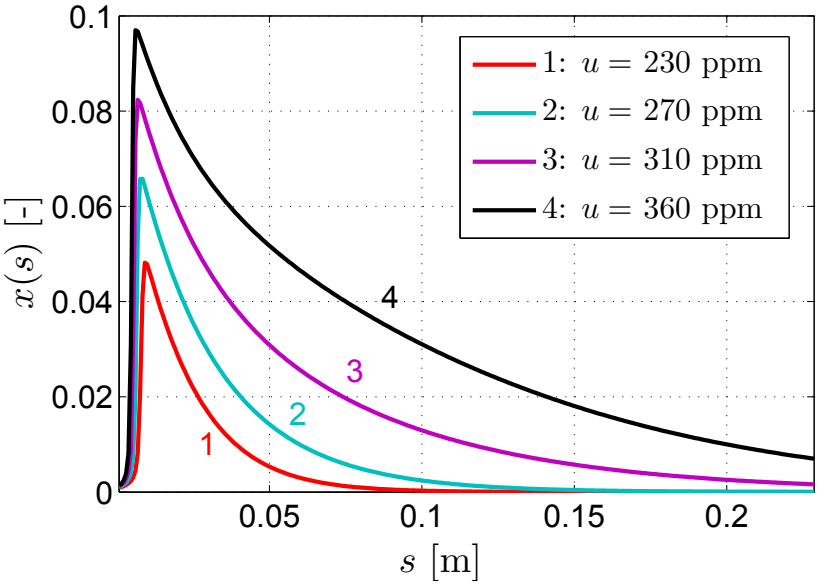

Figure 1.8: Equilibrium storage profile with $\omega_1 = 150$ ppm, $\omega_2 = 150$ ppm, $v = 5$ m.s^{-1}, $T^{in} = 400$°C and with several (constant) inputs u (230, 270, 310 and 360 ppm).

amount of NH_3 adsorbed onto the active surface of the catalyst. From these figures, it is clear that the storage of NH_3 is not uniformly distributed along the s-axis, but is predominantly concentrated near the inlet of the catalyst. This spatial distribution widely varies depending on the operating conditions and injection of NH_3. It gets more concentrated near the inlet when the temperature T^{in} is high.

More in depth investigations reveal that a large part of NO_2 is actually reduced in the first millimeters of the SCR catalyst (the "fast" SCR reaction is faster than the "standard" SCR reaction) which results in the coverage ratio x being small in the very first part of the catalyst. Then, with the decrease of NO_2, (almost) only the reduction of NO takes place, the weight of the NO_x reduction terms ("fast" SCR and "standard" SCR kinetic terms) is less significant in front of the adsorption-desorption terms, which results into a larger coverage ratio until a maximum is eventually reached. Finally, the coverage ratio slowly decreases due to progressive decline of the NH_3 to be adsorbed, as the gas travels through the catalyst. In all cases, if the steady value u is set too small, the storage gets (on average) low.

Let us now describe the overall behavior of the reactor. For this, two performance indexes are introduced.

One defines the *NO_x reduction efficiency* (η_{NO_x}) as the ratio between the reduced

NO_x and the total amount of NO_x at the inlet of the catalyst (at any time)

$$\eta_{NO_x}(t) = 1 - \frac{z_{11}(L,t) + z_{12}(L,t)}{\omega_1(t) + \omega_2(t)}$$

The other very important quantity is the *NH_3-slip* [ppm] which is the value of NH_3 that is sent to the atmosphere at the outlet of the catalyst. At any time t, it is defined as:

$$\text{NH}_3\text{-slip}(t) = z_2(L,t)$$

This performance index is of importance because tailpipe NH_3 emissions create unpleasant odors and well-known risks for human health[9]. Also, it is expected that this pollutant will be regulated in the future. The following thresholds are considered: a peak value of 30 ppm and an average value of 10 ppm (the threshold on the average value comes from the upcoming Euro VI standards concerning heavy duty vehicles).

Table 1.7 reports the steady state values of these two indexes for the curves depicted in Figures 1.6, 1.7 and 1.8.

Table 1.7: Steady state values of NO_x reduction efficiency (η_{NO_x}) and NH_3-slip under steady state conditions, for various (steady) values of the injection u and T (the combinations (u, T) are depicted in Figures 1.6, 1.7 and 1.8); $\omega_1 = 150$ ppm, $\omega_2 = 150$ ppm, $v = 5$ m.s^{-1}.

T^{in} [° C]	u [ppm]	NO_x reduction efficiency (η_{NO_x}) [%]	NH_3-slip [ppm]	NH_3 oxidized by O_2 (1.6) [ppm]
200	130	43	0	0
	170	57	0	0
	220	65	15	0
	300	73	80	0
300	180	60	0	0
	220	73	0	0
	250	85	5	0
	330	96	42	0
400	230	70	0	20
	270	81	4	23
	310	91	10	27
	360	98	25	41

[9] As an example, the effects of NH_3 are lethal for an exposure of 60 minutes to 3400 ppm, refer to INERIS (2004)

As is clearly visible, both indexes are increasing functions of the total amount of NH_3 stored onto the active surface of the catalyst. It is also visible that it is difficult to achieve very high reduction (above 90%) while keeping the NH_3-slip low (below 10 ppm), except for high temperatures. The latter also induces an additional consumption of urea due to the direct oxidation of NH_3 by O_2 (see the last column of Table 1.7).

Note that, *in steady state conditions*, if the coverage ratio at the exit point of the catalyst $x(L,t)$ is close to zero then the NH_3-slip is small.

To confirm that the coverage ratio x is the main factor determining the input-output behavior of the dynamics of SCR reactors, we study the impact of the average coverage ratio $\left(\frac{1}{L}\int_0^L x(s)ds\right)$ on the NO_x reduction efficiency. Figure 1.9 extends the results of Table 1.7. In this figure, the evolution of the NO_x reduction efficiency is represented as function of the coverage ratio, for several temperatures[10]. We also represent two distinct zones separated by a curve $x^{\max,\text{stat}}$ at which the NH_3-slip is equal to 10 ppm .

As it appears in Figure 1.9, the efficiency is increasing with the storage of NH_3, for every given temperature. In fact, this is expected from the kinetics (1.9)-(1.10), which stresses that the reduction capacity of the SCR catalyst is scaled by the value of its storage of NH_3 (x). This variable must be dynamically controlled. However, another aspect must be considered. From an environmental point of view, it is not only desired to maximize the NO_x reduction efficiency but maintaining NH_3-slip within acceptable levels is also very important. The key variable in this perspective is the dosing of urea (u). To achieve our goal, we can not simply use urea in excess. This would induce undesired NH_3-slip (and also generate extra-costs for the user). On the other hand, under-dosing results in insufficient NO_x reduction, and possible failure to meet emission standards. Further, it is also not sufficient to inject a stoichiometric amount of NH_3 with respect to the instantaneous value of the inlet NO_x. This historical open-loop approach of the SCR system has been proposed in Tennison et al. (2004), Willems et al. (2007) and neglects the coverage dynamics. It provides a good efficiency but only after a transition period (which can be quite long) needed to fill the catalyst. Rather, to achieve a high efficiency in all situations, the catalyst must be filled first at the correct average value, and then its coverage ratio should be kept equal to a carefully chosen setpoint. The control strategy will be developed based on a simplified model, the "control model" derived below.

[10]Similar curves can be plotted for variations in the gas velocity, the inlet ratio NO_2/NO_x and the amount of NO_x to be treated. The influence of these variations is of second order with respect to the impact of temperature.

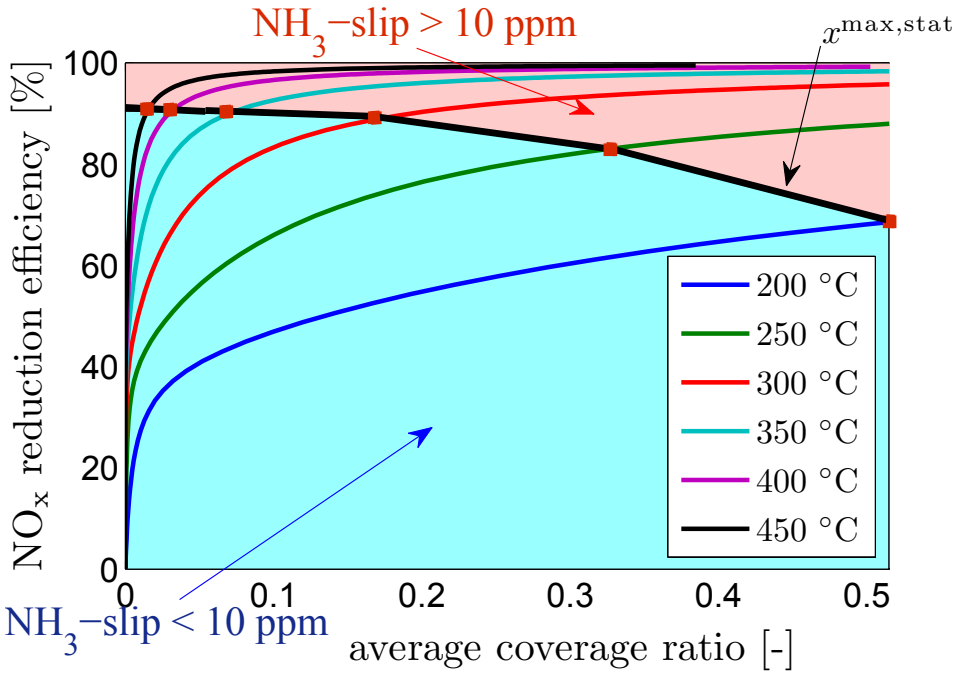

Figure 1.9: Evolution of the NO_x reduction efficiency (η_{NO_x}) as a function of the average coverage ratio for various temperatures. $x^{\max,\text{stat}}$ is the steady state average coverage ratio at which the NH_3-slip is equal to 10 ppm. Steady state solutions of the "reference model" (1.21) for various injection of NH_3, $T \in [200, 450]°C$, $\omega_1 = 150$ ppm, $\omega_2 = 150$ ppm, $v = 5$ m.s^{-1}. Simulation results.

1.4 Derivation of a control model: successive steps of simplifications

We now wish to simplify the "reference model" (1.21) described previously, which will serve for simulation and definition of the setpoint in the sequel, to make it more suitable for control design and analysis. Several steps of simplifications are considered: lumping of distributed parameters, reduction of variables and method of singular perturbations.

1.4.1 Lumping the parameters: from PDE to ODE

This first step of simplification consists in reducing the distributed parameter model into a lumped parameter model. From now, the variables are regarded as spatially homogeneous inside of the catalyst and the phenomena are represented by

ordinary differential equations:

$$\begin{cases} \dot{x} &= k_{\mathrm{a}} z_2 (1-x) - k_{\mathrm{d}}(T)x - k_{\mathrm{s}}(T) z_{11} x - k_{\mathrm{f}}(T) z_{11} z_{12} x - k_{\mathrm{o}}(T) x \\ \dot{z}_{11} &= \frac{v}{L}(\omega_1 - z_{11}) - \Omega k_{\mathrm{s}}(T) z_{11} x - \frac{1}{2}\Omega k_{\mathrm{f}}(T) z_{11} z_{12} x \\ \dot{z}_{12} &= \frac{v}{L}(\omega_2 - z_{12}) - \frac{1}{2}\Omega k_{\mathrm{f}}(T) z_{11} z_{12} x \\ \dot{z}_2 &= \frac{v}{L}(u - z_2) - \Omega k_{\mathrm{a}} z_2 (1-x) + \Omega k_{\mathrm{d}}(T) x \end{cases} \tag{1.22}$$

In these equations, we have chosen notations consistent with the previous model, namely, x is the coverage ratio (adimensional state variable), z_{11} [mol.m^{-3}] is the outlet SCR NO molar concentration, z_{12} [mol.m^{-3}] is the outlet SCR NO_2 molar concentration, and z_2 [mol.m^{-3}] is the outlet SCR NH_3 molar concentration. The variables k_{j}, $j \in \{\mathrm{a}, \mathrm{d}, \mathrm{f}, \mathrm{s}, \mathrm{o}\}$ are the kinetics rates of NH_3 adsoption, NH_3 desorption, "fast" SCR, "standard" SCR and direct oxidation of adsorbed NH_3 by O_2 (defined in (1.7) to (1.11)), respectively. Note that, in this model, the formal expressions of the kinetics rates are identical to those of model (1.21), while the calibration of the pre-exponential factors and of the activation energies differ. Also, one should note that the kinetics rates depend on the gas temperature T (instead of T_s) since the differences between gas and solid temperatures are negligible (as in Lepreux (2009)). A tuning procedure of these parameters has been performed to best reproduce the input-output behavior of the distributed parameters model. ω_1 and ω_2 [mol.m^{-3}] are the inlet molar concentration of NO and NO_2, respectively. L [m] is the length of the catalyst. u [mol.m^{-3}] is the molar concentration of injected NH_3 at the inlet of the catalyst. v [m.s^{-1}] is the gas velocity. The temperature model is also simplified using the average gas temperature of the catalyst (Lepreux (2009)) which is now assumed to satisfy a first order linear time-varying dynamics

$$\tau(v)\dot{T} = -T + T^{in} \tag{1.23}$$

where T_{in} [K] is the temperature at the inlet of the SCR catalyst and the time constant τ depends on the instantaneous gas velocity. In the sequel, the gas temperature T is considered as a disturbance driven by a known input signal T^{in}.

1.4.2 NO and NO_2 lumped into NO_x

Following Upadhyay & Van Nieuwstadt (2006), we lump NO and NO_2 into a single variable. A single reaction rate law (gathering "fast" and "standard" SCR)

is fitted to reproduce the global reduction of NO_x by NH_3:

$$r_r = \underbrace{\frac{k_r^0}{M_{NO_x}} \exp\left(\frac{-E_r}{RT}\right)}_{\triangleq k_r(T)} z_1 \Omega x \tag{1.24}$$

where z_1 [mol.m^{-3}] is the NO_x molar concentration such as

$$z_1 = z_{11} + z_{12},$$

M_{NO_x} [kg.mol−1] is the molecular mass of NO_x, k_r^0 [kg.m^3.mol^{-2}.s^{-1}] is a constant pre-exponential factor, and E_r [kJ.mol^{-1}] is the activation energy. k_r^0 and E_r are tuning parameters employed for the fit. Then, the model (1.22) can be reduced to

$$\begin{cases} \dot{x} &= k_a z_2 (1-x) - k_d(T)x - k_r(T) z_1 x - k_o(T)x \\ \dot{z}_1 &= \dfrac{v}{L}(\omega - z_1) - \Omega k_r(T) z_1 x \\ \dot{z}_2 &= \dfrac{v}{L}(u - z_2) - \Omega k_a z_2 (1-x) + \Omega k_d(T) x \end{cases} \tag{1.25}$$

where ω [mol.m^{-3}] is the inlet molar concentration of NO_x ($\omega = \omega_1 + \omega_2$). In the sequel, for sake of conciseness, the dependence on temperature of the kinetics constants is not explicitly mentioned (rather it is simply noted k_j) but duly accounted for.

1.4.3 Reduction by singular perturbations

Now, a further reduction of the model is performed using the technique of singular perturbations (Tikhonov (1952), Khalil (2002)) to take advantage of the slow/fast nature of the dynamics. In this method, the state variables are separated according to their dynamics: one considers that the fastest ones are at their equilibrium values driven by slow state variables. Considering only the slow state variables, the obtained differential-algebraic system appears as a singular perturbation of the original one. As discussed in § 1.4.1, the average temperature of the catalyst derived from (1.23) is considered as a disturbance, implicitly impacting the kinetics rates of reactions. Thus, we only consider the system (1.25) where each equation is multiplied by $\epsilon = L/\Omega$ (typically here $\epsilon \approx 3.10^{-3}$) to obtain the standard singular perturbation form (Khalil (2002))

$$\begin{cases} \dot{x} &= f(x, z, u, \omega) \quad \text{(slow)} \\ \epsilon \dot{z} &= g(x, z, u, \omega) \quad \text{(fast)} \end{cases} \tag{1.26}$$

where $z = (z_1 \;\; z_2)^T$. Setting $\epsilon = 0$ in this model causes the differential equation $\epsilon \dot{z} = g(x, z, u, \omega)$ to degenerate into a static relation $0 = g(x, z, u, \omega)$ which is exploited to eliminate z from the equations. To be valid, this reduction requires that the fast variables z are promptly converging to an equilibrium value depending on the slow variables x (and the other variables, Tikhonov (1952)). To guarantee this convergence, one has to study the stability of the fast dynamics.

Stability of the fast dynamics As a preliminary, it is easily proved that $\dot{x}$ points inwards on the frontier of $[0, 1]$. Note that for $j \in \{\mathrm{a}, \mathrm{d}, \mathrm{r}, \mathrm{o}\}$, $k_j > 0$. For $x = 0$, one has $\dot{x} = k_\mathrm{a} z_2 \geq 0$; and for $x = 1$, one has $\dot{x} = -k_\mathrm{d} - k_\mathrm{r} z_1 - k_\mathrm{o} \leq 0$. So, for every initial condition $x(0) \in [0, 1]$, $x(t) \in [0, 1]$ for all $t > 0$.

Further, $\forall x \in [0, 1]$, the Jacobian matrix of the fast dynamics is:

$$\frac{\partial g}{\partial z}(x, z, u, \omega) = \begin{pmatrix} -\left(\dfrac{v}{\Omega} + L k_\mathrm{r} x\right) & 0 \\ 0 & -\left(\dfrac{v}{\Omega} + L k_\mathrm{a}(1 - x)\right) \end{pmatrix} \tag{1.27}$$

Clearly, the eigenvalues of the Jacobian triangular matrix are strictly negative. So, for any given x, u, ω the fast dynamics is asymptotically stable (and converges to its equilibrium value implicitly defined by $g(x, z, u, \omega) = 0$).

Fast dynamics equilibrium By introducing $\gamma = \dfrac{v}{L\Omega} > 0$, the equilibrium condition $g(x, z, u, \omega) = 0$ rewrites

$$\left\{ \begin{array}{rcl} 0 &=& \gamma(\omega - z_1) - k_\mathrm{r} z_1 x \\ 0 &=& \gamma(u - z_2) - k_\mathrm{a} z_2 (1 - x) + k_\mathrm{d} x \end{array} \right. \tag{1.28}$$

which is readily solved and gives the unique equilibrium

$$\left\{ \begin{array}{rcl} z_1 = h_1(x, \omega) & \triangleq & \dfrac{\omega}{1 + k_\mathrm{r} x/\gamma} \\ z_2 = h_2(x, u) & \triangleq & h_{21}(x) + h_{22}(x) u = \dfrac{k_\mathrm{d} x/\gamma}{1 + k_\mathrm{a}(1 - x)/\gamma} + \dfrac{1}{1 + k_\mathrm{a}(1 - x)/\gamma} u \\ (z_1, z_2)^T & \triangleq & h(x, u, \omega) \end{array} \right. \tag{1.29}$$

Reduction to the slow dynamics Finally, the system (1.26) can be reduced to its slow dynamics

$$\boxed{\dot{x} = f(x, h(x, \omega, u), u, \omega) = \gamma(u + h_1(x, \omega) - h_2(x, u) - \omega) - k_\mathrm{o} x} \tag{1.30}$$

Importantly, this reduction is valid for all times because the slow dynamics (apart from the external driving variables u, ω, T and v) features an asymptotic stability property which is established by the analysis of its tangent approximation. Indeed, for any equilibrium point $\bar{x} \in [0,1]$ of the reduced system driven by constant signals $\left(\bar{u}, \bar{\omega}, \bar{T}, \bar{v}\right)$, one can compute

$$\begin{aligned} \left.\frac{\partial f}{\partial x}\right|_{\left(\bar{x},\bar{u},\bar{\omega},\bar{T},\bar{v}\right)} &= \gamma \left(-\frac{\bar{\omega} k_{\mathrm{r}}/\gamma}{\left(1 + k_{\mathrm{r}}\bar{x}/\gamma\right)^2} \right. \\ &\quad \left. - \frac{1}{\left(1 + k_{\mathrm{a}}\left(1-\bar{x}\right)/\gamma\right)^2} \left(\left(1 + k_{\mathrm{a}}/\gamma\right) k_{\mathrm{d}}/\gamma + \bar{u} k_{\mathrm{a}}/\gamma \right) \right) - k_{\mathrm{o}} < 0 \end{aligned} \tag{1.31}$$

because $k_j > 0$ for $j \in \{\mathrm{a}, \mathrm{d}, \mathrm{r}, \mathrm{o}\}$, $\gamma > 0$, $\bar{\omega} \geq 0$ and $\bar{u} \geq 0$.

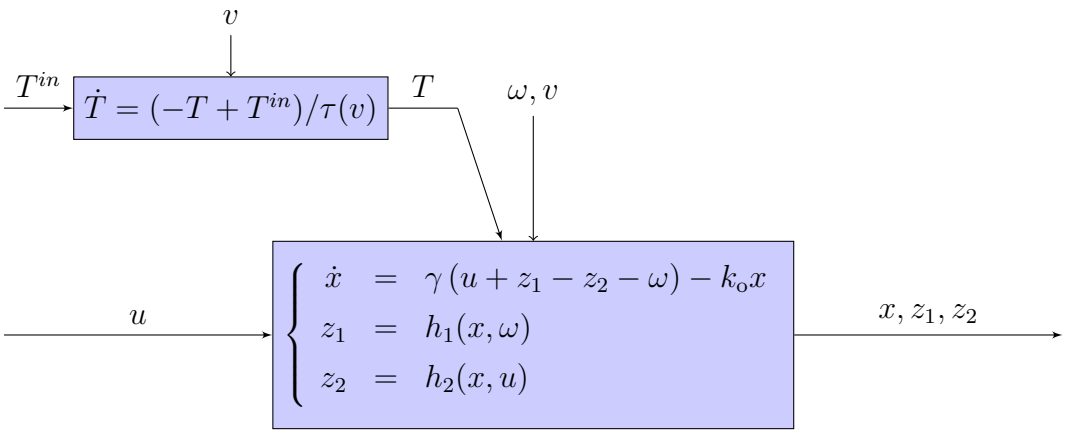

Figure 1.10: Block diagram representation of the differential-algebraic system derived from (1.23), (1.29) and (1.30): the "control model". Recall that γ depends on the gas velocity v while h_1 and h_2 depend on v and on the gas temperature T.

Figure 1.10 depicts, in a block diagram, the system representation that will be used in the sequel for the control design: the "control model". The model has one input u and three bounded and measured disturbances: the inlet SCR temperature T^{in}, the NO_x molar concentration at the inlet of the SCR catalyst ω and the gas velocity v. In this model, only two state variables are considered: the coverage ratio x and the average gas temperature of the catalyst T. Only x will be controlled. The outputs of practical interest are the coverage ratio x, the outlet NO_x and NH_3 molar concentrations, respectively z_1 and z_2, defined by algebraic equations. Their values depend on the state variables and the disturbances.

Chapter 2

Difficulties for the control design

The SCR control problem can be viewed as a problem on the storage of NH_3 which directly and quantitatively defines the capacity of NO_x treatment of the SCR system. This quantity, represented by the coverage ratio x must be constantly in adequacy with the instantaneous values of inlet NO_x (pollutants to be treated), keeping in mind that the target value has to be constantly updated when the temperature varies. Indeed, if the target is set too low, the NO_x reduction is not sufficient. If it is set too high, tracking it rises the risk of massive NH_3-slip, which is directly governed by the thermal behavior of the inlet gas flow (thermal desorption). As a result, some particular cautiousness is required when the system operates in high temperature conditions.

As presented in the preceding chapter, the amount of NO_x to be treated, the inlet temperature and the inlet gas flow are bounded and measured disturbances. The NH_3 coverage ratio is a state governed by the control, the injection of NH_3. The measurement used in a closed-loop is a NO_x sensor at the outlet of the SCR catalyst.

One can imagine that this setup should allow one to easy control the coverage ratio and thus ensure an optimum operation of the SCR. Unfortunately, the employed sensor is sensitive to present NH_3. This is a well documented limitation of the current industrial NO_x sensor technology. This sensitivity disturbs the feedback loop and is the main reason why it is difficult to provide an effective treatment of NO_x while limiting the emissions of residual NH_3 (NH_3-slip).

In this chapter, we discuss these two issues:

i. working with industrial NO_x sensors providing biased measurements;

ii. choosing an appropriate target for the catalyst state variable to guarantee NO_x reduction efficiency while avoiding temperature related malicious effects.

2.1 Difficulty 1: working with an industrial NO_x sensor

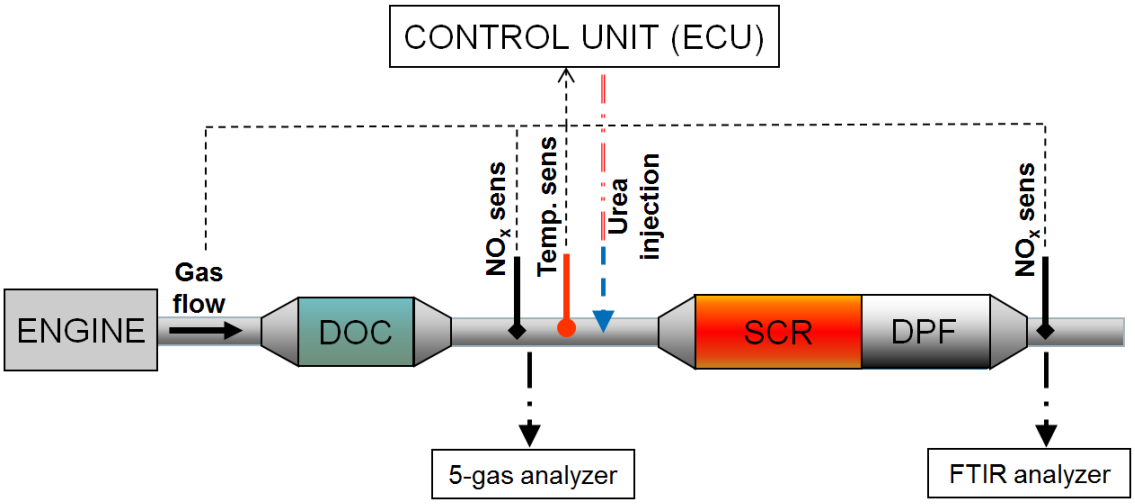

Figure 2.1: Exhaust aftertreatment system of the considered experimental setup.

2.1.1 Sensor implementation in the experimental setup

Figure 2.1 pictures the experimental setup under consideration in this thesis. The considered exhaust line is composed of a diesel oxidation catalyst (DOC), a SCR catalyst (in this study two different catalysts are used: a Fe-zeolite and a Cu-zeolite), and a diesel particulate filter (DPF). The SCR catalyst is 8 inch long (L) for the Fe-zeolite and 9 inch long for the Cu-zeolite, has a diameter D of 2.5 inch and a NH_3 storage capacity Ω of 70 mol/m^3 for the Fe-zeolite and 160 mol/m^3 for the Cu-zeolite. The exhaust gas flow rate, the measurements from the inlet SCR temperature sensor and the two NO_x sensors are available to the ECU, as is pictured in Figure 2.1. On this test, bench temperatures along the exhaust line, as well as two gas analyzers, are available for analysis purposes: a 5-gas analyzer is located upstream of the catalyst and a FTIR analyzer (Fourier Transform InfraRed spectroscopy) downstream of the catalyst. These two high fidelity analyzers are used to measure the upstream SCR tailpipe NO_x emissions and the downstream SCR tailpipe NO_x and NH_3 emissions. They serve as absolute references (since they do not have any cross-sensitivity), but they are not used in the algorithms implemented on the ECU. Finally, a single actuator (urea injector) is located upstream of the SCR catalyst.

2.1.2 NO_x sensor technologies and induced problems

2.1.2.1 Operation principle

In our setup, two identical VDO/NGK UniNO_x sensors (see Laemmerhirt et al. (2010) for a complete description) are used to measure the NO_x molar concentration upstream and downstream of the SCR system. These sensors are state-of-the-art industrial sensors. In this field, there does not exist any alternative technology. Therefore, the discussion which follows is relevant for any existing industrial NO_x sensor.

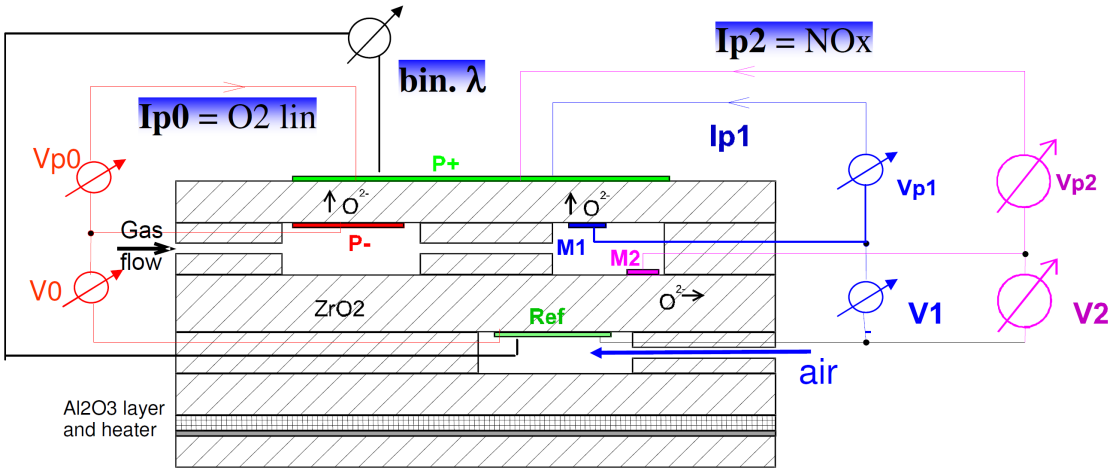

Figure 2.2: Schematic representation of the internal structure of a VDO/NGK UniNO_x sensor (source Walde & Nakasone (2007)).

The VDO/NGK UniNO_x sensors are of the ZrO_2-based multilayer sensor type, and are referred to as "amperometric sensors with multi-electrodes system". As presented in Kato et al. (1998, 1999), they use electro-chemical oxygen pumps (Goodenough (1997)). A schematic view of their structure (Walde & Nakasone (2007)) is given in Figure 2.2. They are composed of two cavities containing, respectively, one and two electrochemical devices consisting of an electrochemical sensor associated with an amperometric sensor (indexed 0, 1 and 2). This sensor works according to the following principles:

i. The exhaust gases to be analyzed are introduced into a first cavity containing a first electro-chemical oxygen pump in which the oxygen partial pressure (value of the potential V0 between P- and Ref) is measured. Then, the potential Vp0 is adjusted (imposed variation) to regulate the oxygen partial pressure (oxygen is removed through the porous wall), which is directly proportional to the current Ip0 (established under the effect of Vp0). The O_2 flow between

the two cavities is then known and set. This regulation allows to oxidize HC, CO and NH_3 in the first cavity.

ii. In the second cavity, another electro-chemical oxygen pump further lowers the oxygen molar concentration. Indeed, the current Ip1 is imposed (in accordance to the value of the current Ip0) by adjusting Vp1 (the voltage is imposed and the current is measured) to deplete oxygen in the second cavity (leading to an almost oxygen-free atmosphere). The measurement of the potential V1 between M1 and Ref electrodes allows one to check the residual oxygen content. This oxygen depletion is required to ensure the selectivity of the measurements of the NO_x molar concentration (on the electrode M2).

iii. The current Ip2 results from the reduction of NO and NO_2, and the pumping through the porous wall of oxide ions (O^{2-}) toward P+, which is achieved by adjusting the voltage Vp2 (between M2 and P+). The voltage V2 between M2 and Ref serves as a reference to set the potential Vp2. As a result, the measurement of the pumping current Ip2 is directly proportional to the emitted oxygen (from the reduction of NO and NO_2) and therefore to the NO_x molar concentration in the exhaust.

Note that a heated platinum element is placed at the bottom of the sensor to guarantee the activation of the reactions (around 600°C) and a good conduction of the oxide ions.

The technical specifications provided by VDO/NGK indicate an accuracy, given in terms of three standard deviations[1] (3σ), of $\pm$ 10% for NO_x emissions above 100 ppm and of 10 ppm below 100 ppm, with a rise time[2] (τ_m) of approx. 3 seconds.

2.1.2.2 Cross-sensitivity

Frobert et al. (2013) have experimentally detected that the NO_x sensor described above is sensitive to several species which are frequently contained in the exhaust gas: HC, HNCO, N_2O and *importantly* NH_3.

In theory, during normal operations of the engine, HC are oxidized in the DOC and do not impact the SCR system. During DPF regenerations (refer to Lepreux (2009) for a description of this thermal reaction), if the SCR catalyst is located upstream of the DPF (as in Figure 2.1), then the SCR is fed by additional HC, which requires to stop SCR operations during these phases. Otherwise (if the DPF is located upstream of the the SCR), no additional precautions are required. As a summary of this discussion, the amount of HC can be considered as negligible here.

[1] In the normal (or Gaussian) distribution, about 99.7% of the values are within three standard deviations (3σ) away from the mean.

[2] Time required for a signal to evolve from 10% to 90% of its final value.

According to our own experiments (not detailed in this thesis), the decomposition of urea can be considered to be complete. Thus, the amount of HNCO is negligible.

The formation of N_2O in the Fe-zeolite SCR catalyst is always considered as negligible as is explained in Devadas et al. (2005). One should note that this is not the case with a Cu-zeolite catalyst. However, the impact of N_2O on the NO_x sensor

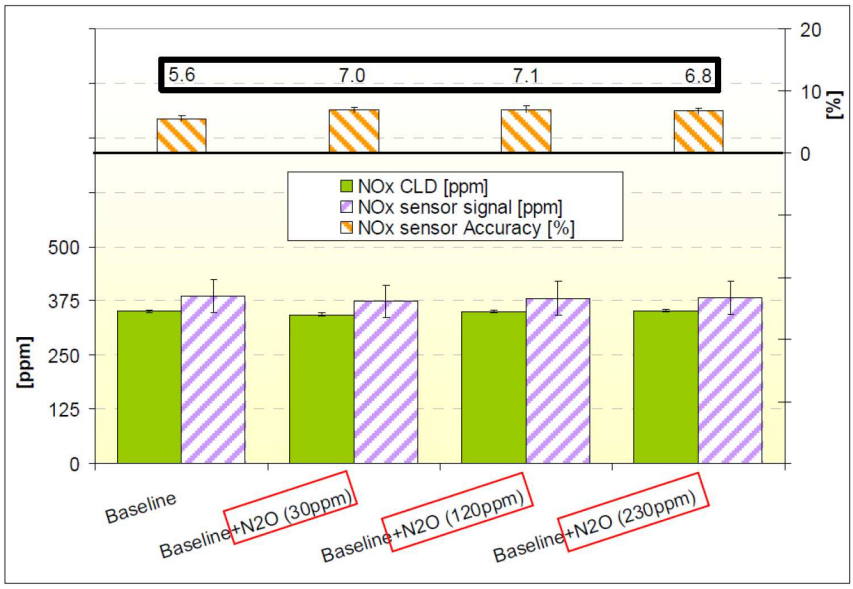

Figure 2.3: N_2O cross-sensitivity of a VDO/NGK UniNO_x sensor for several gaseous blends (Frobert et al. (2013)). The various values of the cross-sensitivity factor are boxed in black. The measurements of the NO_x sensor are depicted as well as those obtained with chemical luminescence detection (CLD). Experimental results.

measurement is not major as pictured in Figure 2.3. Its impact has been tested for three different molar concentrations of N_2O (30, 120, 230 ppm) in a feed gas containing water, oxygen and 350 ppm of NO. The measurements of the NO_x sensor are compared to those obtained with a reference analysis method, the chemical luminescence detection (CLD). This figure also shows that the impact of N_2O on the NO_x sensor can be ignored whatever its concentration, since its cross-sensitivity factor is less than 7%.

Leaving all these species outside of the discussion, we now focus on NH_3. The inlet NO_x sensor measurement is not polluted by NH_3 since it is located upstream of the injector. However, a mismanagement of the coverage induces the possible presence of NH_3 at the outlet of the catalyst. As shown in Figure 2.4, the estimated NO_x molar concentration is significantly impacted by the presence of NH_3 in the exhaust gas. The cross-sensitivity of NH_3 is also described in Schär et al. (2006),

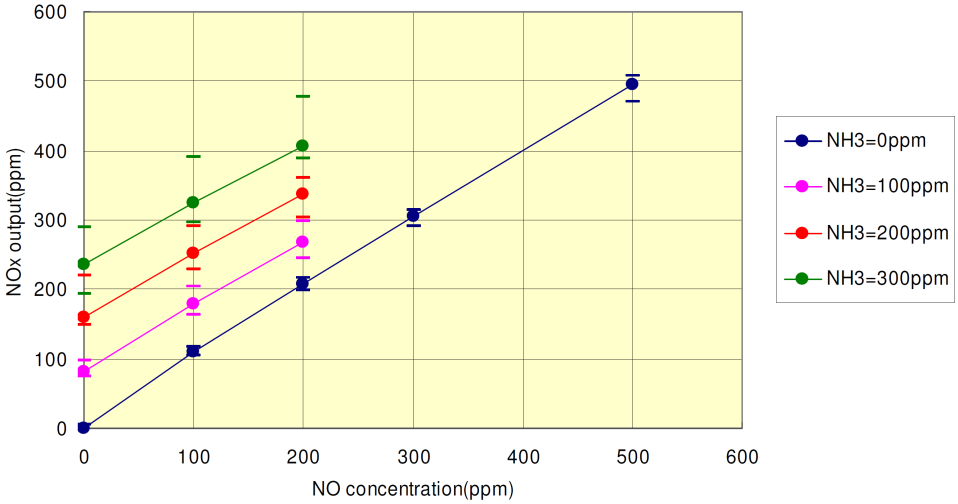

Figure 2.4: NH_3 cross-sensitivity of a VDO/NGK UniNO_x sensor for several temperatures (source Walde & Nakasone (2007)).

Moos (2005). It is due to a bias in the measurement of the current Ip2 (see § 2.1.2.1 for the description of this current). The causes are as follows. Due to the excess of oxygen, NH_3 is oxidized to N_2O, NO or NO_2 in the first cavity of the sensor according to the following reactions

$$4NH_3 + 4O_2 \rightarrow 2N_2O + 6H_2O \quad (2.1)$$
$$4NH_3 + 5O_2 \rightarrow 4NO + 6H_2O \quad (2.2)$$
$$4NH_3 + 7O_2 \rightarrow 4NO_2 + 6H_2O \quad (2.3)$$

In the second cavity, the additional N_2O, NO and NO_2 (produced by (2.1), (2.2) and (2.3), respectively) are reduced and the resulting O_2 is removed by the oxygen pump. This induces a positive bias of the NO_x sensor measurement (i.e the cross-sensitivity factor).

In the following, the cross-sensitivity factor of NO_x sensors with respect to NH_3 is denoted α. Based on the NH_3 oxidation reaction (2.1), one can note that if NH_3 is completely oxidized into N_2O, the cross-sensitivity factor of the NO_x sensor is 0.5. Indeed, 2 moles of NH_3 can introduce 0.5 extra mole of O_2 to the oxygen sensor when the N_2O is reduced into N_2 and O_2 in the second cavity, and the extra 0.5 mole of oxygen corresponds to 1 mole of measured NO_x which therefore causes a cross-sensitivity factor of 0.5. On the other hand, when the NH_3 oxidation produces NO according to (2.2), a cross-sensitivity factor of 1 can be derived using the same reasoning. Accordingly, a cross-sensitivity factor of 2 is expected when the reaction (2.3) dominates the NH_3 oxidation process. Table 2.1 summarizes values of the

Table 2.1: Summary of the cross-sensitivity factor α depending on the species which is reduced in the second cavity.

Species reduced in the 2nd cavity	α
N_2O	1/2
NO	1
NO_2	2

cross-sensitivity factor depending on the species which is reduced in the second cavity. Gathering all these possible effects, it is possible to write (as in Hsieh & Wang (2010b)):

$$1/2 \leq \alpha \leq 2 \tag{2.4}$$

In theory, the cross-sensitivity factor depends on the competitions and therefore on the activation energies of the three reactions. It also depends on the first cavity operating temperature for this reason. Interestingly, experimental data obtained

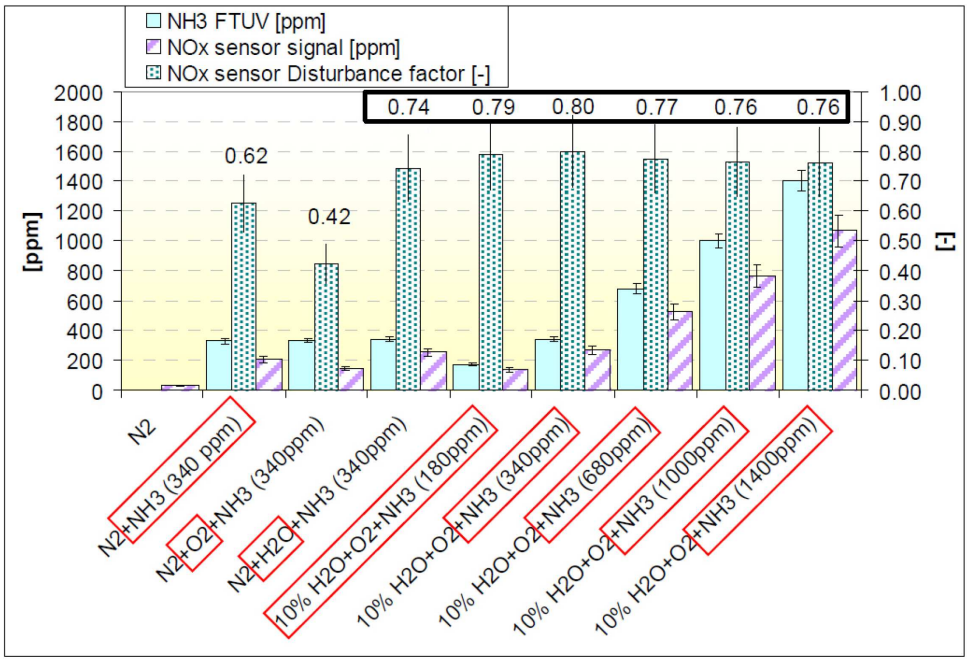

Figure 2.5: NH_3 cross-sensitivity of a VDO/NGK UniNO$_x$ sensor for several gaseous blends (Frobert et al. (2013)). The various values of α are boxed in black. The two first blends are not considered in the calculation of α since there is always oxygen and water steam in exhaust gases. Experimental results.

in a synthetic gas bench and reported in Figure 2.5 show that the cross-sensitivity factor can be approximated by a constant value (in the reported case $\alpha \approx 0.77$). This fact is enabled by the selectivity of the employed materials in the sensor and by the embedded low-level controller which regulates and therefore limits the variability of the sensor internal temperature.

2.1.2.3 NO_x sensor model

In summary of the preceding discussion, the following model of NO_x sensor is proposed

$$y = z_1 + \alpha z_2 \tag{2.5}$$

In this thesis, α is considered to be a constant value equal to 0.77 in accordance with the experimental values presented in Figure 2.5. This simplifying assumption could be called into question if a better knowledge/model of the cross-sensitivity were available in the future.

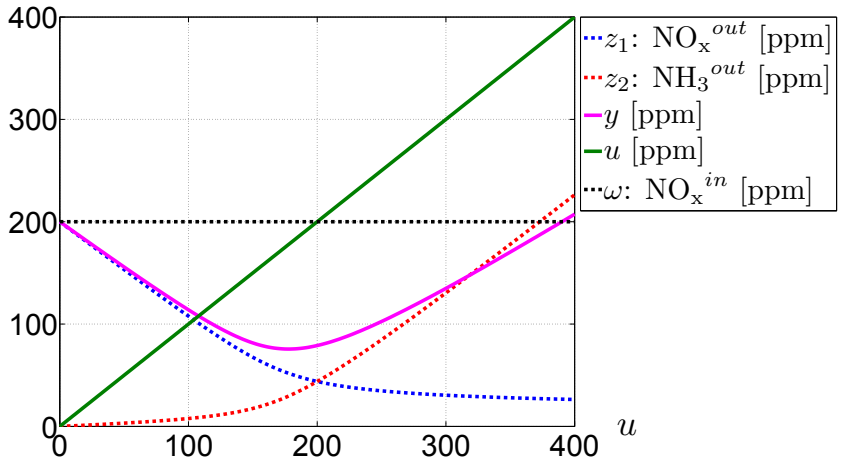

Figure 2.6: Outlet NO_x sensor response to increasing NH_3 injection at the inlet of the catalyst (steady state). The inlet SCR temperature, the gas flow rate and the NO_x inlet molar concentration are respectively set to 300 °C, 100 kg/h and 200 ppm. Simulation results.

In Figure 2.6, based on the proposed NO_x sensor model, the steady state values of z_1 (outlet NO_x) and z_2 (outlet NH_3) are represented as functions of u (inlet NH_3 injection), and are compared against the output equation y. It is shown that while u is increased, z_1 decreases (NO_x are reduced) and z_2 increases (NH_3-slip increases). As a result, y is non monotonic: it is close to z_1 when z_2 is small, but largely corrupted when z_2 becomes significant (i.e. NH_3-slip becomes overwhelming).

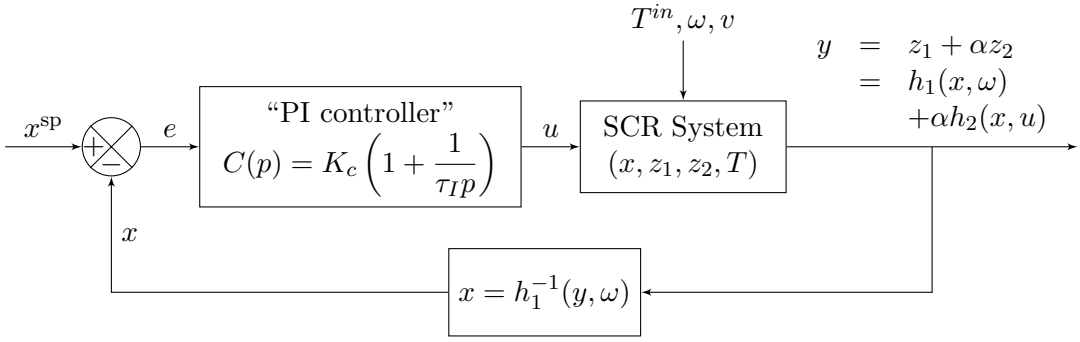

Figure 2.7: Block diagram representation of a SCR closed-loop using a PI controller. Recall that h_1 and h_2 depends on the gas velocity v and on the gas temperature T.

One can easily realize that the cross-sensitivity is troublesome for feedback control purposes. To illustrate this point, a simple PI controller (Figure 2.7) is developed and tested in simulation. This study is made on the simple "control model" as synthesis, control and simulation model (which is a favorable test case). Two cases are considered:

i. an ideal NO_x sensor ($\alpha = 0$) providing a measurement which is a monotonic function of the coverage ratio x. The simulation results are reported in Figure 2.8. This figure illustrates the evolution of x^{sp}, x and u as functions of time, for a fixed operating condition ($NO_x = 100$ ppm, $v = 5.5$ m.s^{-1}, $T = 250$°C). At time $t = 100$ s, a step on the coverage ratio setpoint x^{sp} is per-

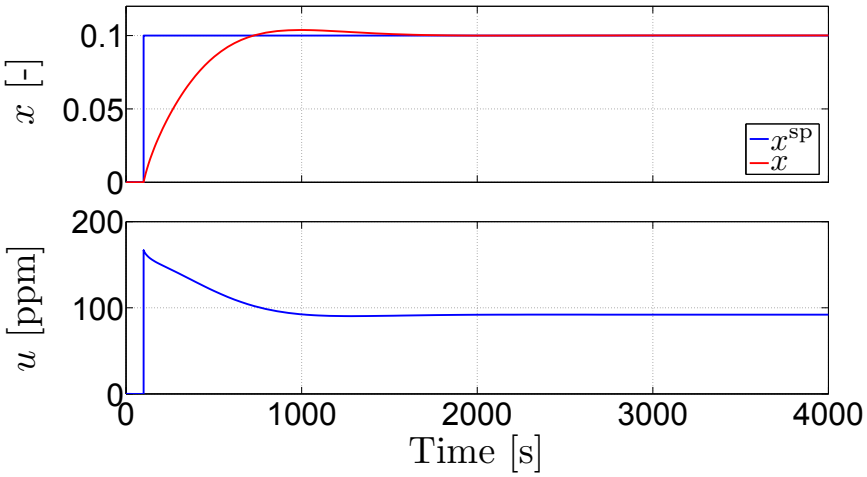

Figure 2.8: Performance of a PI controller for the "control model" with an ideal NO_x sensor. Histories of x^{sp}, x and u for a given operating condition: $NO_x = 100$ ppm, $v = 5.5$ m.s^{-1} and $T = 250$°C. Simulation results based on model (1.25).

formed. Due to the proportional relation between y and x, the PI controller works well and the coverage ratio x kindly tracks its setpoint x^{sp}.

ii. a realistic NO_x sensor, which is cross-sensitive to NH_3 (cross sensitivity factor $\alpha = 0.77$). As illustrated in Figure 2.6, the output y is a non-monotonic function of the coverage ratio x. In Figure 2.9, the (poor) performance of the developed PI controller is reported. Counter-intuitively, an increasing coverage ratio does not necessary lead to a decreasing measurement y. Due to this cross-sensitivity and using a simple PI controller the coverage ratio x does not converge to its setpoint x^{sp}. The control variable u diverges but x does not, it is bounded by 1 by definition.

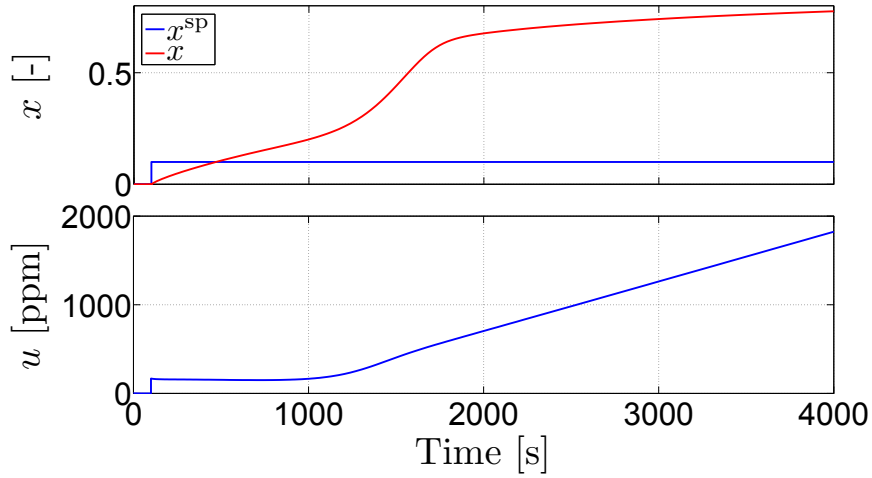

Figure 2.9: Performance of the PI controller for the "control model" with a NO_x sensor cross-sensitive to NH_3. Histories of x^{sp}, x and u for a given operating condition: $NO_x = 100$ ppm, $v = 5.5$ m.s^{-1}, $T = 250$°C, $x^{sp} = 0.1$. Simulation results based on model (1.25).

2.2 Difficulty 2: choosing a setpoint

In this section the (arbitrary) choice of the coverage ratio setpoint x^{sp} is discussed. As already explained in § 1.3.5, maintaining large values of x allows to reach high levels of NO_x reduction efficiency, but increases the risks of NH_3-slip (especially in case of thermal desorption). In the following, we get a bit deeper into this question and study first whether the spatial distribution of the coverage ratio has an impact on the NO_x reduction efficiency and on the NH_3-slip. At the light of this study, the choice of the coverage ratio setpoint is discussed. This study is realized using the (spatially distributed) "reference model" (1.21) which is spatially

discretized (for numerical implementation) into ten equal zones using a backward finite difference method. The conclusion is that representing the setpoint as a constant parameter for a lumped state is sufficient. Then, we explain how this constant value should be chosen.

2.2.1 Have we missed the definition of an interesting target by lumping the parameters?

Considering the spatially distributed nature of the SCR system, a natural question is: should the coverage ratio target be chosen as a constant (equal to the average coverage ratio corresponding to an equilibrium profile) or a spatially varying profile? A spatially varying profile may be either a constant equilibrium profile or a non equilibrium (so non constant) profile. If a non constant profile produces better efficiency and less NH_3-slip, then we could have to reconsider our lumping reduction. In particular, the nonlinearities coming into play may promote the non constant profile as a potentially appealing target. To address this question, we propose a numerical experiment where we force the system into a periodic regime.

We want to obtain a coverage profile for which ammonia is predominantly stored near the entry of the catalyst. Indeed, we believe that this kind of profile could improve the robustness towards the thermal desorption (fast increase of the temperature which potentially induces NH_3-slip). Therefore, the system response resulting from the application of a periodic signal on the control variable u is studied in simulation. A spatially discretized version of the "reference model" is used. The amount of inlet NO_x is fixed to 300 ppm, the exhaust gas velocity v is 5 $m.s^{-1}$

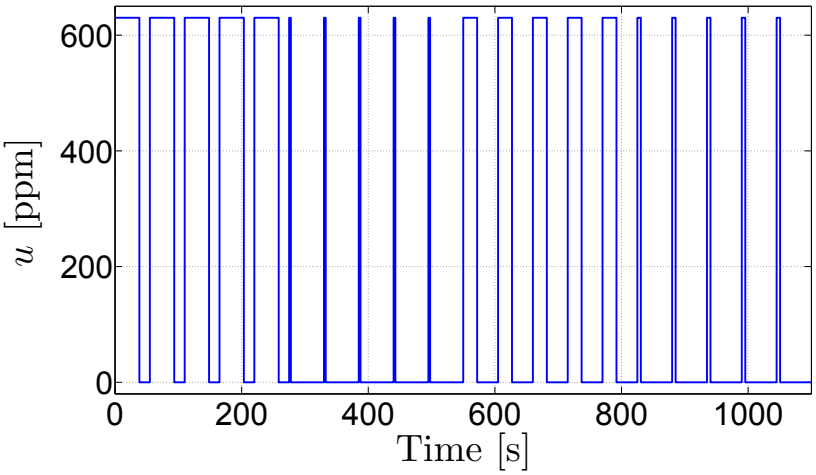

Figure 2.10: Sequence applied to the control input u. Simulation results.

and the temperature at the catalyst inlet T is 250 °C. The sequence defined in the Figure 2.10 is repeated in time, and then applied to the control variable u (NH_3 injection). The system converges to a periodic regime. The average efficiency and NH_3-slip are evaluated and compared to those obtained with a constant injection having the same average value.

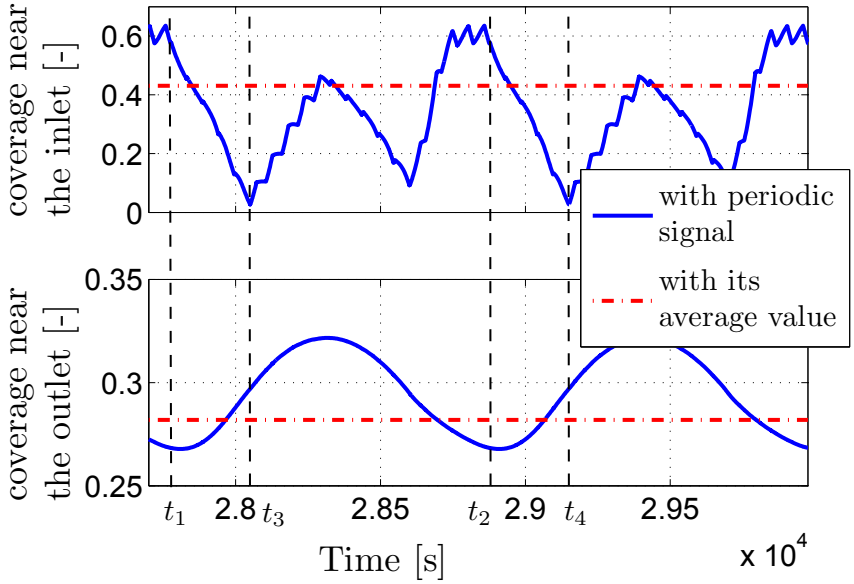

Figure 2.11: Evolution of the coverage ratios near the inlet and near the outlet resulting from the application of a periodic signal on u (blue) and its average value (red), as functions of time. Stationary operating conditions (ω = 300 ppm, v = 5 m.s^{-1} and T = 250 °C). Simulation results.

Figure 2.11 reports the histories of the coverage ratio near the inlet and near the outlet of the system, for the two different situations (periodic signal on u (blue) and its average value (red)). As expected, one notes that the average coverage ratio oscillates about the value obtained with a constant input signal.

Figure 2.12 reports the spatially-distributed coverage ratio evolution in response to the periodic signal on u. In addition, Figure 2.13 shows the resulting NH_3-slips and the NO_x reduction efficiency (η_{NO_x}). As it appears, a non-stationary coverage ratio profile for which NH_3 is predominantly stored near the inlet of the catalyst yield periodically varying NH_3-slip. Indeed, at about $t_1 = 2.78\ 10^4$ s and $t_2 = 2.88\ 10^4$ s in Figure 2.11, the coverage ratio is about 0.6 near the inlet, 0.27 near the outlet and the NH_3-slip is 8 ppm. However, the system moves periodically too far from the interesting profile, e.g. at $t_3 = 2.81\ 10^4$ s and and $t_4 = 2.92\ 10^4$ s where the coverage ratio near the inlet is almost zero and is about 0.3 near the outlet. This temporary

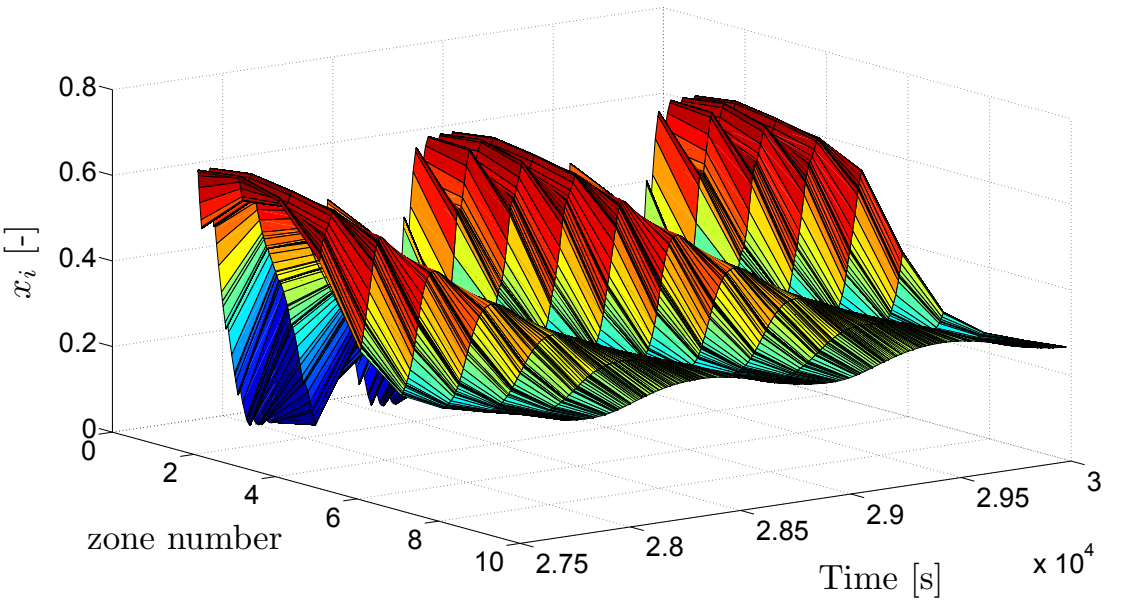

Figure 2.12: Spatially-distributed coverage ratio evolution, induced by the application of a periodic signal on u. Stationary operating conditions ($\omega = 300$ ppm, $v = 5$ m.s^{-1} and $T = 250$ °C). Simulation results.

profile leads to a peak of NH_3-slip of 16 ppm. Figure 2.13 (bottom) shows that the average NO_x reduction efficiency is close to the one obtained with a constant signal (its average value is 79.4%). The variations of the total efficiency are negligible while the coverage ratio profile is highly varying. From this, we (arbitrarily) conclude that there is a very weak dependence of the NO_x reduction efficiency on the magnitude of the periodic variations of the coverage ratio profile: it is the total amount of stored NH_3 which mostly defines the efficiency.

A periodic evolution of the NH_3-slip is also observed. The average value of the outlet NH_3 is almost unchanged (it is slightly deteriorated) but its maximum value (peak of NH_3-slip) is much greater.

Further, some temporary non equilibrium profiles are studied. They are represented by a parameter β which defines the slope of the spatial variation of the profile. β is varied between 0 and 0.065. Four such curves are pictured in Figure 2.14 as well as the equilibrium coverage ratio profile. All these chosen coverage ratio profiles share the same amount of stored NH_3 (their integrals are the same). This family of curves is tested in simulation. The amount of upstream NO_x is set at 300 ppm and the exhaust gas velocity v is set at 5 m.s^{-1}. At the initialization of the simulation, an arbitrary coverage ratio profile is selected and u is set to zero. Five different

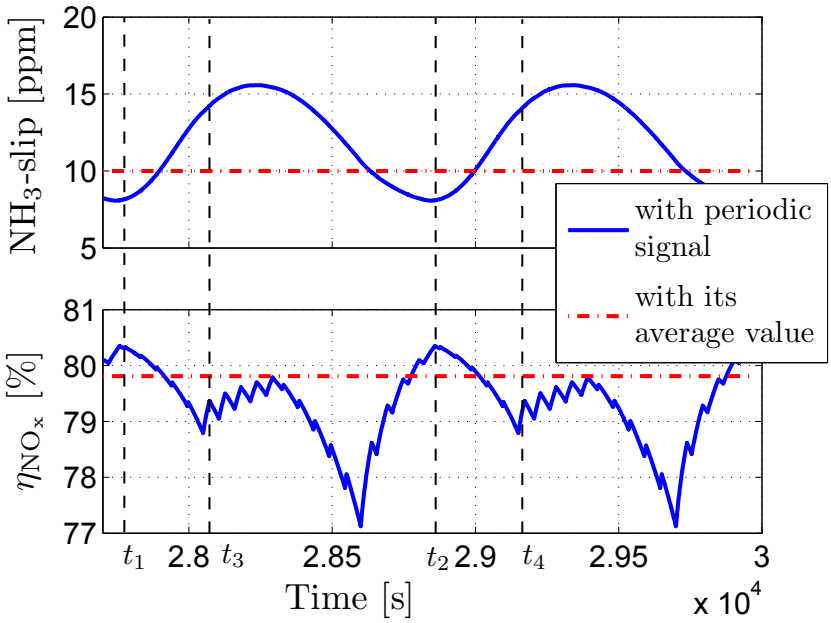

Figure 2.13: Histories of NH_3 at the outlet of the SCR catalyst (NH_3-slip) and the NO_x reduction efficiency, induced by a periodic signal on u (blue) and its average value (red). Stationary operating conditions ($\omega = 300$ ppm, $v = 5$ m.s^{-1} and $T = 250$ °C). Simulation results.

simulations (initial conditions $x_{i,eq}$ and $x_{i,j}$, $j \in \{1, 2, 3, 4\}$) are performed and the results are presented in the sequel.

From the chosen initialization, the coverage ratio profile evolves from $t = 0$ since it is a non-stationary point. At $t = 100$ s, a step on the temperature (from 250°C to 300°C) is applied at the input of the catalyst (Figure 2.15, top). The propagation of the temperature along the catalyst induces a change in the coverage ratio profile: the adsorbed NH_3 desorbs, travels from upstream to downstream of the catalyst and is eventually emitted into the atmosphere. Figure 2.15 (bottom) reports the evolution of the NH_3 downstream of the catalyst for various initializations of the coverage ratio profile.

If it were possible to maintain a profile as defined by $\beta = 0.065$ in the Figure 2.14, the amount of NH_3 released into the atmosphere during fast rise of temperature would be significantly reduced as it appears in Figure 2.15 (bottom). However, as previously discussed, the periodic regime necessarily obtained in order to achieve such a profile (since it is a non constant profile) implies, periodically, adverse situations (e.g. NH_3 being rather stored near the outlet of the catalyst). It is therefore necessary to reason in a time averaging fashion and the conclusion is already known:

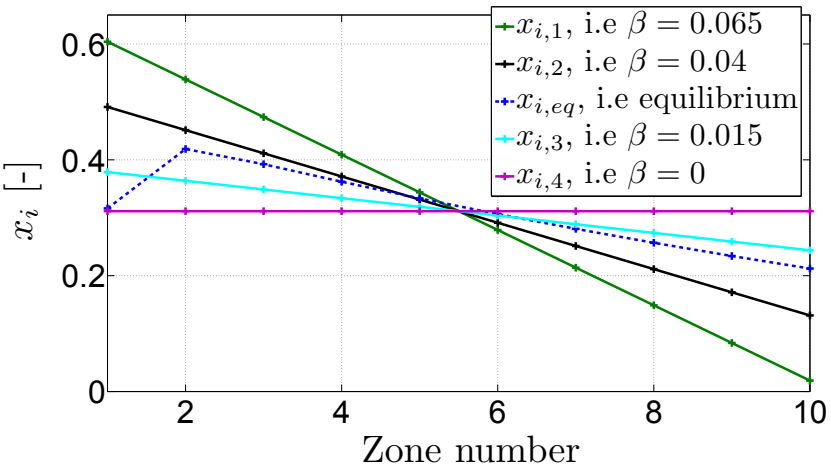

Figure 2.14: Representation of the equilibrium coverage ratio profile ($x_{i,eq}$) and four arbitrary unstationary profiles ($x_{i,j}$, $j \in \{1, 2, 3, 4\}$) for a slope $\beta = 0.065$, 0.4, 0.15 and 0 (stationary operating conditions: $\omega = 300$ ppm, $v = 5$ m.s^{-1} and $T = 250$ °C). Simulation results.

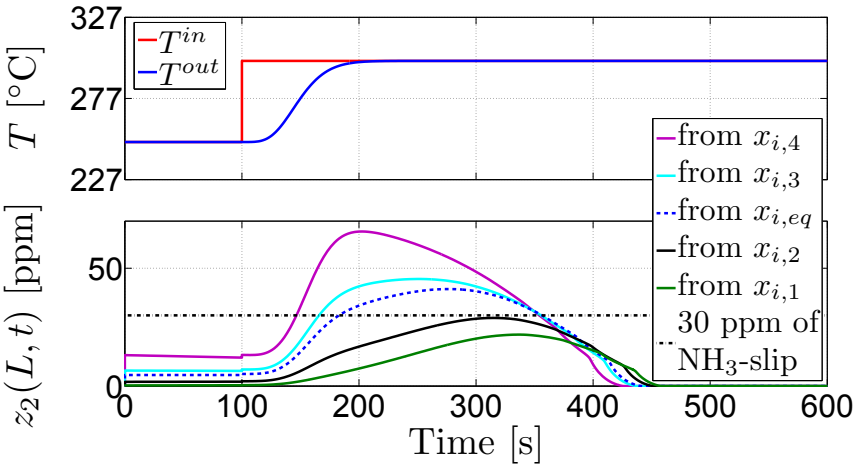

Figure 2.15: Evolution of NH_3 molar concentration at the outlet of the catalyst (NH_3-slip) as a function of time, in response to a step on the inlet temperature (from 250°C to 300°C) and for the five initial conditions ($x_{i,eq}$ and $x_{i,j}$, $j \in \{1, 2, 3, 4\}$). The gas velocity and the inlet amount of NO_x are fixed, $v = 5$ m.s^{-1} and $\omega = 300$ ppm, respectively. Simulation results.

a spatially varying profile is a non viable target for the coverage ratio. The average effects are not beneficial, the peaks are higher and not desirable.

Some analytic calculations given in Appendix B support the observations made in simulation. It is proved that with a linear model of the SCR catalyst stemming from a spatially discretization in two equal parts of the "control model", the system can reach any arbitrary point or asymptotic regime (since it is controllable). However, the average of the coverage ratios obtained is identical to the ones at equilibrium. Again, the periodic changes of the coverage ratio profile lead to a deterioration of the system performance in terms of maximum NH_3-slip, the average level being unchanged, and the maximum being larger.

Considering the conclusions above, we now come back to our lumped representation of the dynamics and define a suitable target point for it.

2.2.2 Setpoint mapping

Here, we now explain how one should set the target value x^{sp} for the coverage

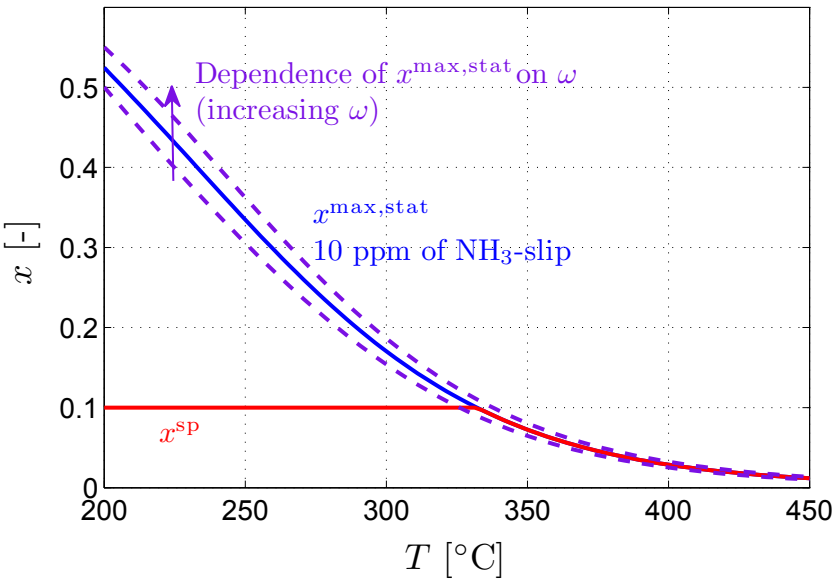

Figure 2.16: Maximum average coverage ratio yielding less than 10 ppm of NH_3-slip ($x^{\mathrm{max,stat}}$) and desired setpoint map (x^{sp}) as functions of temperature. The dependence of $x^{\mathrm{max,stat}}$ on ω is depicted as function of temperature. Simulation results.

ratio x. First, we determine a value above which the NH_3-slip gets higher than 10 ppm (at steady state). The boundary of this domain is computed as steady state solutions of the distributed parameter system (1.21) for temperatures ranging in [200, 450]°C. The employed methodology consists, for each operating condition (ω, T and v being fixed), in finding the steady state input u and therefore the coverage ratio x such that NH_3-slip = 10 ppm. In Figure 2.16, the average of these spatially varying values over the catalyst length $\left(\frac{1}{L}\int_0^L x(s)ds \triangleq x^{\max,\text{stat}}\right)$ is reported as a function of the temperature only (ω and v being fixed). Indeed, the temperature plays the most significant role among the parameters. Figure 2.16 illustrates that $x^{\max,\text{stat}}$ weakly depends on the inlet NO_x (ω), for usual values ($\omega \in [10, 500]$ ppm). The impact of the gas velocity v is also weak.

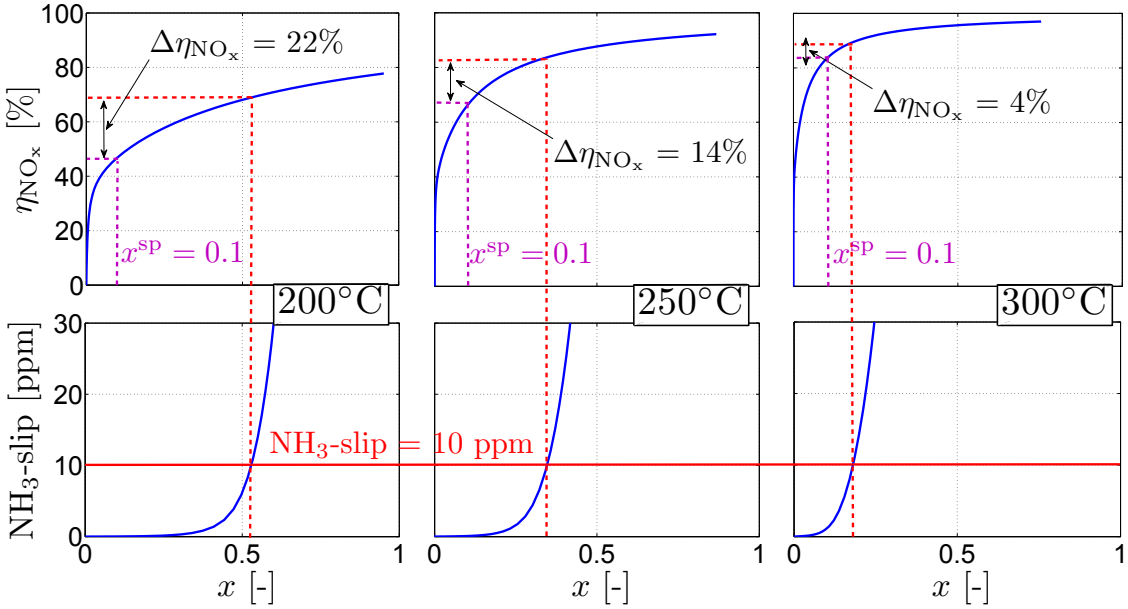

Figure 2.17: NO_x reduction efficiency (η_{NO_x}) and NH_3-slip as functions of the average coverage ratio for various temperatures (T = 200°C, 250°C and 300°C). In each situation the impact on the efficiency of limiting x^{sp} to a lower value is reported (absolute variation of the NO_x reduction efficiency $\Delta\eta_{NO_x}$). Simulation results.

By definition, x^{sp} should not be chosen greater than $x^{\max,\text{stat}}$. Moreover, to prevent possible large NH_3-slip during temperature transients (thermal desorption), x^{sp} is further limited to a much lower value (typically 0.1) for low temperatures (at the expense of a slightly detrimental impact on the efficiency). In Figure 2.17 one reports the detrimental impact on the NO_x reduction efficiency of this limitation for T in range [200, 300]°C. The upper curves depict the NO_x reduction efficiency

(η_{NO_x}) and the three lower ones report the NH_3-slip evolution as functions of the average coverage ratio. As a result, for $T = 200°C$, $250°C$ and $300°C$, the limitation of x^{sp} to 0.1 implies an absolute variation (reduction) of the efficiency of 22%, 14% and 4%, respectively. This appears acceptable.

Saturating the target value x^{sp} at 0.1 for low temperatures [200, 330]°C corresponds to security margins tailored for fast rises in temperature. Indeed, x can be only decreased slowly (by ω when T is fixed, see (1.30) with u saturated to 0), while rises in temperature imply vast decreases of $x^{max,stat}$ (see Figure 2.16). Because desorption can be abrupt, while loading is a slow process, these security margins are needed.

Why saturating x^{sp} to 0.1? Limiting x^{sp} to a constant value for low temperatures is a simple way to take security margins. An alternative way to proceed is to consider a bound $x^{max,dyn}$, computed by considering that the system must be able to deal with known inlet temperature disturbances Δ_T. Such disturbances can be quantified through a statistical analysis of the engine operating conditions. To each operating temperature then corresponds a temperature rise that must be considered to set the maximum available storage at this operating temperature. An example is given in Table 2.2 (for the vehicle considered in this thesis, on NEDC cycles), from which $x^{max,dyn}$ is computed and depicted in Figure 2.18. A much wider set of operating conditions should be considered for a sounded calibration. However, for this simple example, it appears that, in the range [300, 450]°C, the natural decrease of the coverage ratio by NO_x reduction is more important. Here, x^{sp} can be chosen greater than $x^{max,dyn}$ without excessive risk of NH_3-slip.

Table 2.2: Disturbance Δ_T to be rejected for various initial temperatures.

Initial gas temperature [°C]	200	250	300	350	400	450
Disturbance to be rejected Δ_T [°C]	110	70	35	10	2	0

In the sequel, this possibility to consider a bound $x^{max,dyn}$ has not been fully addressed: the target x^{sp} is set as $\min(0.1, x^{max,stat})$.

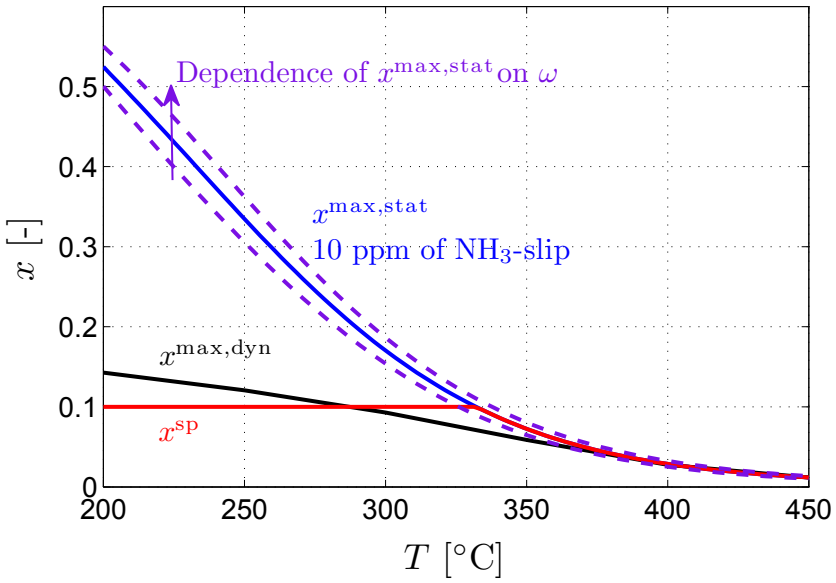

Figure 2.18: Maximum average coverage ratio yielding less than 10 ppm of NH_3-slip ($x^{\max,\text{stat}}$) and desired setpoint map (x^{sp}) as functions of temperature. The dependence of $x^{\max,\text{stat}}$ on ω and the modified $x^{\max,\text{dyn}}$ account for transient temperature variations are depicted as functions of temperature. Simulation results.

Chapter 3

Proposed strategy

In this chapter, we propose a control architecture for the SCR system. This structure is pictured in Figure 3.1. It operates using five connected algorithms, each being described in a particular section.

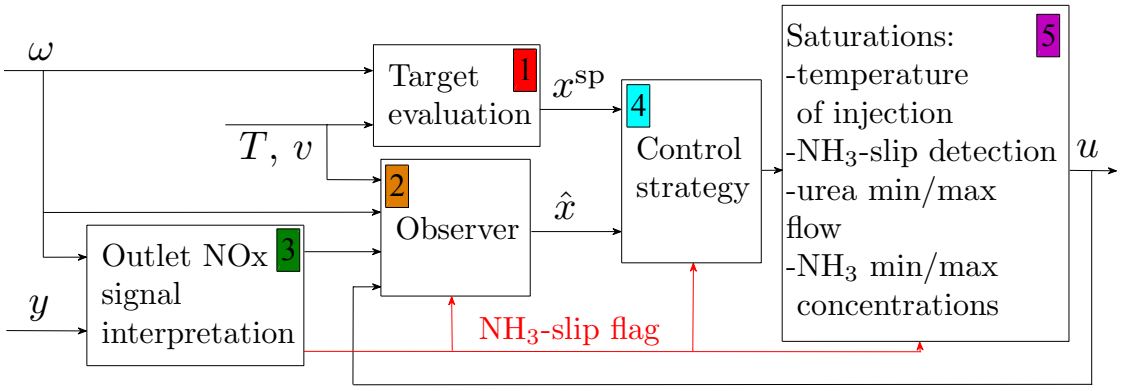

Figure 3.1: Structure of the proposed control architecture. Block (1) corresponds to the determination of the setpoint. Block (2) corresponds to the coverage ratio observer. Block (3) corresponds to the NH_3-slip detection. Block (4) corresponds to the feedback control. Block (5) corresponds to several saturations in accordance with the catalyst and the actuator limits.

The task of this control architecture is to manage the adsorbed NH_3 coverage ratio x. Following our "control model" (1.30), the SCR control problem is simply recast into controlling the following Single Input Single Output (SISO) dynamics

$$\left\{ \begin{array}{rcl} \dot{x} & = & \gamma \left(u + h_1(x,\omega) - h_2(x,u) - \omega \right) - k_o x \\ y & = & h_1(x,\omega) + \alpha h_2(x,u) \end{array} \right. \tag{3.1}$$

where y is the measurement of the downstream NO_x sensor, u is the NH_3 injection at the inlet of the catalyst (control variable), ω is the upstream SCR NO_x molar concentration (measured disturbance), γ is a constant proportional to the gas velocity v (measured disturbance), T is the average temperature of the catalyst (disturbance computed from the measurement of the inlet SCR temperature T^{in} using (1.23)), h_1, h_2 are defined in (1.29) (recall that their dependencies on T and v is not explicitly mentioned but accounted for), k_o is the direct oxidation of NH_3 by O_2 kinetic rate, and α represents the NO_x sensor cross-sensitivity discussed in Chapter 2.

To control this SISO dynamics, a control architecture is proposed. The target x^{sp} for the coverage ratio is determined, using the current engine conditions (T, v) and the amount of NO_x to be treated as inputs (block (1) in Figure 3.1). This setpoint is determined to reach an acceptable efficiency of NO_x reduction while limiting the release of ammonia into the atmosphere (see the discussion in § 2.2).

The estimation of the current coverage ratio x is the second element of the control architecture (block (2) in Figure 3.1). Using the downstream (outlet) NO_x sensor in this observer requires particular caution because of its sensitivity to NH_3. The interpretation of the downstream NO_x sensor signal is the subject of a specific study to guarantee the validity of the measured signal (block (3) in Figure 3.1).

Then, the estimate of the coverage ratio $\hat{x}$ is dynamically forced by the controller (feedback action, block (4) in Figure 3.1) to track the target x^{sp}.

Finally, due to practical implementation issues, several saturations are applied on the AdBlue® mass flow (block (5) in Figure 3.1), to account for the limitations of the catalyst (minimum injection temperature, allowable maximum NH_3 molar concentration) and of the injector (urea injection is positive and upper bounded).

The whole architecture defines an observer-controller consisting in a closed-loop dynamics coupled to an algebraic equation (defining the stabilizing controller). Due to the cross-sensitivity of the sensor, this algorithm has several equilibrium points. The list contains the point of practical interest (providing the desired aftertreatment effects) and artefacts. These artefacts could be very troublesome. A study of their stability is presented and reveals that they are either naturally unstable, discarded by the discrete time implementation of the controller, or ambiguity-free. Therefore, the considered observer-controller can be tuned to guarantee asymptotic convergence toward the point of practical interest. An additional control mechanism is introduced to prevent large NH_3-slip. Prior to experimentations, a robustness analysis of this controller is performed based on simulations.

3.1 Observer synthesis

System (3.1) is SISO. It is clear that y is non invertible with respect to x when $\frac{\partial y}{\partial x} = 0$. Because of this singularity, the system is not uniformly observable. In practice, the analytical expression of this condition bearing on x is not straightforward and a numerical study is needed to determine the roots. Leaving this singularity aside, the proposed observer is defined however, following an output-injection design, as

$$\begin{aligned} \dot{\hat{x}} &= \ell(u, y(x,\omega,u), \hat{x}, \omega) \\ &\triangleq \gamma(u + \underbrace{h_1(x,\omega) + \alpha h_2(x,u)}_{y(x,\omega,u)} - \omega) - k_o \hat{x} - k_L \left(\hat{x} - h_1^{-1}(y,\omega)\right) \end{aligned} \tag{3.2}$$

where $k_L > 0$ is the (constant) observer gain. Implicitly, in this observer design, the role of h_2 is neglected (when we copy the dynamics (1.30)) because the NH_3-slip is neglected (in theory the choice of x^{sp} leads to low levels of NH_3 at the outlet of the catalyst) and h_1 is directly replaced by the measurement y ($= h_1(x,\omega) + \alpha h_2(x,u)$). In (3.2), y is used to calculate a tentative estimate x^c of the coverage, as

$$x^c = h_1^{-1}(y,\omega), \text{ i.e. } h_1(x^c,\omega) = y \tag{3.3}$$

As y is not invertible with respect to x, we have chosen that only the (dominant) part h_1 should be inverted in (3.3) (NH_3-slip is neglected due to the choice of x^{sp} which is never greater than 0.1). As a result, x^c is calculated with the NO_x sensors

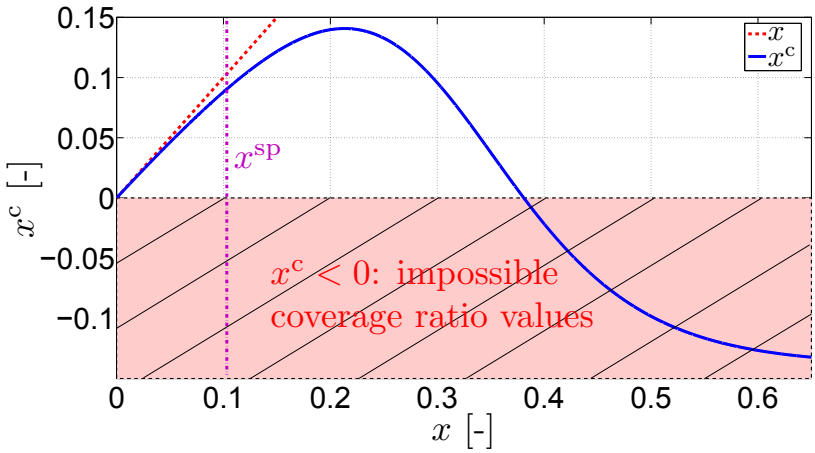

Figure 3.2: Interpreted coverage x^c as a function of x (taken at equilibrium), for $T = 250$ °C, $\omega = 200$ ppm, $v = 4.5$ m.s^{-1} and $x^{sp} = 0.1$. Simulation results.

signals upstream and downstream of the catalyst. This strong simplification yields the mapping represented in Figure 3.2: for low values of x, x^{c} is close to x.

In this figure, for most values of the interpreted coverage x^{c}, the true coverage x can take two distinct values. Out of those two, the desirable one (in terms of control objective) is always the smallest. The real problem is to know, for a given x^{c}, which value has to be considered in the feedback strategy. We now close the loop with this estimate.

3.2 Control strategy

The control strategy is designed to force, if possible, the estimate error dynamics to satisfy $\dot{\hat{x}} = -k_P\,(\hat{x} - x^{\mathrm{sp}})$. The resulting linearizing feedback law has to be saturated for negative values to account for the actuator limitations (and therefore is not achieving linearization for saturated values). The upper limit is not considered since it is in general too high to be reached. This yields

$$\begin{array}{rl} & u - \max\left(0, \omega - y + \dfrac{1}{\gamma}\left[k_{\mathrm{o}}\hat{x} + k_L\,(\hat{x} - x^{\mathrm{c}}) - k_P\,(\hat{x} - x^{\mathrm{sp}})\right]\right) \\ \triangleq & \xi(y(x,\omega,u),\hat{x},\omega,u) = 0 \end{array} \tag{3.4}$$

The closed-loop system consisting of (3.1), (3.2) and (3.4) is

$$\left\{\begin{array}{rcl} \dot{x} & = & f(x, h(x,\omega,u), u, \omega) \\ \dot{\hat{x}} & = & \ell(u, y(x,\omega,u), \hat{x}, \omega) \\ 0 & = & \xi(y(x,\omega,u),\hat{x},\omega) \end{array}\right. \tag{3.5}$$

3.3 Description of closed-loop equilibria

The analysis of the closed-loop equilibria needs to consider, separately, the case of saturated control $u = 0$, which leads to the equilibrium point $(x = 0, \hat{x} = 0)$ (for further details refer to Appendix D.1.1) and the case of unsaturated control which always satisfies $\hat{x} = x^{\mathrm{sp}}$, obtained by substituting the unsaturated control

$$\Phi(y(x,\omega,u),\hat{x},\omega,u) \triangleq u - \omega + y - \frac{1}{\gamma}\left[k_{\mathrm{o}}\hat{x} + k_L\,(\hat{x} - x^{\mathrm{c}}) - k_P\,(\hat{x} - x^{\mathrm{sp}})\right] = 0 \tag{3.6}$$

into the observer dynamics right-hand side $\ell(.)$. Due to the observer convergence (in principle the observer is stable due to the choice of $k_P > 0$, and converges to x^{sp}), we restrict our analysis to the dynamics of x. One shall note that there exists an equilibrium curve of x as a function of k_L. The nature of this equilibrium curve depends on the value of several parameters (see Figures 3.5, 3.6 and 3.7). The stability analysis is more involved.

Generally, the system has one or three equilibrium points, solely depending on the value of k_L. Indeed, for a given $x \in [0,1]$, the condition

$$0 \;=\; f(x, h(x,\omega,u), u, \omega)$$

gives

$$0 = u + h_1(x,\omega) - h_2(x,u) - \omega - k_o x/\gamma$$

or, equivalently, $\forall x \in [0,1]$,

$$u = \frac{\omega - h_1(x,\omega) + h_{21}(x) + k_o x/\gamma}{1 - h_{22}(x)} \tag{3.7}$$

with $1 - h_{22}(x) = 1 - \dfrac{1}{1 + k_a(1-x)/\gamma} > 0$ provided that x remains at all time away from 1, $h_{21}(x) = \dfrac{k_d x/\gamma}{1 + k_a(1-x)/\gamma} \geq 0$ and $\omega - h_1(x,\omega) = \omega - \dfrac{\omega}{1 + k_r x/\gamma} \geq 0$, knowing that $\gamma > 0$, $k_a > 0$, $k_d > 0$, $k_r > 0$ and $k_o > 0$, which gives $u \geq 0$.

Then, the expression of k_L as a function of x is determined using (3.7) into $\ell(u, y(x,\omega,u), \hat{x}, \omega) = 0$. Eventually, one obtains the condition

$$k_L \;=\; \gamma \frac{u(x)(1 + \alpha h_{22}(x)) - \omega + h_1(x,\omega) + \alpha h_{21}(x) - k_o x^{sp}/\gamma}{x^{sp} - x^c(x)} \tag{3.8}$$

which uniquely defines k_L, with some possible singularities. The expression (3.8) may be not defined for all $x \in [0,1]$, as the denominator may become singular. The condition $x^{sp} - x^c(x) = 0$ is a polynomial function of order 2 ($ax^2 + bx + c = 0$), where

$$\begin{cases} a &=& -k_r^2 x^{sp} k_d - \gamma\omega k_r k_a - \gamma k_d k_r \\ b &=& -k_r x^{sp}\gamma k_d + k_r x^{sp}\gamma\omega k_a - k_r^2 x^{sp}\gamma\omega + \gamma\omega k_r k_a - \gamma^2 k_d - \gamma^2\omega k_r \\ c &=& -k_r x^{sp}\omega\gamma k_a \end{cases} \tag{3.9}$$

and k_a, k_d, k_r are the kinetics rates of model (1.25). Depending on the operating conditions (especially T and ω), the discriminant may be *i*) positive yielding two distinct real roots, denoted x_1^* and x_2^* or *ii*) negative creating imaginary roots which are not physical.

In all cases, stability is studied using the Jacobian of the closed-loop dynamics, obtained through the implicit function theorem applied to the unsaturated algebraic equation of u (Φ) previously defined in (3.6).

In general, the two eigenvalues along the x axis and $\hat{x}$ axis (λ_1 and λ_2, respectively) are defined as follows

$$\begin{cases} \lambda_1 &=& \dfrac{\partial f}{\partial x} - \dfrac{\partial f}{\partial u}\left(\dfrac{\partial \Phi}{\partial u}\right)^{-1}\dfrac{\partial \Phi}{\partial x} \\ \lambda_2 &=& -k_P \end{cases} \tag{3.10}$$

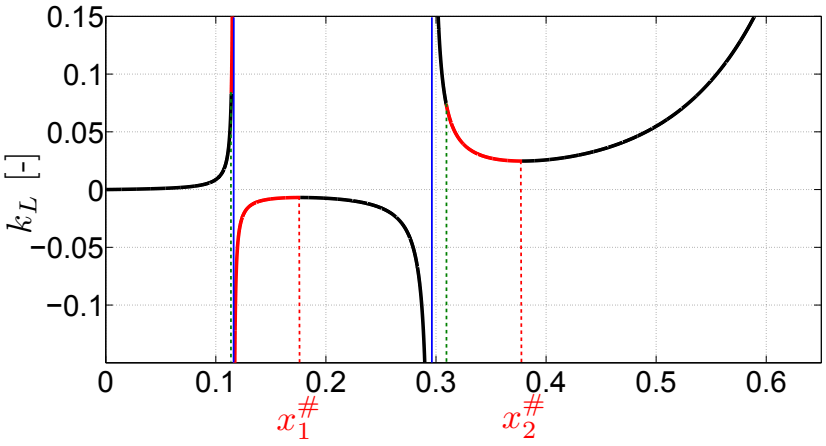

(a) Equilibria of the closed-loop dynamics.

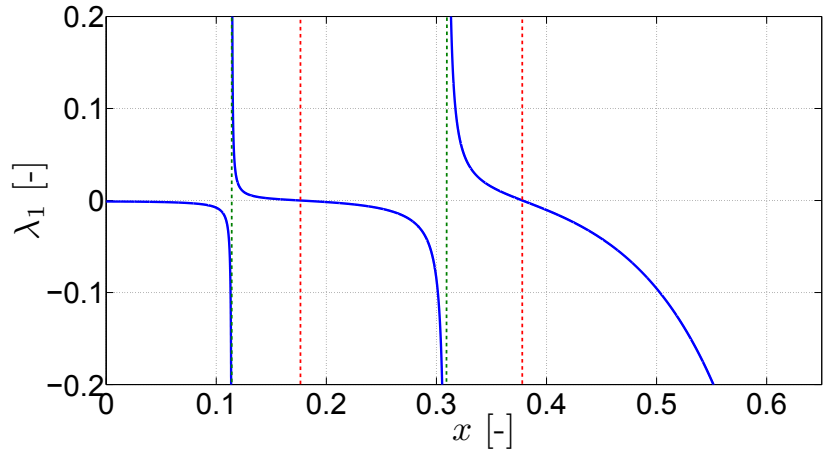

(b) Eigenvalue λ_1.

Figure 3.3: Equilibria of the closed-loop dynamics (3.5) and the eigenvalue λ_1 as functions of k_L. The stable equilibrium points are represented in black and the unstable ones in red. $x_1^\#$ and $x_2^\#$ are the two roots of $\partial k_L/\partial x = 0$.

In Figure 3.3a, for the case of real roots, the equilibria are represented for various k_L (according to (3.8)), $T = 250$ °C, $\omega = 200$ ppm, $v = 4.5$ m.s^{-1} and $x^{\text{sp}} = 0.1$. The stable equilibrium points are depicted in black and the unstable one in red. In Figure 3.3b, the eigenvalue λ_1 is represented as a function of x. For convenience, a zoom on the x axis of Figure 3.3 is reported in Figure 3.4.

The first eigenvalue λ_1 is a discontinuous function. Its sign changes on two separate occasions (see Figure 3.3b and 3.4): about the singularities (values of x such that $\partial\Phi/\partial u = 0$) and when $\partial k_L/\partial x = 0$ (values of x denoted $x_1^\#$ and $x_2^\#$

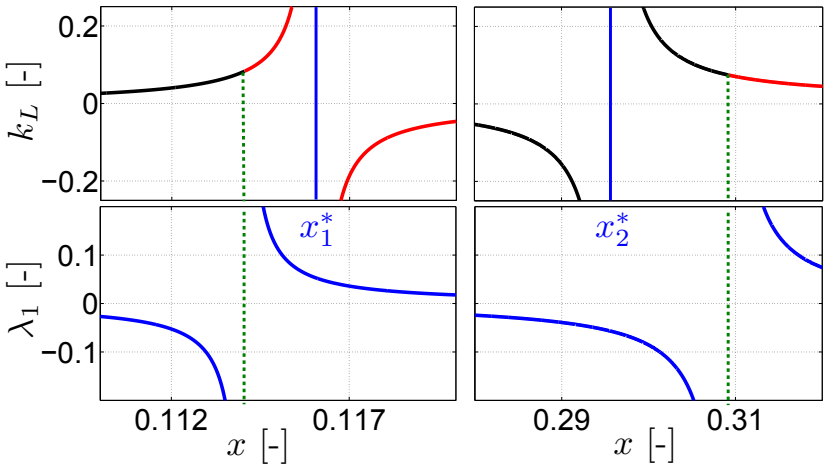

Figure 3.4: [Close-up view of Figure 3.3]. Equilibria of the closed-loop dynamics (3.5) and the eigenvalue λ_1 as functions of k_L. Zoom on x axis, close to the singularities of λ_1.

in Figure 3.3a). Indeed, the condition $\lambda_1 = 0$ is equivalent to $\partial k_L/\partial x = 0$ (see Appendix D.1.2.1 for further details). The second eigenvalue λ_2 is always negative since $k_P > 0$ by construction.

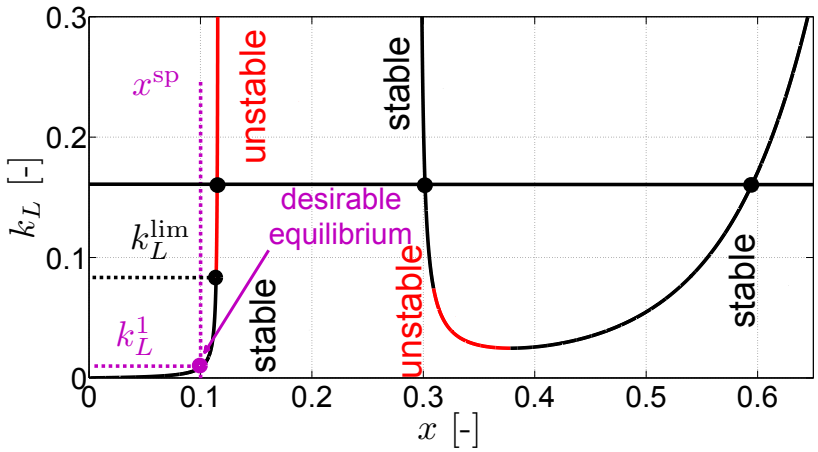

Figure 3.5: Equilibria of the closed-loop dynamics (3.5) as function of k_L ($T = 250$ °C, $\omega = 200$ ppm, $v = 4.5$ m.s^{-1} and $x^{\mathrm{sp}} = 0.1$). The stable equilibrium points are represented in black and the unstable ones in red.

To remove some stable equilibrium points far from the target ($x \in [0.18, 0.3]$

for negative k_L in the figure 3.3a) and to simplify the calibration of the observer gain k_L, we decided to impose $k_L > 0$. This leads to Figure 3.5 which only reports the branches of Figure 3.3a corresponding to positive values of k_L. In the case of (discarded) imaginary roots, the expression (3.8) is continuous with respect to $x \in [0, 1]$. It yields Figures 3.6 and 3.7 which also report the stability/unstability of the equilibrium.

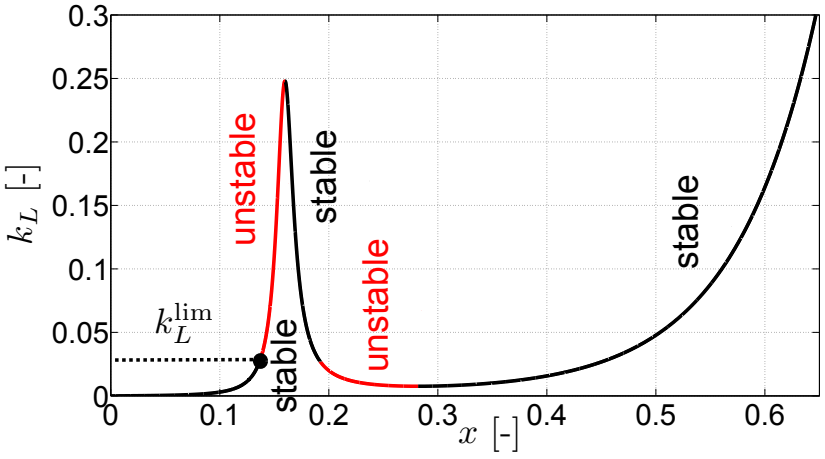

Figure 3.6: Equilibria of the closed-loop dynamics (3.5) as function of k_L ($T = 250$ °C, $\omega = 70$ ppm, $v = 4.5$ m.s^{-1} and $x^{\text{sp}} = 0.1$). The stable equilibrium points are represented in black and the unstable ones in red.

On the domain of interest for the variables ω, x^{sp}, T, v, the system (3.5) may present a bifurcation when the parameter k_L is varied. As shown in Figures 3.5 and 3.6, for a small k_L, there is only one stable equilibrium point close to the setpoint. This is the desired equilibrium. When k_L is increased, two more points appear. The first equilibrium (desired) remains stable, the second one is unstable and the last one, which corresponds to a very high value for the coverage, is also stable. Figures 3.5 and 3.6 report the existence of an upper bound for k_L (denoted $k_L^{\lim}$), from which the desired equilibrium point is no longer stable. Slightly below this critical value, the second equilibrium becomes stable. These critical points do not exist in all cases as depicted in Figure 3.7; in this case (for a small ω), $\forall x \in [0, 1]$, $\dfrac{\partial \Phi}{\partial u} > 0$. The sign of the first eigenvalue λ_1 never changes on the interval $[0, 1]$, it is always negative and the system remains stable. In this case (when ω is small), k_L must be carefully set (close to zero) to prevent the system from converging toward a high coverage ratio (which generates a lot of NH_3-slip).

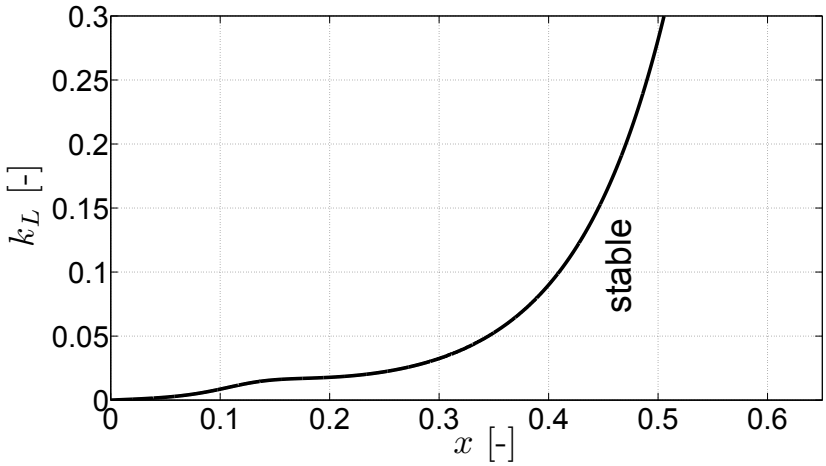

Figure 3.7: Equilibria of the closed-loop dynamics (3.5) as function of k_L ($T = 250$ °C, $\omega = 20$ ppm, $v = 4.5$ m.s^{-1} and $x^{\text{sp}} = 0.1$).

3.4 NO_x measurement interpretation: detection of NH_3-slip

In virtue of the local analysis above, one can conclude that the closed-loop dynamics (3.5) asymptotically reaches one of the stable equilibria. Out of these equilibria, the smallest one is always the desirable one, as already discussed. Fortunately, being in the vicinity of the higher undesirable equilibria (with the largest value) can be easily detected thanks to the downstream NO_x sensor, without any risk of misinterpretation. Indeed, when $x^{\text{c}} < 0$ which represents an impossible coverage ratio value, the measurement of the inlet sensor is lower than the measurement at the outlet $\left(x^{\text{c}} < 0 \Leftrightarrow \frac{\gamma}{k_{\text{r}}}\left(\frac{\omega}{y} - 1\right) < 0 \Leftrightarrow \omega < y\right)$. In the measurement y, see equations (1.29) and (2.5), it is clear that the part h_2 is overwhelming the useful signal h_1 (see Figure 2.6) when y is greater than ω. In this region, with certainty, the sensor measures NH_3. The region of NH_3-slip detection is pictured in Figure 3.8a. It covers some of the stable equilibria that have been created by the closed-loop controller, which are thus "detected". When this detection occurs, the following actions are carried out. First, the observer state $\hat{x}$ is set to the maximum coverage ratio guaranteeing that the NH_3 desorption remains below 10 ppm. This coverage is taken from the *a priori* $x^{\max,\text{stat}}$ map presented in Figure 2.16. This leads to stop the NH_3 injection and to keep it null as long as $\hat{x}$ is greater than x^{sp} to ensure that x has evolved in the vicinity of the desired equilibria and avoid limit cycles phenomena.

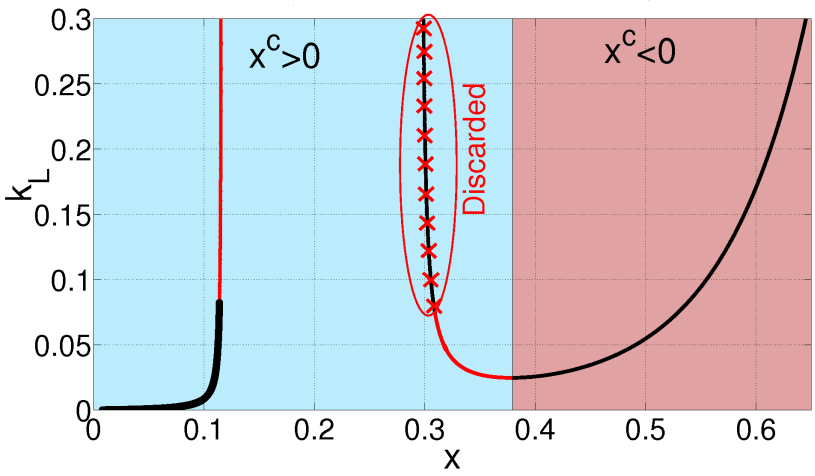

(a) Equilibria of the closed-loop dynamics implemented in discrete time.

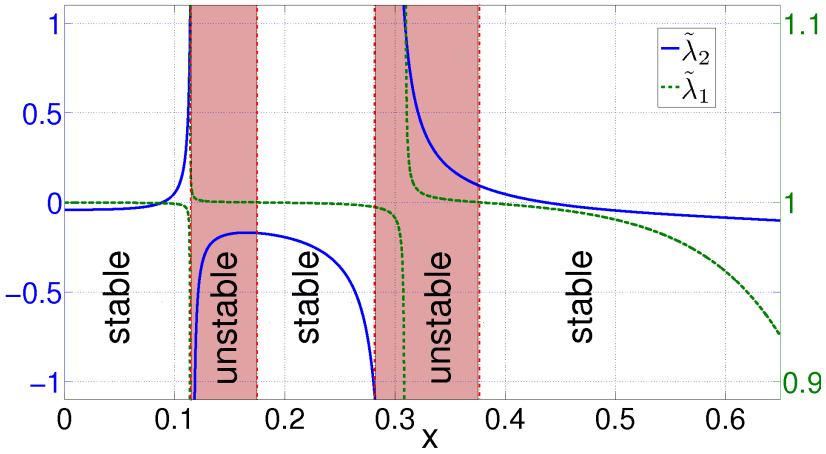

(b) Eigenvalues of the discrete time implementation $\tilde{\lambda}_1$, $\tilde{\lambda}_2$ on x axis and u axis, respectively. Unstable region in red.

Figure 3.8: Equilibria of the closed-loop dynamics (3.5) and eigenvalues of the discrete time implementation as functions of k_L. The region where NH_3-slip is detected ($x^c < 0$) is red in (a) and the one where it is not detected ($x^c > 0$) is blue. The undesirable points, discarded by the implementation in discrete time (3.11) of the closed-loop dynamics, are represented in red in (b).

3.5 Discarding the remaining undesirable stable equilibrium

The proposed feedback controller (3.4) is implicit, due to its defining algebraic equation. One possible explicit implementation in discrete time is as follows (Δ_t being the sampling period):

$$\begin{cases} x_{k+1} &= x_k + \Delta_t f(x_k, h(x_k, \omega_k, u_k), u_k, \omega_k) \\ \hat{x}_{k+1} &= \hat{x}_k + \Delta_t \ell(u_k, y_k(x_k, \omega_k, u_k), \hat{x}_k, \omega_k) \\ u_{k+1} &= \max\Big(0, \omega_k - h_1(x_k, \omega_k) - \alpha h_2(x_k, u_k) \\ & \quad + \frac{1}{\gamma}\left(k_o \hat{x}_{k+1} + k_L\left(\hat{x}_{k+1} - x_k^c\right) - k_P\left(\hat{x}_{k+1} - x_k^{sp}\right)\right)\Big) \end{cases} \tag{3.11}$$

With this implementation, which contains a fixed-point iteration (the relation giving u_{k+1}), the equilibrium points in discrete time always satisfies $\hat{x}_{k+1} = x_k^{sp}$ (refer to Appendix D). Neglecting the observer dynamics, one can now reduce the system (3.11) and consider only the two coupled discrete time dynamics

$$\begin{cases} x_{k+1} &= x_k + \Delta_t \gamma \left(u_k + h_1\left(x_k, \omega_k\right) - h_2\left(x_k, u_k\right) - \omega_k\right) \\ u_{k+1} &= \omega_k - h_1(x_k, \omega_k) - \alpha h_2(x_k, u_k) + \frac{k_o}{\gamma} x_k^{sp} + \frac{k_L}{\gamma}\left(x_k^{sp} - x_k^c\right) \end{cases} \tag{3.12}$$

Its two eigenvalues are $\tilde{\lambda}_1 = 1 + \Delta_t \lambda_1$ and $\tilde{\lambda}_2 = 1 - \dfrac{\partial \Phi}{\partial u}$ (refer to Appendix D.2 for further details). The evolutions of these two eigenvalues as functions of x are depicted in Figure 3.8b. Interestingly, this discrete time dynamics is unstable for every value of the second stable equilibrium. As a result, this troublesome point is discarded by the discrete-time implementation of the proposed closed-loop controller (see Figure 3.8). Indeed, as these critical points always satisfy $\dfrac{\partial \Phi}{\partial u} < -2$, the value of $\tilde{\lambda}_2$ is always less than -1 (they become unstable). Combined with the previous detection method, this implementation leaves only one stable equilibrium remaining: the equilibrium of interest.

3.6 Gain scheduling

Choosing the value for k_L is critical because it defines the value of the reached equilibrium. The most relevant value for this gain would be k_L^1 (see in Figure 3.5) because it corresponds to x^{sp}. Yet the model is relatively uncertain, so we do not target this specific value. Rather, the gain k_L can be simply scheduled to provide an acceptable level of performance. An off-line study reveals that k_L can be taken as a

piecewise affine function of w, which leads to values which are valid for the ranges defined in Section 1.3.5 and induces acceptable bias in the coverage variable x:

$$\begin{cases} k_L = 0 & , \quad \omega < 10 \text{ ppm} \\ k_L = \omega\beta & , \quad 10 < \omega < 100 \text{ ppm} \\ k_L = 100\beta & , \quad \omega > 100 \text{ ppm} \end{cases} \tag{3.13}$$

where β is a calibration parameter inversely proportional to the temperature. It changes from 1 to 1.10^{-2} when T varies from 200 to 400°C. Experimental results using this calibration are reported and discussed in the next chapter.

3.7 Saturations

For practical considerations several saturations are applied to compute the actual AdBlue® mass flow. These prevent malfunctions and ensure the integrity of the actuator.

First, the injection is not permitted (it is arbitrary set to 0) when the temperature at the inlet of the catalyst is lower than 180°C. Below this critical temperature, agglomerates of solid urea and secondary compounds (resulting from incomplete decomposition of urea, refer to § 1.2.1) are formed in the exhaust line and in front of the catalyst (Figure 1.4b). These would be particularly difficult to remove and would decrease the efficiency since they obstruct a part of the catalyst section.

Then, the AdBlue® injector can not remain continuously open. It must be operated by injection pulses. Further, the time between two consecutive pulses must be lower-bounded to avoid injector clogging. These constraints are handled by a conversion of the desired continuous mass flow rate signal into a pulsating signal (having same integral values).

Finally, the NH_3 molar concentration at the inlet of the catalyst has to be saturated to prevent excessive injection (flooding) of urea that could be not completely decomposed (according to (1.1) and (1.2)) into NH_3 before the SCR catalyst or in its first few millimeters.

3.8 Investigations on robustness

In this section, the robustness of the proposed control strategy to modeling errors is assessed in simulation by dispersing the model parameters k_j, $j \in \{\mathrm{a}, \mathrm{d}, \mathrm{f}, \mathrm{s}\}$ and Ω. This robustness analysis is performed on a spatially discretized version of the "reference model" (1.21), with the calibration of the Cu-zeolite catalyst and additional errors on its parameters. Similar results can be obtained for another calibration (for example with the calibration of the Fe-zeolite catalyst). Errors are

added on the pre-exponential factors k_j^0 and on the activation energies E_j, $j \in \{\mathrm{d}, \mathrm{f}, \mathrm{s}\}$, of the reaction rates. These variations consist of additive errors (Δ) of $\pm 20\%$ except for the activation energy of desorption ($\Delta = +20\%$ and -5%).

Table 3.1: NO_x reduction efficiency and NH_3-slip during a NEDC cycle, nominal case and variations with modeling errors.

Parametric variation			NO_x reduction efficiency [%]	NH_3-slip (peak value) [ppm]
Nominal			**81**	**3**
Adsorption	k_a	+20%	81	1
		-20%	81	7
Desorption	k_d^0	+20%	81	5
		-20%	81	2
	E_d	+20%	80	0
		-5%	81	**32**
NH_3 storage capacity	Ω	+20%	80	0
		-20%	81	**21**
NO_x reduction	k_f^0	+20%	82	3
		-20%	80	3
	E_f	+20%	**51**	4
		-20%	72	3
	k_s^0	+20%	83	3
		-20%	78	3
	E_s	+20%	**54**	4
		-20%	81	3

For assessing the robustness, the controller consisting of (3.2), (3.3) and (3.4) is coupled with the disturbed version of the "reference model" and simulations are performed. The NO_x reduction efficiencies and NH_3-slip resulting from modeling errors are reported and compared against the nominal case. All the inputs (set-point and disturbances) of the simulation model are experimental data obtained by performing a NEDC cycle with warm start on a roller test bench.

Table 3.1 reports the results.

It appears that the two parameters that are the most influent on the NH_3-slip are the NH_3 storage capacity Ω and the activation energy of desorption E_d. In particular, an underestimation of the activation energy of desorption E_d greater than 5% may lead to difficulties in maintaining the release of NH_3 into the atmosphere within acceptable levels.

Then, it also appears that the activation energies of NO_x reduction E_f and E_s are influential parameters since an overestimation of 20% of these parameters leads to absolute loss of efficiency of 30% and 26%, respectively. However, with 51% of NO_x reduction efficiency and an inlet SCR amount of NO_x of 164 mg.km^{-1}, the amount of NO_x at the outlet of the catalyst is 80 mg.km^{-1}, which is the Euro 6 standard (80 mg.km^{-1}).

In conclusion, this study suggests that the proposed strategy has a good level of robustness to modeling errors provided that calibration efforts on the desorption process are made. Furthermore, due to the asymmetric impact of the activation energy of desorption (over or under estimation having different impacts), the robustness of the control law has been improved by using a conservative calibration of this parameter (E_d being always overestimated in practice).

Chapter 4

Experimental validation of the proposed strategy

In this chapter, the control strategy proposed in Chapter 3 is implemented on a fully instrumented vehicle, and tested on a roller test bench. First, details of the experimental setup are presented. Then, test results obtained on different cycles are reported.

4.1 Experimental setup

(a) Wind tunnel.

(b) Fully instrumented vehicle.

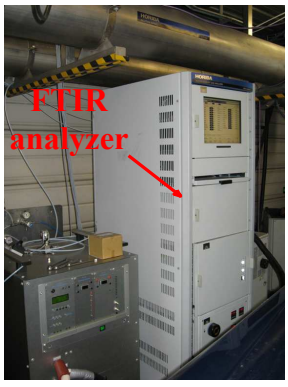

(c) FTIR analyzer.

Figure 4.1: The fully instrumented vehicle mounted on a roller test bench. An FTIR (Fourier Transform InfraRed spectroscopy) analyzer serves for evaluating the performance. The wind tunnel permits to reproduce experimental driving conditions (increase of drag and heat losses with the vehicle speed).

Several pictures of the experimental setup are given in Figure 4.1 and Figure 4.2. The engine and the aftertreatment devices for the experiments are as follows. This engine is a 2.2 liter, four-cylinder, direct-injection diesel engine, equipped with a fixed geometry turbocharger, a high pressure (HP) Exhaust Gas Recirculation (EGR) loop, a Diesel Oxidation Catalyst (DOC), a SCR catalyst and a Diesel Particulate Filter (DPF). This engine is typical of current mid-range vehicles, as detailed in Frobert et al. (2013).

(a) Dilution tunnel to the 5-gas analyzer.

(b) Gas extraction to the analyzers.

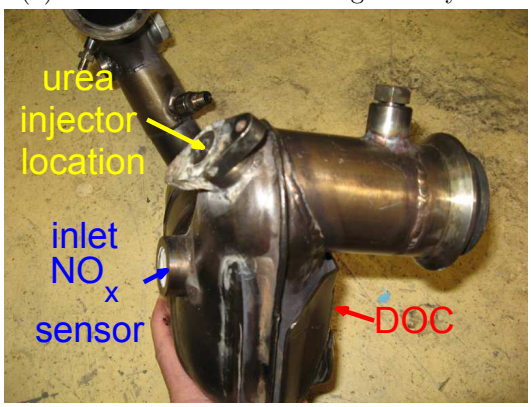

(c) Injector and inlet NO_x sensor location (at the outlet of the DOC).

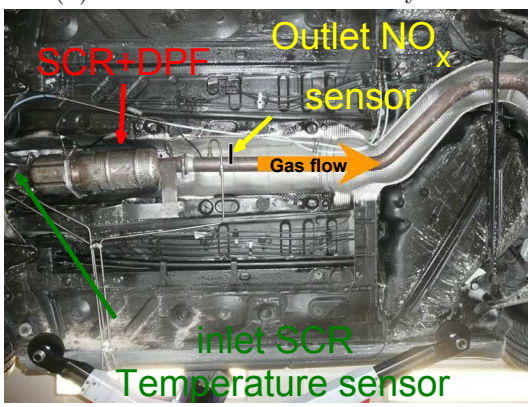

(d) Bottom view of the vehicle.

Figure 4.2: Pictures of the emission measurement system and the aftertreatment devices.

For the emission measurement system, a Horiba™ 5-gas analyzer and a Horiba™ MEXA 6000 FT (FTIR: Fourier Transform InfraRed spectroscopy) gas analyzer (Figure 4.1c and Figure 4.2a) have been used to measure the upstream SCR tailpipe NO_x emissions and the downstream SCR tailpipe NO_x and NH_3 emissions, respec-

tively. These high fidelity analyzers do not have any cross-sensitivity, and can therefore serve as absolute references. Consistently with the definition of the control architecture pictured in Figure 3.1, two VDO/NGK UniNO$_x$ sensors (Laemmerhirt et al. (2010)) located upstream and downstream of the aftertreatment block (SCR + DPF) have been used to provide information to the SCR controller. Their locations are reported in Figure 4.2c and Figure 4.2d. A temperature sensor located at the inlet of the SCR catalyst (Figure 4.2d) and a mass flow sensor located in the intake manifold (used to calculate the exhaust gas velocity) are also connected to the ECU (Engine Control Unit).

The SCR control strategy consisting of (3.2), (3.3), (3.4) and (3.13) developed in Chapter 3 has been implemented on a real time target (xPC Target™) which receives information from the various sensors and communicates with the actuator. This real-time target communicates with the embedded ECU developped by IFPEN (which replaces the serial ECU of the vehicle) using real time Ethernet through the UDP protocol. The real-time target is supervised using a specifically developed HMI (Human Machine Interface). The sensors and actuators are connected to the ECU in various ways:

- The NO$_x$ sensors and the temperature sensors of the exhaust line (including inlet SCR temperature sensor) are connected through the CAN (Controller Area Network) channels;
- Several PWM (Pulse Width Modulation) channels are used for the control of the actuators such as: the turbocharger, the EGR valve, the urea injector;
- Several analog channels are used to receive information from various sensors such as: (manifold, exhaust) pressure, (water, oil, fuel) temperature, (intake manifold) mass flow.

4.2 Experimental results

In this section, the results obtained from the fully instrumented vehicle tested under real driving conditions are reported. These experimental results are obtained with two types of catalysts: Fe-zeolite and Cu-zeolite. The model parameters used in the control algorithm for these two catalysts are reported in Table 4.1. The two types are representative of the technologies found on current and next-generation (2017) of automotive vehicles. The main advantage over other technologies (TiO_2, V_2O_5,...) is that they do not use precious metals, while leading to improved performance and compactness (Johnson (2006)).

Table 4.1: Model parameters for the two types of catalysts (Fe-zeolite and Cu-zeolite).

			Fe-zeolite catalyst	Cu-zeolite catalyst
Adsorption	k_a^0	[kg.m^3.mol^{-2}.s^{-1}]	4.1	5.9
Desorption	k_d^0	[kg.mol^{-1}.s^{-1}]	2.67 10^5	4.1 10^5
	E_d	[kJ.mol^{-1}]	85	88.5
NO_x reduction	k_r^0	[kg.m^3.mol^{-2}.s^{-1}]	7.19 10^5	2 10^9
	E_r	[kJ.mol^{-1}]	55	82.6
NH_3 storage capacity	Ω	[mol.m^{-3}]	70	160
Length	L	[inch]	8	9

4.2.1 Experimental results without gain scheduling

First, to demonstrate the necessity of scheduling the gain k_L, a test is performed with a voluntarily poorly tuned k_L. As it appears in Figure 4.3, where the last 500 seconds of a NEDC cycle are highlighted, this strategy has relatively limited performance.

Figure 4.3a presents the histories of (ω,y) and (x^{sp},$\hat{x}$). At about $t = 330$ s, the difference $\hat{x} - x^c$ increases (due to the cross-sensitivity to NH_3, the apparent efficiency calculated from the NO_x sensors decreases): $\hat{x}$ decreases, and u is increased as depicted in the evolution of the AdBlue® mass flow in Figure 4.3b. This results in significant NH_3-slip, as can be seen from traces of ω and y. At last, when NH_3 is detected with certainty (at about $t = 360$ s), the coverage ratio is corrected, and the injection is turned off ($u = 0$).

This clearly stresses that a proper choice of k_L is important, as well as a good detection of NH_3-slip is.

4.2.2 Experimental results obtained with the proposed gain scheduling methodology

The gain scheduling method proposed in § 3.6 is used and several cycles are performed with the two kinds of catalysts. All these tests have been performed with a catalyst which is initially empty at the start of the cycle.

4.2.2.1 Warm start NEDC cycle with a Fe-zeolite catalyst

First, the results on a NEDC cycle with a warm start and a Fe-zeolite catalyst are presented in Figure 4.5.

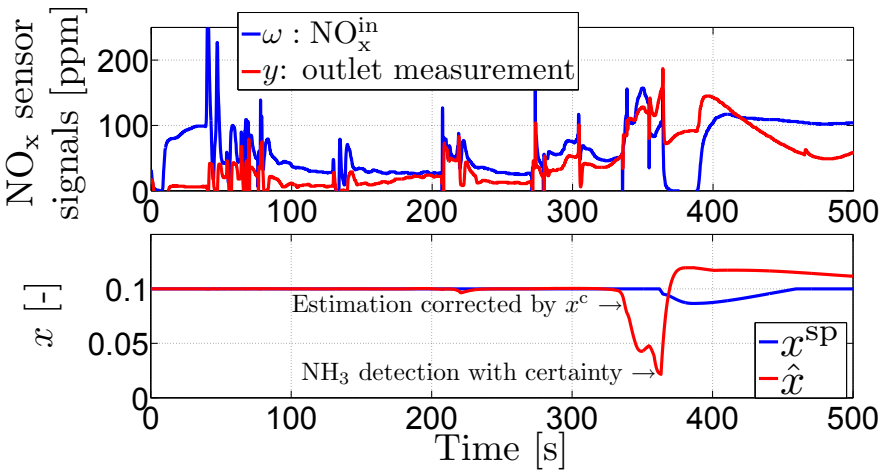

(a) NO_x emissions and coverage ratio evolution.

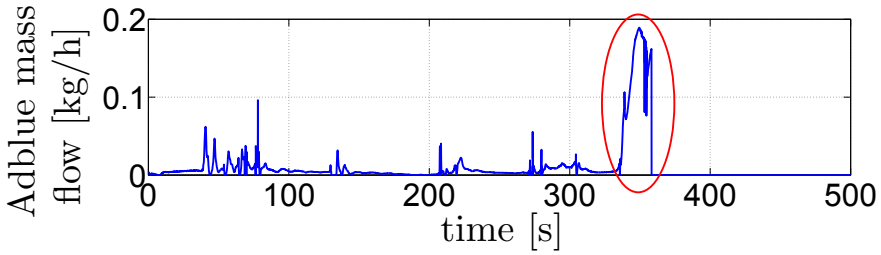

(b) AdBlue® injection.

Figure 4.3: Case of a poorly tuned k_L under transient conditions: evolution of ω, y, x^{sp}, $\hat{x}$ and the AdBlue® injection as functions of time. Poor tuning results in a bad interpretation of sensor information, the system gets caught into a temporary NH_3-slip phase, which is eventually stopped when NH_3 detection is certain. Catalyst: Fe-zeolite. Experimental results.

Changes of the temperature and the gas velocity during the cycle are illustrated in Figure 4.4. Figure 4.5a and Figure 4.5b report the instantaneous and cumulative amounts of NO_x produced by the engine and released to the atmosphere, respectively. In this test, the control strategy performs well, both in terms of NO_x reduction and NH_3-slip limitation. A quantitative summary of performance is given in Table 4.2. The NEDC cycle corresponds to a driving distance of 11 km.

The NO_x input is 2.06 g or 188 mg/km (Euro 4 standard: 250 mg/km; and Euro 5 standard: 180 mg/km). In this NEDC cycle, the obtained NO_x reduction efficiency is about 68% while a very low amount of NH_3 is detected by the FTIR analyzer. In conclusion, one can now remark that one has been able to make an

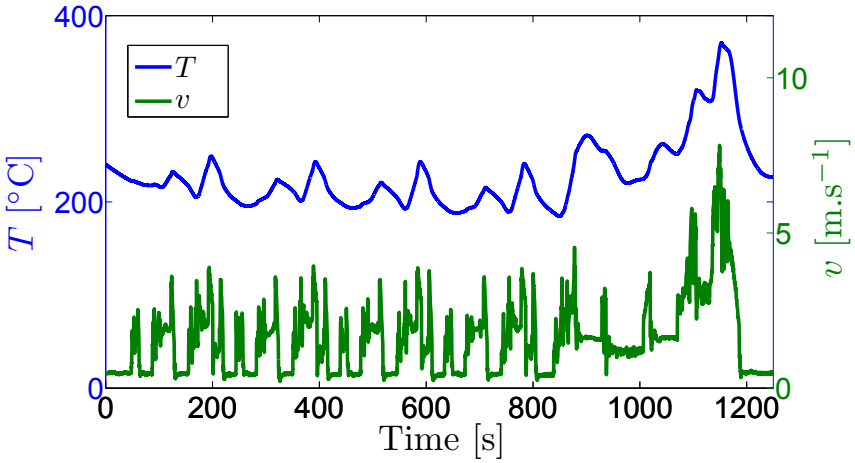

Figure 4.4: Variation of temperature and gas velocity during the warm start NEDC cycle. Experimental results.

Table 4.2: Performance obtained on a warm start NEDC cycle using a Fe-zeolite catalyst (inlet amount of NO_x: 188 mg/km). NH_3 acceptable limits are derived from the regulatory thresholds of the upcoming Euro VI standards concerning heavy duty vehicles. Experimental results.

		Obtained results	Euro 6 standards	NH_3 acceptable limits
NO_x reduction efficiency [%]		**68**	-	-
Cumulative outlet NO_x	over the cycle [g]	0.67	-	-
	per km [mg/km]	61	80	-
Outlet NH_3 molar concentration	average value [ppm]	**3**	-	10
	maximum value [ppm]	**20**	-	30

almost Euro 5 diesel engine satisfy the Euro 6 standards requirement on a warm start NEDC cycle.

These results highlight that the proposed gain scheduling methodology has allowed to improve the performance of the SCR system, both in terms of NO_x reduction and release of NH_3 into the atmosphere. The AdBlue® injection is further reduced (compared to Figure 4.5c) at the end of the NEDC cycle, when the apparent

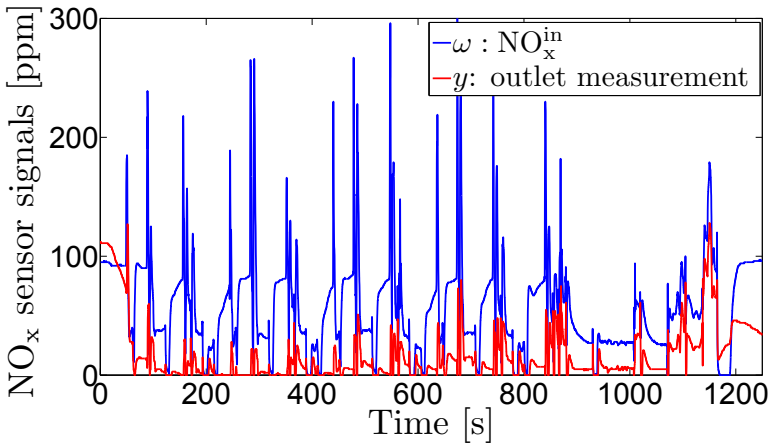

(a) NO_x emissions.

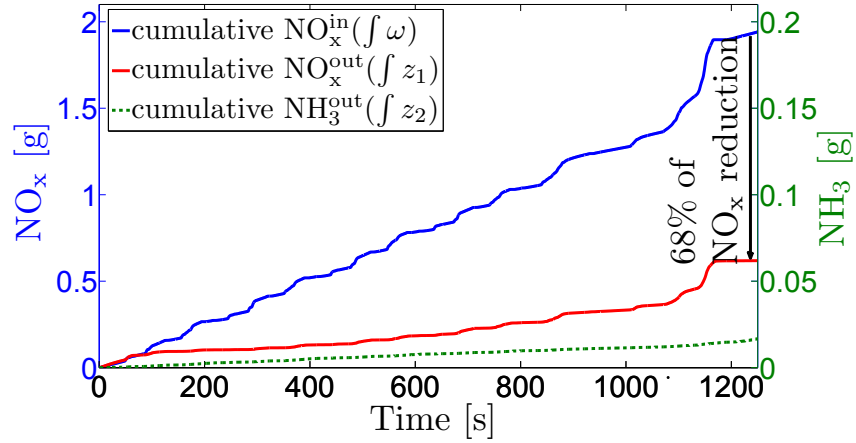

(b) Cumulative NO_x and NH_3 emissions.

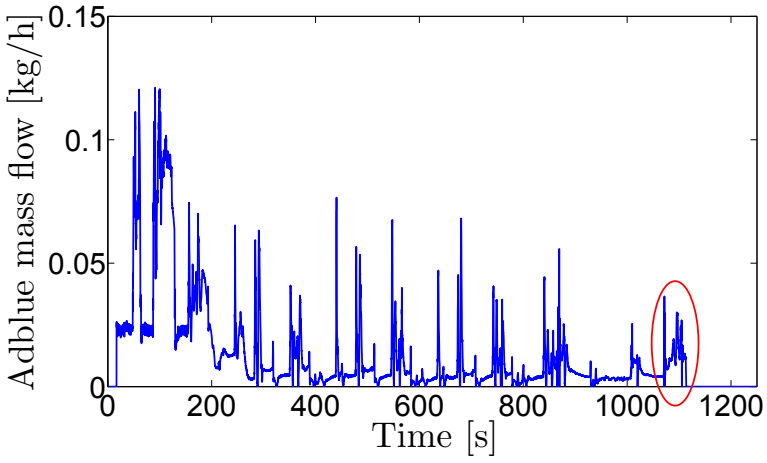

(c) AdBlue® injection.

Figure 4.5: Warm start NEDC cycle using a Fe-zeolite catalyst. Experimental results.

NO_x reduction efficiency (calculated from the two NO_x sensors) decreases due to the non-negligible presence of NH_3 at the outlet of the catalyst. The scheduling of the observer gain (in addition to a proper choice of the setpoint) is able to drastically reduce the NH_3-slip, that remains below the fixed limits.

4.2.2.2 Warm start NEDC cycle with a Cu-zeolite catalyst

Here, the results on a NEDC cycle with a warm start and a Cu-zeolite catalyst are presented in Figure 4.6.

The curves depicted in Figure 4.6a and Figure 4.6b can be directly compared to those in Figure 4.5a and Figure 4.5b, respectively. The performance of the control strategy is quite good too. A NO_x reduction efficiency of 81% is obtained with a very low level of NH_3-slip over the cycle. This performance is reported in Table 4.3.

Table 4.3: Performance obtained on a warm start NEDC cycle using a Cu-zeolite catalyst (inlet amount of NO_x: 164 mg/km). Experimental results.

		Obtained results	Euro 6 standards	NH_3 acceptable limits
NO_x reduction efficiency [%]		**81**	-	-
Cumulative outlet NO_x	over the cycle [g]	0.33	-	-
	per km [mg/km]	30	80	-
Outlet NH_3 molar concentration	average value [ppm]	**2**	-	10
	maximum value [ppm]	**15**	-	30

The NO_x input is 1.8 g (or 164 mg/km). In this test, the amount of input NO_x varies from the previous NEDC cycle due to a different setpoint of the engine Burned Gas Ratio (BGR). This change shifts the trade-off between NO_x and particles (PM) to a lower level of NO_x (and thus more PM). Again, the result is that the Euro 6 standards requirement is now achieved on a warm start NEDC cycle by an Euro 5 diesel engine. These good results also show that the proposed strategy is relatively versatile and can be easily adapted to various types of catalysts.

4.2.2.3 The controller behavior on a transient cycle

Finally, another cycle, a highly varying one beginning with a warm start is performed (using a Cu-zeolite catalyst). The obtained results are reported in Figure 4.7. The performance is also highly satisfactory, both in terms of NO_x reduction (76%

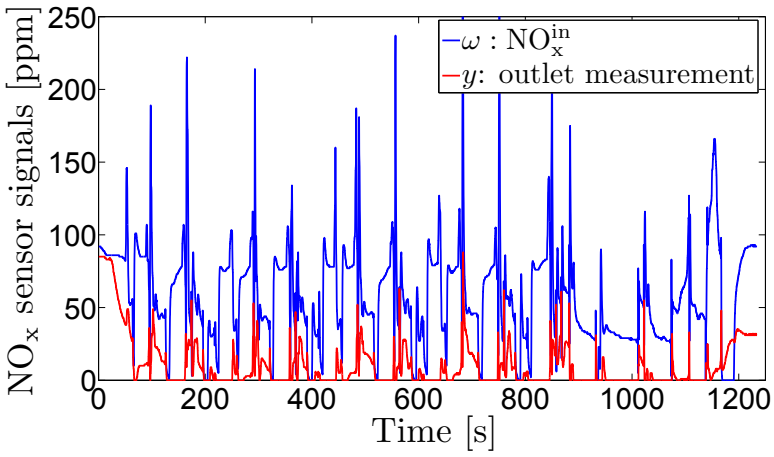

(a) NO_x emissions.

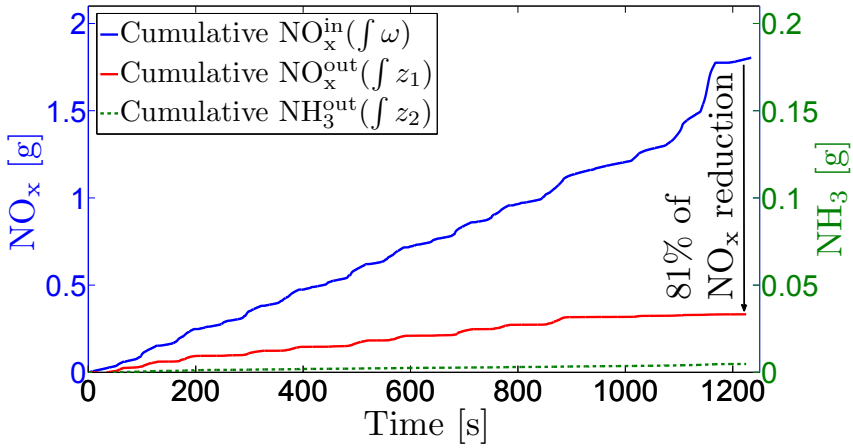

(b) Cumulative NO_x and NH_3 emissions.

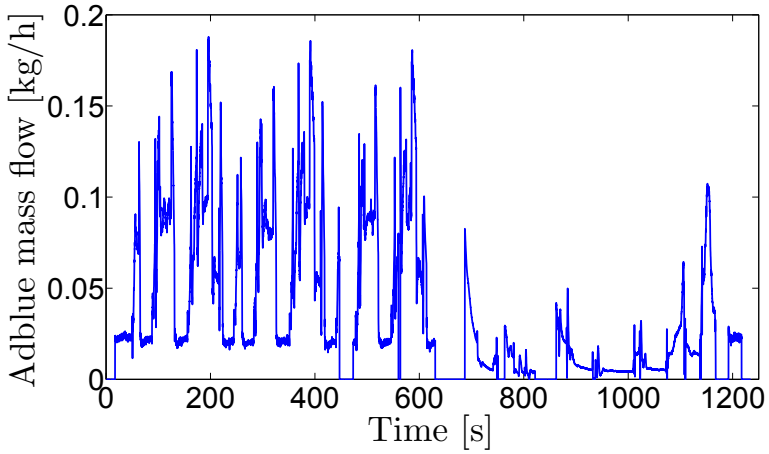

(c) AdBlue® injection.

Figure 4.6: Warm start NEDC cycle using a Cu-zeolite catalyst. Experimental results.

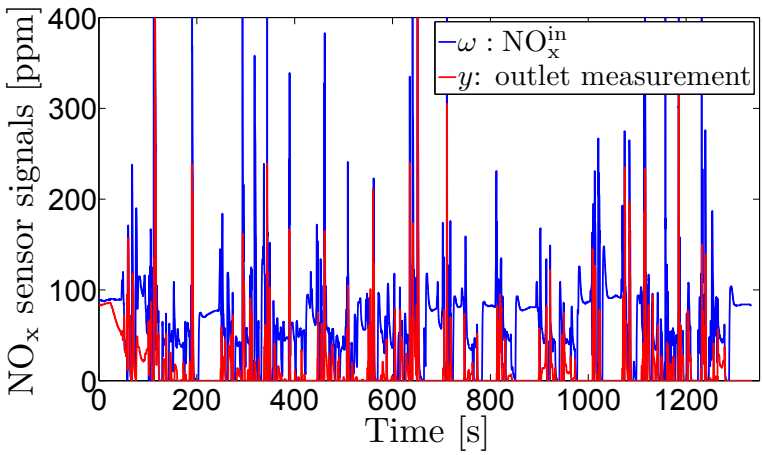

(a) NO_x emissions.

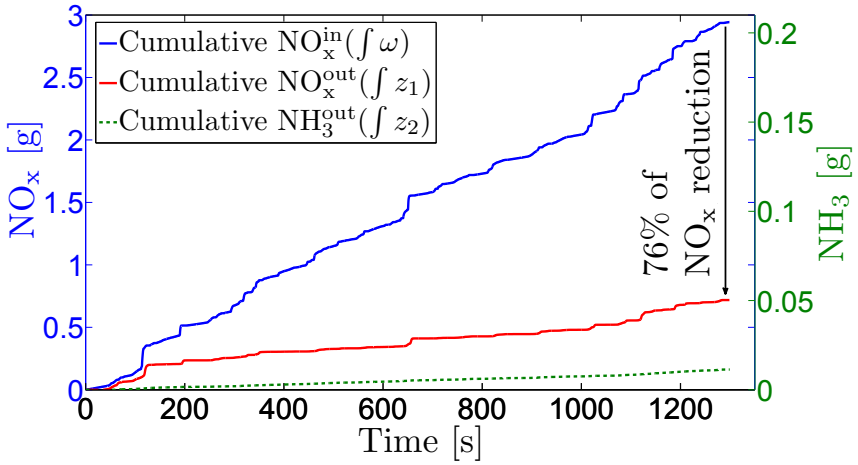

(b) Cumulative NO_x and NH_3 emissions.

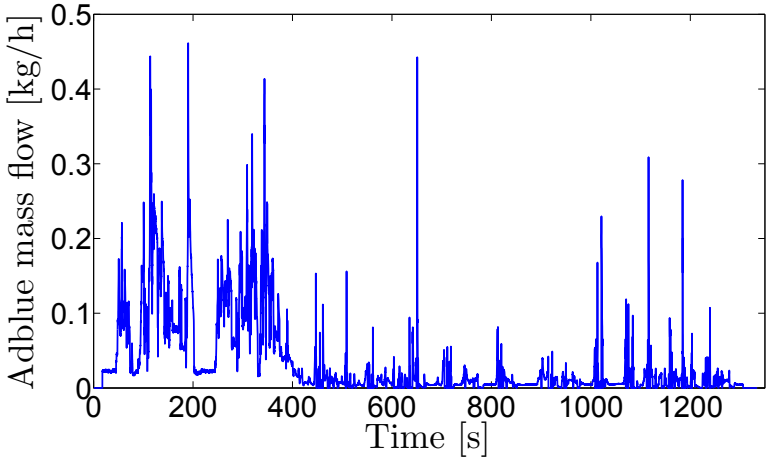

(c) AdBlue® injection.

Figure 4.7: Warm start cycle using a Cu-zeolite catalyst. Experimental results.

efficiency) and NH_3 slip limitations (average molar concentration about 3 ppm and peak value less than 10 ppm). This performance is reported in Table 4.4.

Table 4.4: Performance obtained on the highly varying cycle using a Cu-zeolite catalyst (inlet amount of NO_x: 2.95g). Experimental results.

		Obtained results
NO_x reduction efficiency [%]		**76**
Cumulative outlet NO_x over the cycle [g]		0.72
Outlet NH_3 molar concentration	average value [ppm]	**2**
	maximum value [ppm]	**12**

4.3 Concluding remarks

The experimental results presented in this chapter show that the proposed control strategy allows to reach the Euro 6 emission standards while keeping the NH_3-slip below an acceptable threshold. The comparison between Figure 4.3 and Figure 4.5 points out the improvement provided by the gain scheduling methodology. In practice, for all the Euro standards, a cold NEDC cycle ("cold engine" start of the vehicle) must be carried out. In this process, the inlet temperature of the catalyst is initially less than 180°C at the beginning of the cycle (which lasts approximately 400 s) and no injection is permitted. During this lapse of time, the NO_x treatment capacity is decreased due to the impossibility to reach the setpoint x^{sp}. Interestingly, one can compensate the impossibility to inject urea by preconditioning the SCR catalyst. The European standards allow one to start the normalized cycle with a non empty catalyst. This procedure yields a partial NO_x reduction when no injection is permitted while the temperature is sufficient for the reduction reactions to take place. During this thesis, this kind of cycles has not been realized. The main reason is that performing a NEDC cycle with cold start means running only one test per day. Given the cost of experiments at roller test bench, proceeding that way would have prevented us from obtaining the experimental results presented here. The second reason is that we have not yet established nor implemented the preconditioning strategy.

However, we bet one could achieve the objectives of the Euro 6 standards with cold start considering the obtained margins in terms of NO_x reduction efficiency on the warm start tests. In the future, further experiments should be considered to check the validity of this point of view.

Chapter 5

Extensions

The cross-sensitivity of NO_x sensors to NH_3 is an example of a wider class of control problems where measurements are ambiguous. In the preceding chapters, we have proposed a solution tailored to the particular example. In this chapter, we wish to provide an alternative view of this problem.

This chapter contains developments directly presented in section 5.1 inspired by the works of Praly (1992) and Coron (1994) where one considers the output-feedback stabilization of

$$\dot{x} = u, \quad y = x^2 \tag{5.1}$$

In Coron (1994), it is shown that it is impossible to asymptotically stabilize (5.1) by a *continuous stationary dynamic output feedback law*. In particular, a classic linear time-invariant observer-controller will not work. Viable solutions can be sought after among several options: discontinuous feedback, or instationnary feedback, or an adaptive technique which introduces extra states that are not asked to converge to zero. This is the path that is explored in Praly (1992), where it is shown that one can construct a particular dynamic feedback of Nussbaum type (see the original work of Nussbaum (1983)) the synthesis of which is instrumental in the derivation of the state observer constructed below in section 5.1. The Nussbaum gain (see e.g. Narendra & Annaswamy (2005) [§9.2 pp 360–363] for a tutorial presentation) is a function which changes its sign and gets an unbounded absolute magnitude as its argument (which is an extra state) increases to ∞. It can be used to globally asymptotically stabilize a scalar plant with unknown damping and input gain with unknown sign. Below we will extend this stabilization technique to construct an observer.

Following this approach, we will test in simulation an observer of this type for the problem under consideration.

$$\left\{ \begin{array}{rcl} \dot{x} & = & \gamma \left(u + h_1(x, \omega) - h_2(x, u) - \omega \right) - k_o x \\ y & = & h_1(x, \omega) + \alpha h_2(x, u) \end{array} \right. \tag{5.2}$$

derived from (1.30) and considering the measurement of a cross-sensitive NO_x sensor (2.5).

5.1 Adaptive observer

5.1.1 Preliminary theory

We consider the problem of designing an observer for the single-dimensional system

$$\dot{x} = u, \qquad y = g(x) \tag{5.3}$$

where u is a bounded signal such that x remains bounded for all times, and g is a surjective unimodal differentiable function $\mathbb{R} \to \mathbb{R}^+$, i.e. there exists $\bar{x}$ such that $\forall y \geq 0$, there exists a unique vector $(x_1 \leq \bar{x}, x_2 \geq \bar{x})$ such that $g(x_1) = g(x_2) = y$.

Proposition 1. Consider k a differentiable function such that $\sup_{z\geq 0} k(z) = +\infty$, $\inf_{z\geq 0} k(z) = -\infty$, with k' the derivative function of k, bounded on every compact of $\mathbb{R}^+$, and h a bounded continuous function with $h(0) = 0,\ h(x \neq 0) > 0$.

The following observer

$$\begin{cases} \dot{\hat{x}} = u + k'(z)h(y - g(\hat{x})) \\ \dot{z} = h(y - g(\hat{x})) \end{cases} \tag{5.4}$$

gives an asymptotic reconstruction of x as

$$\lim_{t\to\infty} \hat{x}(t) - x(t) = 0$$

for every initial conditions $x(0)$, $\hat{x}(0)$ providing that the following two assumptions hold

1. *persistent excitation*

$$\begin{aligned} &\forall 0 < M \leq 1, \forall T > 0, \exists t_1 > T \text{ such that:} \\ &\{\forall t \in [t_1, t_1 + 1], u(t) > M\} \text{ or } \{\forall t \in [t_1, t_1 + 1], u(t) < -M\} \end{aligned} \tag{5.5}$$

2. *the state x remains strictly on one side of $\bar{x}$ for all times.* This assumption bears on u. It can be formulated as: for some $\epsilon' > 0$,

$$\{\forall t \geq 0, x(t) \leq \bar{x} - \epsilon'\} \text{ or } \{\forall t \geq 0, x(t) \geq \bar{x} + \epsilon'\} \tag{5.6}$$

Proof. A simple integration of the equation $\dot{\hat{x}} - \dot{x} = k'(z)\dot{z}$ gives

$$\hat{x}(t) - x(t) = \hat{x}(0) - x(0) + k(z(t)) - k(z(0)) \tag{5.7}$$

On the other hand, one has that $t \mapsto z(t)$ is increasing because $\dot{z} \geq 0$. So, either z grows unbounded or it has a limit

$$\lim_{t\to\infty} z(t) = \ell < \infty$$

- Assume that

  $$\lim_{t\to\infty} z(t) = \ell < \infty$$

  Then, one directly gets

  $$\int_0^\infty h(g(x(t)) - g(\hat{x}(t)))dt = \ell \tag{5.8}$$

  In this equation, $t \mapsto h(g(x(t)) - g(\hat{x}(t)))$ is uniformly continuous. To establish this, consider that x and $\dot{x}$ are bounded and g is uniformly continuous. Then $h(g(x(t)))$ is uniformly continuous. Also, in (5.7), all the terms are bounded, so $\hat{x}(t)$ is bounded for all t. Then, in (5.4), one has $\dot{\hat{x}} = u + k'(z)h(g(x) - g(\hat{x}))$. In this expression, u is bounded by assumption, $k'(z)$ is bounded because z is upper-bounded by ℓ, and k' is bounded on every compact set. This shows that $\dot{\hat{x}}$ is bounded so $\hat{x}$ is uniformly continuous. Then, the desired result directly follows.

  One can then apply Barbalat's lemma to (5.8) to obtain that the integrand goes to 0 as $t \to +\infty$, and then that

  $$\lim_{t\to+\infty} g(x(t)) - g(\hat{x}(t)) = 0 \tag{5.9}$$

  We are now going to use the persistency of excitation assumption (5.5) to conclude. Consider the differential equation

  $$\frac{d}{dt}\left(g(x(t)) - g(\hat{x}(t))\right) = g'(x)u - g'(\hat{x})\left(u + k'(z)h(g(x) - g(\hat{x}))\right)$$

  Take $M = 1$, from (5.5), $\forall T > 0$, $\exists t_1 > T$ such that, without loss of generality $u(t) > 1$ on $[t_1, t_1 + 1]$. Then, $\forall \varepsilon \in [0, 1]$,

  $$\begin{aligned} g(x(t_1 + \varepsilon)) - g(\hat{x}(t_1 + \varepsilon)) - g(x(t_1)) + g(\hat{x}(t_1)) = \\ \int_{t_1}^{t_1+\varepsilon} \left(g'(x(t)) - g'(\hat{x}(t))\right) u(t)dt \\ - \int_{t_1}^{t_1+\varepsilon} g'(\hat{x}(t))k'(z(t))h(g(x(t)) - g(\hat{x}(t)))dt \end{aligned}$$

Yet, one has

$$\lim_{T\to\infty} g(x(t_1+\varepsilon)) - g(\hat{x}(t_1+\varepsilon)) - g(x(t_1)) + g(\hat{x}(t_1)) = 0$$

from (5.9). Also, $z(t)$ being bounded by ℓ, one has that $k'(z(t))$ is bounded, independently of T. Then, because of (5.9), one has that, $\forall \varepsilon \in [0,1]$

$$\lim_{T\to\infty} \int_{t_1}^{t_1+\varepsilon} g'(\hat{x}(t))k'(z(t))h(g(x(t)) - g(\hat{x}(t)))dt = 0$$

so, we deduce

$$\lim_{T\to\infty} \int_{t_1}^{t_1+\varepsilon} \left(g'(x(t)) - g'(\hat{x}(t))\right) u(t)dt \triangleq I(t_1, t_1+\varepsilon) = 0$$

By assumption, on the interval $[t_1, t_1+1]$, $u(t) > M = 1$. For ε sufficiently small, $I(t_1, t_1+\varepsilon) \geq \varepsilon(g'(x(t_1)) - g'(\hat{x}(t_1))) + \circ(\varepsilon)$. Then,

$$\lim_{T\to\infty} g'(\hat{x}(t_1)) - g'(x(t_1)) = 0 \tag{5.10}$$

From (5.9), we know that $\forall \varepsilon > 0$, $\exists T$ such that,

$$\forall t \geq T, \{|x(t) - \hat{x}(t)| \leq \varepsilon \text{ or } |x_B(t) - \hat{x}(t)| \leq \varepsilon\}$$

where x_B is (uniquely) defined by $g(x_B) = g(x)$, $x_B \neq x$ for $x \neq \bar{x}$ ($x_B = x$ if $x = \bar{x}$, respectively). Yet, under assumption (5.6), $x_B \neq x$. Then, because $t \mapsto \hat{x}(t)$ is continuous, for ε sufficiently small, $\exists T \geq 0$ such that one of the two propositions holds: *i)*$\{\forall t \geq T, |x(t) - \hat{x}(t)| \leq \varepsilon\}$ or *ii)* $\{\forall t \geq T, |x_B(t) - \hat{x}(t)| \leq \varepsilon\}$.

Assume that *ii)* holds, then

$$\lim_{t\to\infty} g'(x_B(t)) - g'(\hat{x}(t)) = 0$$

Now to show the contradiction, consider an increasing sequence $(T_i)_{i\in\mathbb{N}}$, with

$$\lim_{i\to\infty} T_i = +\infty$$

From (5.5), one can construct an increasing unbounded sequence $(t_i)_{i\in\mathbb{N}}$ such that

$$\lim_{i\to\infty} g'(\hat{x}(t_i)) - g'(x(t_i)) = 0$$

while we have that

$$\lim_{t\to\infty} g'(x_B(t_i)) - g'(\hat{x}(t_i))$$

This contradicts (5.6) (which also induces $g'(x(t))g'(x_B(t)) < 0$).

This contradiction shows that *i)* holds. Therefore

$$\lim_{t\to\infty} x(t) - \hat{x}(t) = 0$$

- In the case where
$$\lim_{t\to\infty} z(t) = +\infty$$
we deduce from (5.7) that there exists $t_1 > 0$ such that
$$\hat{x}(t_1) = x(t_1)$$
This shows that the convergence occurs in finite time.

□

Interestingly, one can interpret conditions (1) and (2) as necessary conditions for observability. At first order $\delta\dot{x} = \delta u$, $\delta y = \frac{\partial g}{\partial x}(x)\delta x$ is a linear time-varying system in state space for $\dot{X} = AX + Bu$, $y = CX$ with $A = 0$, $B = 1$ and $C = \frac{\partial g}{\partial x}(x)$. The time-varying observability condition rank $\begin{pmatrix} C \\ \dot{C} \end{pmatrix} = 2$ is satisfied when $\frac{\partial g}{\partial x}(x) \neq 0$ and $u \neq 0$ which is satisfied on intervals when (5.5) and (5.6) hold.

5.1.2 Application examples

5.1.2.1 First example

First, a simple toy example is presented[1], the observer (5.4) for system (5.3) is considered with $g(x) = |x|\exp(-1/x^2)$, $k(x) = x\sin\left(\frac{\pi}{2}x\right)$, $h(x) = \tanh(x^2)$, $u(t) = \sin(t)$ and $x(0) = 1$.

Results are reported in Figure 5.1 which gives the evolution of the state x and its estimate $\hat{x}$ for various initial conditions ($\hat{x}(0) \in [-3, 3]$). Interestingly, we obtain a potentially long convergence, depending on the ambiguity of the situation (depending on the initial condition). We also depict the gain $k'(z(t))$ over time. Its asymptotic value can take any of the possible signs, depending on the initial condition.

[1]Another interesting problem one could consider is the generalization of (5.3) in a distributed parameter context. For example, consider
$$\begin{cases} \dfrac{\partial v}{\partial t} + \dfrac{\partial v}{\partial x} = -h(v) & , x \in [0,1] \\ v(0,t) = u(t) \\ y = g(v(1,t)) \end{cases}$$
where h is a smooth function (can be bijective, increasing) and g is an unimodal function of the type discussed in this chapter. The question of state estimation from the ambiguous output measurement could be studied in the future.

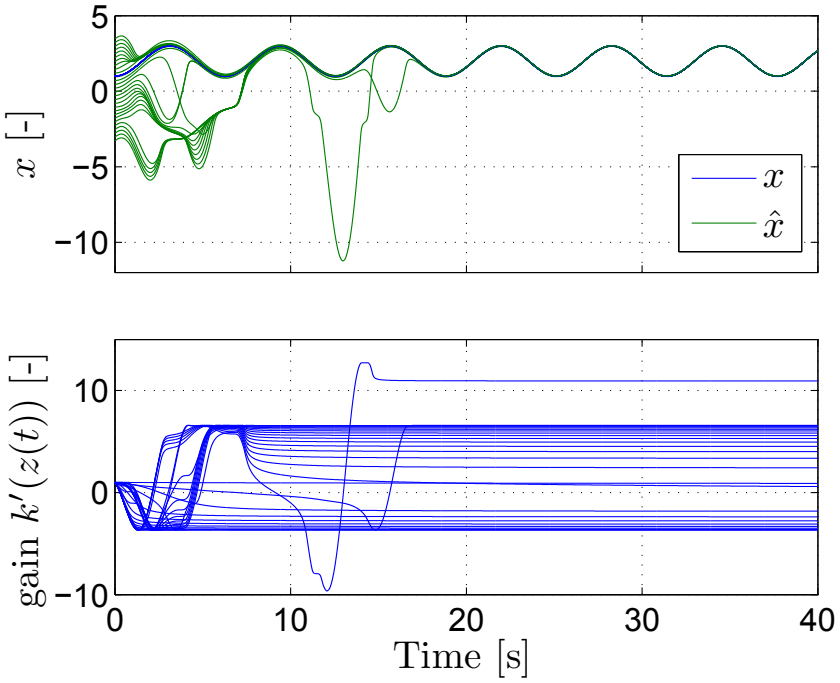

Figure 5.1: Convergence of the observation (5.4) of system (5.3) for various initial conditions. Simulation results.

5.1.2.2 Adaptation to the estimation of the NH_3 coverage ratio

Following the philosophy developed in the previous section, we consider the NH_3 coverage ratio x reconstruction problem. For this purpose, we use a copy of the dynamics and construct a tracking term with a Nussbaum gain of the form given in Proposition 1.

We now consider the observer

$$\begin{cases} \dot{\hat{x}} = \gamma\left(u + h_1(\hat{x},\omega) - h_2(\hat{x},u) - \omega\right) - k_o\hat{x} + k'(z)h(y - g(\hat{x})) \\ \dot{z} = h(y - g(\hat{x})) \end{cases} \tag{5.11}$$

where $g(x) = h_1(x,\omega) + \alpha h_2(x,u)$ and with $k(x) = x\cos\left(\frac{\pi}{2}x\right)$, $h(x) = |x|$, $u(t) = \frac{\omega}{2}(2 + \sin(2\pi f t))$, $f = 3.210^{-3}$. The true system

$$\dot{x} = \gamma\left(u + h_1(x,\omega) - h_2(x,u) - \omega\right) - k_o x$$

is initialized with $x(0) = 0.3$.

Results are reported in Figure 5.2 which gives the evolution of the state x and its estimate $\hat{x}$ for various initial conditions ($\hat{x}(0) \in [0, 0.6]$).

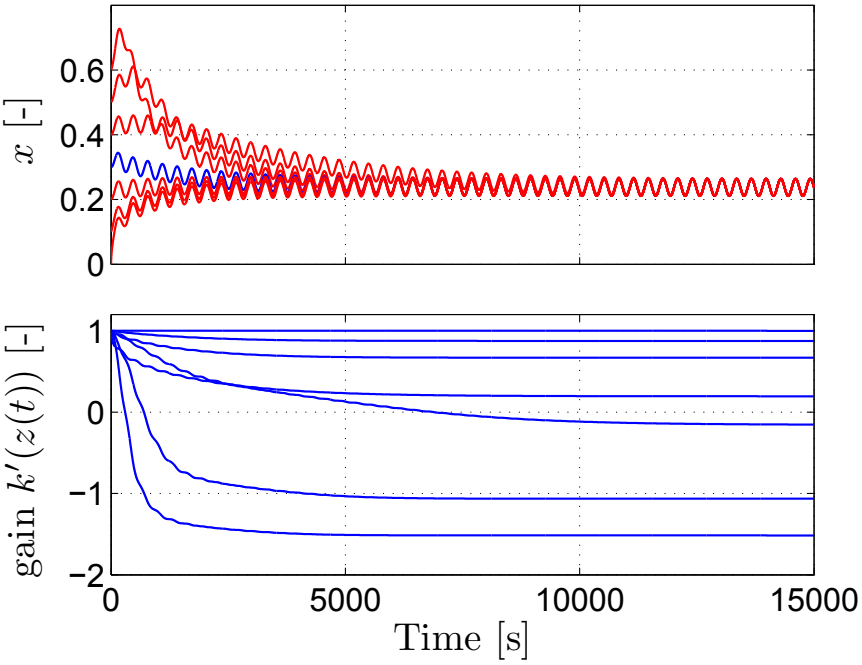

Figure 5.2: Convergence of the observation (5.11) of system (5.2) for various initial conditions. Operating conditions: $T = 250$ °C, $\omega = 300$ ppm, $v = 4.5$ m.s^{-1}. Simulation results.

It is instructive to look at the variations of the Nussbaum gain of the observer for various initial conditions ($\hat{x}(0) \in [0, 0.6]$). It changes its sign depending on the situation. Again, we obtain a potentially long convergence depending on the initialization of the observer. The asymptotic value of the adaptive gain (and the sign) $k'(z)$ which is necessary to reach the reconstruction of x depends on the initial condition.

5.2 Discontinuous observer

In § 5.1, we have seen that the sign of the gain needed to obtain the asymptotic convergence of the estimate from ambiguous measurement is not easy to guess. Rather than employing the adaptive Nussbaum gain, which, intuitively, changes sign as long as convergence is not achieved, we propose another approach. We consider two observers with opposite constant gains. A switching policy is used based on a criterion of absolute error of the prediction. In our setup, y is a non bijective function with respect to x, when x is small, y decreases and then increases when x becomes larger. When the observer is initialized in the decreasing part instead

of the increasing part, it may diverge if the gain is not changed appropriately. In this perspective, one builds two observers having the same structure. The first one employs a positive gain and the second one a negative gain. To compute the estimate $\hat{x}$, only the converging estimate is selected. The same philosophy will be used to extended Kalman filters.

5.2.1 Two state observers with constant gain

The expressions of the observers are given in (5.12) and (5.13), respectively

$$\begin{cases} \dot{\hat{x}}^+ &= \gamma\left(u + h_1(\hat{x}^+, \omega) - h_2(\hat{x}^+, u) - \omega\right) - k_o\hat{x}^+ + K(y - \hat{y}^+) \\ \hat{y}^+ &= h_1(\hat{x}^+, \omega) + \alpha h_2(\hat{x}^+, u) \end{cases} \tag{5.12}$$

$$\begin{cases} \dot{\hat{x}}^- &= \gamma\left(u + h_1(\hat{x}^-, \omega) - h_2(\hat{x}^-, u) - \omega\right) - k_o\hat{x}^- - K(y - \hat{y}^-) \\ \hat{y}^- &= h_1(\hat{x}^-, \omega) + \alpha h_2(\hat{x}^-, u) \end{cases} \tag{5.13}$$

where $K > 0$ is a constant parameter (high gain). We also compute the open loop dynamics to compare it to the developed observers:

$$\dot{\hat{x}}_{OL} = \gamma\left(u + h_1(\hat{x}_{OL}, \omega) - h_2(\hat{x}_{OL}, u) - \omega\right) - k_o\hat{x}_{OL} \tag{5.14}$$

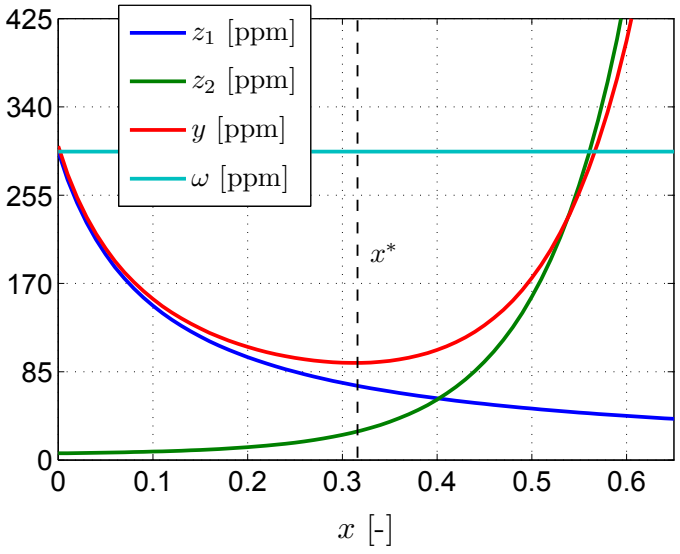

Figure 5.3: Representation of ω, z_1, z_2 and y as functions of x in steady state conditions ($T = 250$ °C, $\omega = 300$ ppm, $v = 4.5$ m.s^{-1}). Simulation results.

For convenience, Figure 5.3 reports the evolution of z_1, z_2 and y as functions of the coverage ratio x, in steady state conditions with a constant input u. y is

a convex function and its derivative is negative before $x^* = 0.32$ characterized by $\frac{\partial y}{\partial x} = 0$ and positive after.

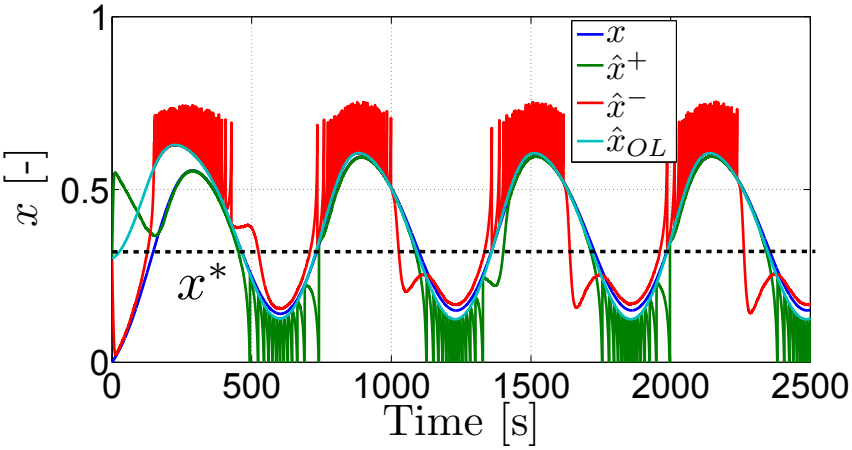

Figure 5.4: Representation of x, $\hat{x}^+$, $\hat{x}^-$ and $\hat{x}_{OL}$ as functions of time for the two state observers with constant gains in steady state conditions ($T = 250$ °C, $\omega = 300$ ppm, $v = 4.5$ m.s^{-1}). Simulation results.

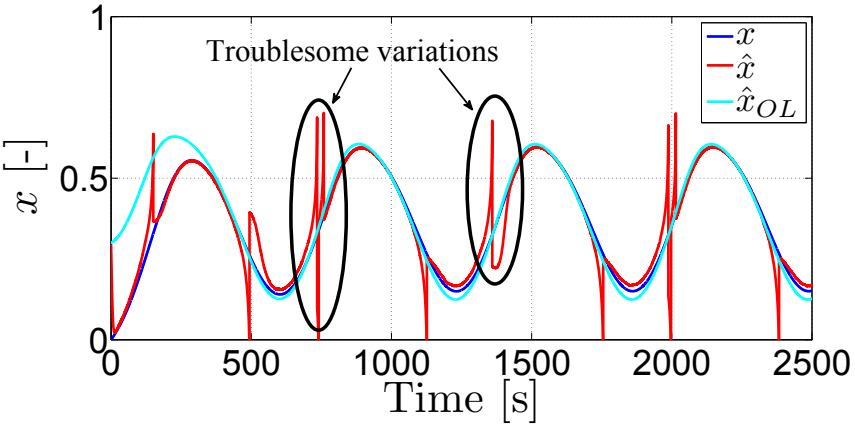

Figure 5.5: Representation of x, $\hat{x}$ and $\hat{x}_{OL}$ as functions of time for the state observers with constant gains in steady state conditions ($T = 250$ °C, $\omega = 300$ ppm, $v = 4.5$ m.s^{-1}). Simulation results.

The two state observers are tested in simulation (steady state conditions: $T = 250$ °C, $\omega = 300$ ppm, $v = 4.5$ m.s^{-1}) with a sinusoidal input $u(t) = 17.10^{-3} * \left(0.5 + \sin\left(\frac{2\pi}{600}t\right)\right)$. The results are depicted in Figures 5.4 and 5.5. Below this

critical value x^*, the positive observer $\hat{x}^+$ diverges while the negative one $\hat{x}^-$ converges (see Figure 5.4). The symmetrical phenomenon occurs when $\hat{x} > x^*$ ($\hat{x}^+$ converges and $\hat{x}^-$ diverges).

This behavior is consistent with the study at first order. First, $\hat{x}^+$ described by (5.12) is considered. The computation of its Jacobian yields

$$\frac{\partial}{\partial \hat{x}^+}\left(\dot{\hat{x}}^+\right) = \gamma\left(\frac{\partial}{\partial \hat{x}^+}\left(h_1(\hat{x}^+,\omega)\right) - \frac{\partial}{\partial \hat{x}^+}\left(h_2(\hat{x}^+,u)\right)\right) - k_o - K\frac{\partial}{\partial \hat{x}^+}\left(\hat{y}^+\right) \tag{5.15}$$

where

$$\frac{\partial h_1}{\partial x} = -\frac{\bar{\omega}k_r/\gamma}{\left(1+k_r\bar{x}/\gamma\right)^2} < 0, \forall \bar{x} \in [0;1], \tag{5.16}$$

$$\frac{\partial h_2}{\partial x} = \frac{1}{\left(1+k_a(1-\bar{x})/\gamma\right)^2}\left[\frac{k_d}{\gamma}\left(1+\frac{k_a}{\gamma}\left(1-\bar{x}\right)\right)+\frac{k_d}{\gamma}\bar{x}\frac{k_a}{\gamma}\right] > 0, \ \forall \bar{x} \in [0;1] \tag{5.17}$$

and

$$\frac{\partial y}{\partial x} = \frac{\partial h_1}{\partial x} + \alpha\frac{\partial h_2}{\partial x} \tag{5.18}$$

For $K >> \gamma$ (typically $\gamma \in [5.10^{-2}, 7.10^{-1}]$), the stability of this observer is simply given by the sign of $\frac{\partial \hat{y}^+}{\partial \hat{x}^+}$. When $\hat{x}^+$ increases from 0 to 1, $\frac{\partial \hat{y}^+}{\partial \hat{x}^+}$ is negative, becomes null at x^* and then is positive.

Similarly, the Jacobian of the second state observer is

$$\frac{\partial}{\partial \hat{x}^-}\left(\dot{\hat{x}}^-\right) = \gamma\left(\frac{\partial}{\partial \hat{x}^-}\left(h_1(\hat{x}^-,\omega)\right) - \frac{\partial}{\partial \hat{x}^-}\left(h_2(\hat{x}^-,u)\right)\right) - k_o + K\frac{\partial}{\partial \hat{x}^-}\left(\hat{y}^-\right) \tag{5.19}$$

Consequently, for $K >> \gamma$, this observer is unstable when $\hat{x}^-$ is below x^* and becomes stable for values of $\hat{x}^-$ above x^*.

The divergence $\hat{x}^+$ or $\hat{x}^-$ can be detected by comparing their predicted measurement (y^+ or y^-) to the true measurement y. Namely, one computes, over a sliding window,

$$c^{\pm} = \int_{t-T}^{t} (y^{\pm}(\tau) - y(\tau))^2 d\tau \tag{5.20}$$

When this variable exceeds a threshold, it is assumed that the observer diverges. Then, the value is discarded. Finally, the choice of the proper observer to obtain the "switching state observer" ($\hat{x}$ depicted in Figure 5.5) is carried out as follows:

- $\hat{x} = \hat{x}^+$, when $\hat{x}^-$ diverges, followed by a reset of $\hat{x}^-$ to the open loop estimate;
- $\hat{x} = \hat{x}^-$, when $\hat{x}^+$ diverges, followed by a reset of $\hat{x}^+$ to the open loop estimate;

Problems persist (wide and fast variations of $\hat{x}$, see Figure 5.5 at $t \approx 1400$ s for example) due to the switch between the two observers. One can easily imagine that using such an observer in a control strategy bearing on the coverage ratio can reveal troublesome.

5.2.2 Extended Kalman filter

Having described the concept of switching observers design, with simple constant gains, we now proceed with more flexible extended Kalman filter (EKF) for sake of improved performance and ease of tuning.

Two EKF are developed and initialized one on each side of the singularity x^*. They have the following expressions

$$\left\{ \begin{array}{rcl} \dot{\hat{x}}^+ & = & \gamma \left(u + h_1(\hat{x}^+, \omega) - h_2(\hat{x}^+, u) - \omega \right) - k_o \hat{x}^+ + K^+(y - \hat{y}^+) \\ \hat{y}^+ & = & h_1(\hat{x}^+, \omega) + \alpha h_2(\hat{x}^+, u) \end{array} \right. \tag{5.21}$$

and

$$\left\{ \begin{array}{rcl} \dot{\hat{x}}^- & = & \gamma \left(u + h_1(\hat{x}^-, \omega) - h_2(\hat{x}^-, u) - \omega \right) - k_o \hat{x}^- + K^-(y - \hat{y}^-) \\ \hat{y}^- & = & h_1(\hat{x}^-, \omega) + \alpha h_2(\hat{x}^-, u) \end{array} \right. \tag{5.22}$$

where $K^+ = S^+(t) \left(\hat{C}^+(t) \right)^T R^{-1}$, $K^- = S^-(t) \left(\hat{C}^-(t) \right)^T R^{-1}$, and S^+, S^- are obtained by the following Riccati equations:

$$\dot{S}^+(t) = \hat{A}^+(t) S^+(t) + S^+(t) \left(\hat{A}^+(t) \right)^T + Q - S^+(t) \left(\hat{C}^+(t) \right)^T R^{-1} \hat{C}^+(t) S^+(t) \tag{5.23}$$

$$\dot{S}^-(t) = \hat{A}^-(t) S^-(t) + S^-(t) \left(\hat{A}^-(t) \right)^T + Q - S^-(t) \left(\hat{C}^-(t) \right)^T R^{-1} \hat{C}^-(t) S^-(t) \tag{5.24}$$

where $\hat{A}^+(t) = \left. \dfrac{\partial f}{\partial x} \right|_{(\hat{x}^+(t), u(t))}$, $\hat{A}^-(t) = \left. \dfrac{\partial f}{\partial x} \right|_{(\hat{x}^-(t), u(t))}$, $\hat{C}^+(t) = \left. \dfrac{\partial h}{\partial x} \right|_{(\hat{x}^+(t), u(t))}$ and $\hat{C}^-(t) = \left. \dfrac{\partial h}{\partial x} \right|_{(\hat{x}^-(t), u(t))}$. R and Q are constant symmetric definite matrices.

Figure 5.6 represents the histories of x, $\hat{x}^+$, $\hat{x}^-$ and $\hat{x}_{OL}$ for a given operating condition ($T = 250$ °C, $\omega = 300$ ppm, $v = 4.5$ m.s^{-1}) and a sinusoidal input. Quickly, in this specific case, the two estimates $\hat{x}^+$ and $\hat{x}^-$ converges to x. One can note that the adaptation of the observer gain due to the Riccati equation (reduced gain when $\hat{x}$ is close to x and change of sign: refer to Figure 5.7 and 5.8) allows the observers to always converge to x. Indeed, close to the non observable point, $\hat{C}^+ = 0$, $\hat{C}^- = 0$ and the open loop dynamics allows both observers to track x. We do not have any proof of the convergence of this EKF, which is not unexpected (linearization being performed near the estimate, which does not allow any simple

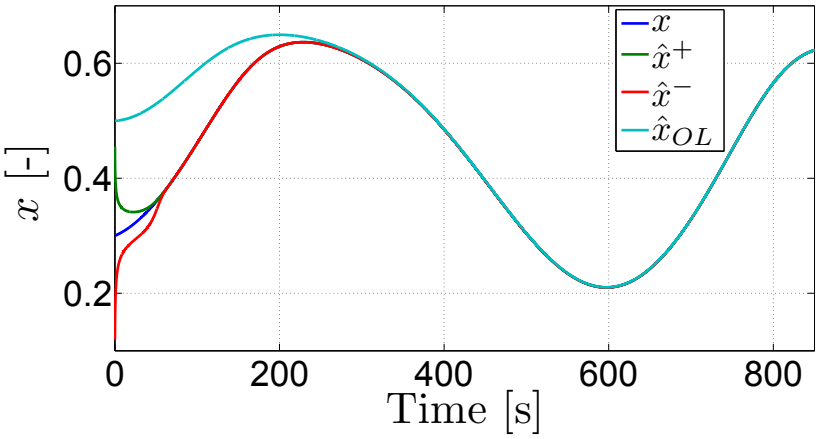

Figure 5.6: Representation of x, $\hat{x}^+$, $\hat{x}^-$ and $\hat{x}_{OL}$ as functions of time for the extended Kalman filters ($T = 250$ °C, $\omega = 300$ ppm, $v = 4.5$ m.s^{-1}), $u(t) = 17.10^{-3}\left(0.6 + \sin\left(\frac{2\pi}{600}t\right)\right)$. Simulation results.

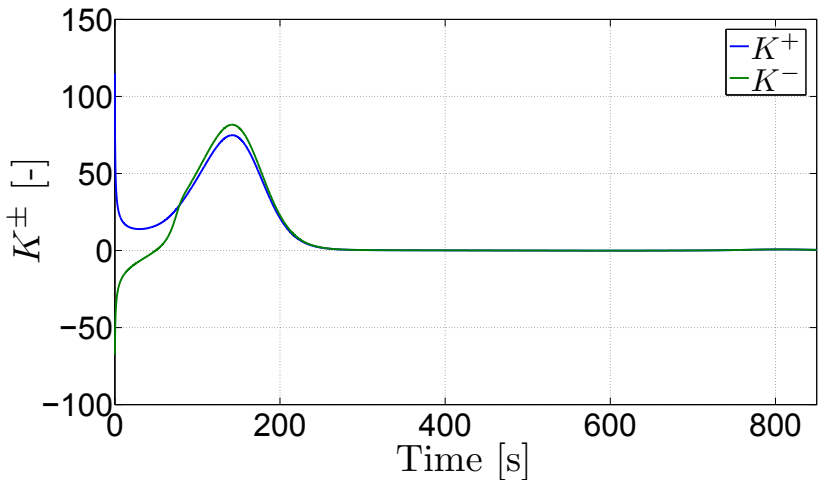

Figure 5.7: Representation of K^+ and K^- as functions of time for the extended Kalman filters ($T = 250$ °C, $\omega = 300$ ppm, $v = 4.5$ m.s^{-1}). Simulation results.

analysis). In practice both EKF seem to converge. Certainly, one behaves better than the other (depending on initialization). Investigation on the propagation of the estimate covariance should yield information on this.

In practice using two EKF is only justified at the initialization, to ensure that one of the two is in the vicinity of x. In all cases, the diverging one (if any) is re-initialized

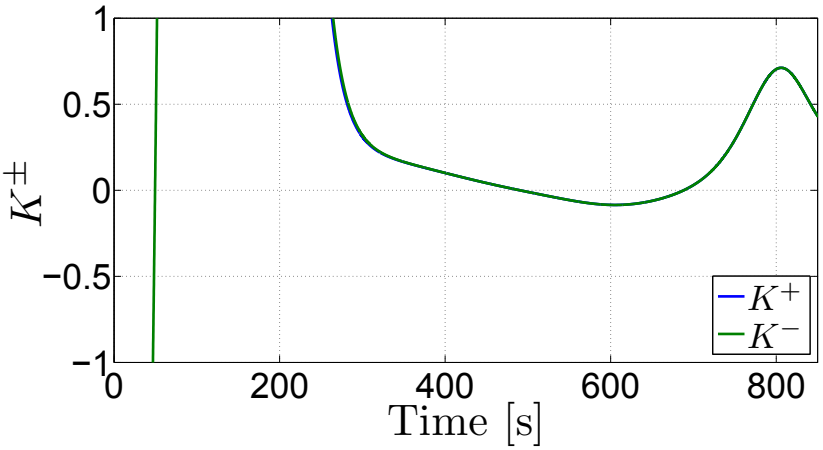

Figure 5.8: [Close-up view of Figure 5.7]. Representation of K^+ and K^- as functions of time for the extended Kalman filters ($T = 250$ °C, $\omega = 300$ ppm, $v = 4.5$ m.s^{-1}). Zoom on the y-axis between -1 and 1. Simulation results.

to the other one. Afterward, the observer gain is automatically adjusted (due to the Riccati equation) and the final state observer always converges to x. When the EKF $\hat{x}^+$ (or $\hat{x}^-$) passes close to the singularity (x^*) where the measurement is not instructive $\hat{C}^+ = 0$ (respectively $\hat{C}^- = 0$), the Kalman gain formula gives $K^+ = 0$ (respectively $K^- = 0$) which prevents any update of the estimate. This is an advantage over the constant gain switching observers. The behavior of the EKF is much smoother (see Figure 5.5 and 5.6).

Application of the switching EKF to a transient cycle To investigate the robustness of these two state observers, a NEDC cycle is performed in simulation using experimental data as inputs of the "reference model" and the observers. In this simulation a 15% modeling error on the NH_3 storage capacity Ω is introduced, as well as 10% bias and measurement noise on y (see Figure 5.9). The results are depicted in Figure 5.10.

To ensure good performance when x is small, and to prevent the observers from diverging repeatedly, the extended Kalman filters are tuned with a simple scheduling method. For this purpose, x^* is computed on line for each operating conditions. When $x^+ < x^*$ (or $x^- < x^*$), a set of parameters is considered for R and Q. Otherwise, when $x^+ > x^*$ (or $x^- > x^*$), the other (lower) set of parameters for R and Q is taken into consideration (since $\partial y^+/\partial x$, $\partial y^-/\partial x$ becomes rapidly significant when $\hat{x}^+ > x^*$, respectively $\hat{x}^- > x^*$). In Figure 5.10, at $t = 0$ s, $x = 0$, the two EKF observers and the open loop estimate are initialized at 0.1, 0.3 and 0.3, respectively. On the one hand, $\hat{x}^-$ rapidly converges since it is initialized close to x. On the

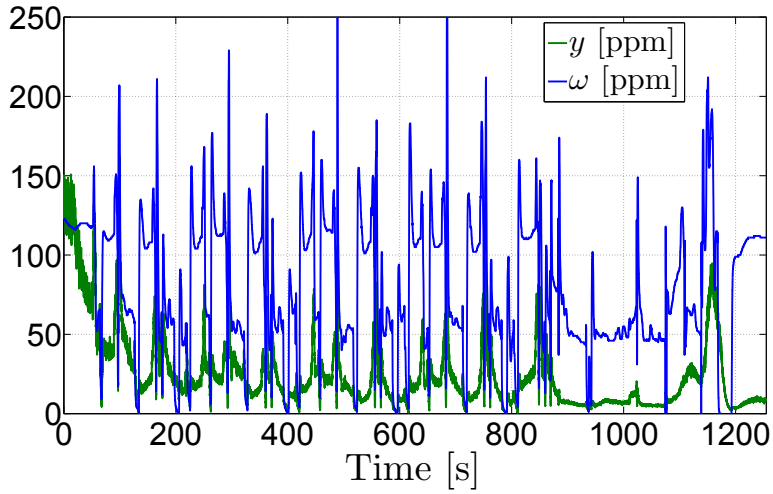

Figure 5.9: Representation of ω and y (with bias and multiplicative noise) as functions of time in transient conditions (NEDC cycle). Simulation results.

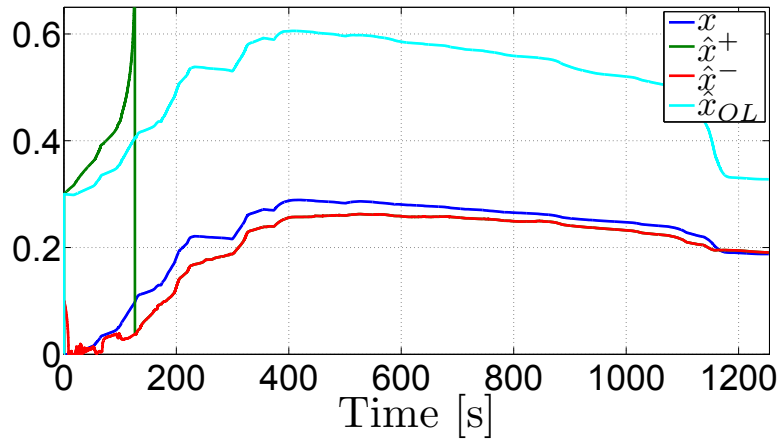

Figure 5.10: Representation of x, $\hat{x}^+$, $\hat{x}^-$ and $\hat{x}_{OL}$ as functions of time in transient conditions (NEDC cycle). A bias and a multiplicative noise is added on the measurement. Simulation results.

other hand, $\hat{x}^+$ diverges. When its divergence is detected, $\hat{x}^+$ is initialized to $\hat{x}^-$. Despite the modeling error, the bias and the noise applied to the measurement, the two observers reproduce with a good level of confidence the real coverage ratio x.

In Figure 5.11 the same NEDC cycle is performed with an additional disturbance of 50 ppm on the measurement between 500 and 600 s. In this case, the observers

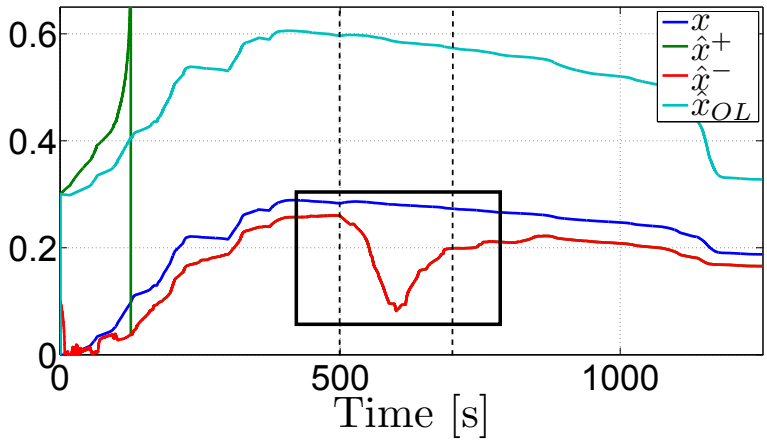

Figure 5.11: Representation of x, $\hat{x}^+$, $\hat{x}^-$ and $\hat{x}_{OL}$ as functions of time in transient conditions (NEDC cycle) with additional (50 ppm large) disturbance on the measurement between 500 and 600 s (in addition to the bias and the multiplicative noise of Figure 5.10). Simulation results.

are able to reject this disturbance relatively quickly.

5.3 Conclusion

In this chapter, we have explored several observer designs for our system featuring ambiguity in the measurement. First, an adaptive observer of Nussbaum type has proven that asymptotic reconstruction is possible under some assumptions of persistence of the excitation. Then, a switching observer and a switching EKF have been shown to lead to good performance even in transient situations. Beside the handy tuning possibility they offer, the main advantage of these solutions is that they can be adapted to the estimation of a spatially distributed coverage ratio. We believe they would represent valuable path to explore in the future.

Conclusion and perspectives

In this thesis, the problem of controlling the urea dosing upstream of a SCR (Selective Catalytic Reduction) catalyst as used in aftertreatment systems of diesel vehicles has been studied. Following the presentation of a detailed "reference model" for the SCR using results from the literature, a first contribution consists in several consecutive reductions to obtain the "reference model" well-suited for control design purposes.

A control strategy for an urea SCR system has been described. This is the second contribution of this thesis. It consists of an observer and a tracking loop. It controls the NH_3 coverage ratio and allows to mitigate the trade-off between NO_x conversion efficiency and tailpipe NH_3-slip. In this strategy, the NH_3 coverage ratio is estimated using the measurement of a commercial NO_x sensor located downstream of the catalyst. This sensor is cross-sensitive to NH_3. It is shown that, in theory, this cross-sensitivity could make the closed-loop system converge to an undesirable value of the coverage ratio as new equilibrium points are created by the feedback loop. The additional and undesirable equilibrium points are either discarded by the discrete time implementation of the control strategy (which makes them unstable) or detected with certainty from the available data. A parametric study is performed and shows how the observer gain has to be tuned so that the system can remain at all times in the vicinity of the setpoint of interest. As a result, the strategy leads to good performance in most cases, as has been demonstrated on a roller test bench under real transient conditions (several cycles with two different types of catalysts).

Finally, some extensions are detailed dealing with the design of observers using an ambiguous measurement. Two different types of observers are developed: an adaptive observer with Nussbaum gain and an EKF switching observer. These two solutions can be adapted to the estimation of a spatially distributed coverage ratio. This opportunity could be explored in the future.

Perspectives An important perspective would be to account for the adsorbed species not taking part in the NO_x reduction. Indeed, when the temperature is below 250°C, it seems that a second species competes for storage ((Way et al. (2009), Strots et al. (2009), Frobert et al. (2009), Olsson et al. (2008)). This phenomenon

of competition for adsorption is reproduced in Figure 5.12 (source Frobert et al. (2009)).

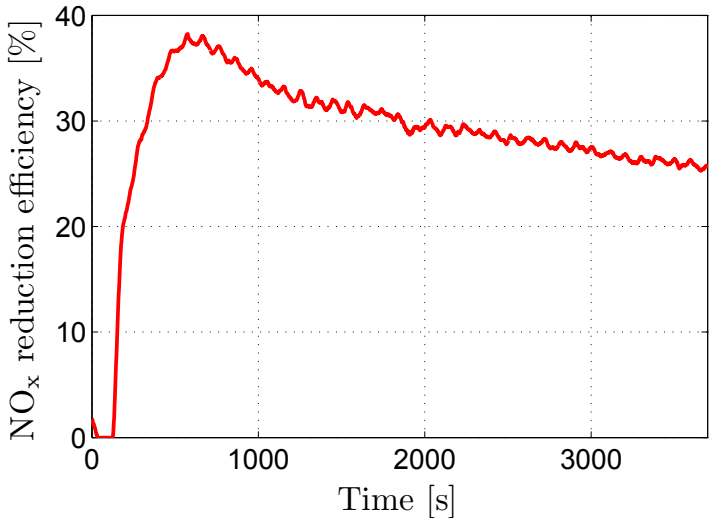

Figure 5.12: Example of NO_x reduction efficiency following the application of a NH_3 step flow, stressing competition for adsorption onto the SCR catalyst surface. Experimental results obtained with a Cu-zeolite catalyst (source Frobert et al. (2009)).

Figure 5.12 shows the efficiency of NO_x reduction obtained in an experiment on a SCR catalyst (Fe-zeolite), for an operating point corresponding to a low temperature ($T^{in} = 213°C$) and a strong gas flow rate (220 kg/h). At time $t = 100$ s, a constant amount of urea is injected with a value equal to the amount of inlet NO_x. The model of the SCR reactor with a single storage site would generate a (increasing) monotonic behavior. This is not the case.

Our understanding is as follows:

i. Initially, NH_3 and the second species are adsorbed on the same sites of the catalytic surface and the efficiency increases rapidly until it reaches a maximum;

ii. Then, the storage of the second species becomes predominant and the reduction efficiency slowly decreases.

Taking into account the storage of two species would allow one to assess the amount of NH_3 actually stored (useful storage) and would be helpful (and needed) in defining a coverage ratio target in these scenarios of cold catalyst.

Bibliography

ACEA. 'Diesel - Historical series by country in Western Europe 1990-2012', 2012. Available online: http://www.acea.be/, European Automobile Manufacturers' Association.

D. E. Ajtay. *Modal Pollutant Emissions Model of Diesel and Gasoline Engines*. PhD thesis, Swiss Federal Institute of Technology Zurich, 2005.

M. Benz, M. Hehn, C. H. Onder, & L. Guzzella. Model-based actuator trajectories optimization for a Diesel engine using a direct method. *Journal of Engineering for Gas Turbines and Power*, 133(3), 2011.

A. Bonfils, Y. Creff, O. Lepreux, & N. Petit. Closed-loop control of a SCR system using a NO_x sensor cross-sensitive to NH_3. In *Advanced Control of Chemical Processes*, pages 738–743, 2012.

A. Bonfils, Y. Creff, O. Lepreux, & N. Petit. Closed-loop control of a SCR system using a NO_x sensor cross-sensitive to NH_3. *Journal of Process Control*, 2013. To appear, DOI: 10.1016/j.jprocont.2013.08.010.

D. Chatterjee, T. Burkhardt, B. Bandl-Konrad, T. Braun, I. Nova, E. Tronconi, & C. Ciardelli. Numerical simulation of ammonia SCR catalytic converters: model development and application. *SAE International*, 2005-01-0965, 2005.

D. Chatterjee, T. Burkhardt, M. Weibel, E. Tronconi, I. Nova, & C. Ciardelli. Numerical simulation of $NO/NO_2/NH_3$ reactions on SCR catalytic converters: model development and application. *SAE International*, 2006-01-0468, 2006.

J. Chauvin, G. Corde, C. W. Vigild, N. Petit, & P. Rouchon. Air path estimation on Diesel HCCI engine. *SAE International*, 2006-01-1085, 2006.

J. N. Chi & H. F. M. Da Costa. Modeling and control of a urea-SCR aftertreatment system. In *Proceedings of SAE World Congress*, number 2005-01-0966. SAE International, 2005.

C. Ciardelli, I. Nova, E. Tronconi, B. Bandl-Konrad, D. Chatterjee, K. Ecke, & M. Weibel. SCR-DeNO$_x$ for diesel engine exhaust aftertreatment: unsteady-state kinetic study and monolith reactor modelling. *Chemical Engineering Science, Vol. 59*, 2004.

C. Ciardelli, I. Nova, E. Tronconi, D. Chatterjee, B. Bandl-Konrad, M. Weibel, & B. Krutzsch. Reactivity of NO/NO$_2$-NH$_3$ SCR system for diesel exhaust aftertreatment: Identification of the reaction network as a function of temperature and NO$_2$ feed content. *Applied Catalysis B: Environmental*, 70(1-4):80–90, 2007.

CITEPA. Centre Interprofessionnel Technique d'Etudes de la Pollution Atmosphérique, 2012. Available online: http://www.citepa.org/fr/.

J-M. Coron. On the stabilization of controllable and observable systems by an output feedback law. *Mathematics of Control signals and Systems*, 7(187-216), 1994.

M. Devadas, O. Krocher, & A. Wokaun. Catalytic investigation of Fe-ZSM5 in the selective catalytic reduction of NO$_x$ with NH$_3$. *Reaction Kinetics and Catalysis Letters*, 86:347–354, 2005. ISSN 0133-1736.

M. Devarakonda, G. Parker, J. H. Johnson, V. Strots, & S. Santhanam. Adequacy of reduced order models for model-based control in a urea-SCR aftertreatment system. In *Proceedings of SAE World Congress*, number 2008-01-0617. SAE International, 2008.

M. Devarakonda, G. Parker, J. H. Johnson, & V. Strots. Model based control system design in a urea-SCR aftertreatment system based on NH$_3$ sensor feedback. *International Journal of Automotive Technology, Vol. 10, No. 6, p.653-662*, 2009.

G. Dolanc, S. Strmčnik, & J. Petrovčič. NO$_x$ selective catalytic reduction control based on simple models. *Journal of Process Control*, 11(1):35–51, 2001.

C. J. Dore, J. W. L. Goodwin, J. D. Watterson, T. P. Murrells, N. R. Passant, M. M. Hobson, K. E. Haigh, S. L. Baggott, S. T. Pye, & P. J. Coleman. UK Emissions of air pollutants 1970 to 2001. *15th Annual Report from the UK National Atmospheric Emissions Inventory (NAEI). Annual Report National Environmental Technology Centre*, 2003.

P. Eastwood. *Critical topics in exhaust gas aftertreatment*. Research Studies Press, 2000.

H. L. Fang & H. F. M. Da Costa. Urea thermolysis and NO$_x$ reduction with and without SCR catalysts. *Applied Catalysis B: Environmental*, 46(1):17–34, 2003.

A. Frobert, Y. Creff, S. Raux, C. Charial, & A. Audouin. SCR for passenger car: the ammonia-storage issue on a Fe-ZSM-5 catalyst. *SAE International*, 2009-01-1929, 2009.

A. Frobert, S. Raux, Y. Creff, & E. Jeudy. About cross-sensitivities of NO_x sensors in SCR operation. *SAE International*, 2013-01-1512, 2013.

L. Gang. *Catalytic oxidation of ammonia to nitrogen*. Technische Universiteit Eindhoven, 2002.

J. B. Goodenough. Ceramic solid electrolytes. *Solid State Ionics*, 94(1):17–25, 1997.

A. Grossale, I. Nova, & E. Tronconi. Study of a Fe-zeolite-based system as NH_3-SCR catalyst for diesel exhaust aftertreatment. *Catalysis Today, Vol. 136*, 2008.

A. Grossale, I. Nova, E. Tronconi, D. Chatterjee, & M. Weibel. The chemistry of the NO/NO_2-NH_3 "fast SCR" reduction over Fe-ZMS-5 investigated by transient reaction analysis. *Journal of Catalysis, 256, 203-217*, 2008.

O. Hayat & E. Georgiadis. SCR and DPF optimized control strategies for diesel powertrains facing PC Euro 6 challenges. In *Proceeding of the 4th MinNOx conference*, Berlin, Germany, June 12-13, 2012.

A. Herman, M. C. Wu, D. Cabush, & M. Shost. Model based control of SCR dosing and OBD strategies with feedback from NH_3 sensors. *SAE International Journal of Fuels and Lubricants*, 2(1):375–385, 2009.

R. Hermann & A. Krener. Nonlinear controllability and observability. *IEEE Transactions on Automatic Control*, 22(5):728–740, 1977.

J. B. Heywood. *Internal combustion engine fundamentals*. McGraw-Hill New York, 1988.

M. F. Hsieh & J. Wang. Diesel engine selective catalytic reduction SCR ammonia surface coverage control using a computationally-efficient model predictive control assisted method. *ASME Dynamic Systems and Control Conference*, 2009.

M. F. Hsieh & J. Wang. Backstepping based nonlinear ammonia surface coverage ratio control for diesel engine selective catalytic reduction systems. *ASME Dynamic Systems and Control Conference*, 2009.

M. F. Hsieh & J. Wang. Observer-based estimation of selective catalytic reduction (SCR) catalyst ammonia storage. *Journal of Automobile Engineering, Vol. 224, No. D9*, 2010.

M. F. Hsieh & J. Wang. Development and experimental studies of a control-oriented SCR model for a two-catalyst urea-SCR system. *Control Engineering Practice*, 2010.

M. F. Hsieh & J. Wang. NO and NO_2 concentration modeling and observer-based estimation across a Diesel engine aftertreatment system. *Journal of Dynamic Systems, Measurement, and Control*, 133(4), 2011.

INERIS. Fiches et rapports de seuils de toxicité aiguë, 2004. Available online: http://www.ineris.fr/, Institut National de l'EnviRonnement Industriel et des riSques.

T. V. Johnson. Diesel emission control in review. In *US Dept. of Energy Diesel Engine Efficiency and Emissions Reduction (DEER) Conference, Detroit*, 2006.

N. Kato, H. Kurachi, & Y. Hamada. Thick film ZrO2 NO_x sensor for the measurement of low NO_x concentration. *SAE International*, 980170, 1998.

N. Kato, N. Kokune, B. Lemire, & T. Walde. Long term stable NO_x sensor with integrated in-connector control electronics. *SAE International*, 1999-01-0202, 1999.

H. K. Khalil. *Nonlinear systems (third edition)*, volume 3. Prentice Hall, 2002.

J. Y. Kim, G. Cavataio, J. E. Patterson, P. M. Laing, & C. K. Lambert. Laboratory studies and mathematical modeling of urea SCR catalyst performance. In *Proceedings of SAE World Congress*, number 2007-01-1573. SAE International, 2007.

M. Koebel & E. O. Strutz. Thermal and hydrolytic decomposition of urea for automotive Selective Catalytic Reduction systems: Thermochemical and practical aspects. *Industrial & Engineering Chemistry Research*, 42(10):2093–2100, 2003.

T. Laemmerhirt, D. Schmitt, C. Heidtkamp, & B. Lemire. Smart NO_x sensor: Functionality and applications in HDT and LDT vehicles. In *Proceeding of the 3rd MinNOx conference*, Berlin, Germany, June 29-30, 2010.

C. Lambert, R. Hammerle, R. Mc Gill, M. Khair, & C. Sharp. Technical advantages of urea SCR for light-duty and heavy-duty diesel vehicle applications. *SAE transactions*, 113(4):580–589, 2004.

O. Lepreux. Model based temperature control of a Diesel Oxydation Catalyst. *PhD thesis, ENSMP*, 2009.

R. Moos. A brief overview on automotive exhaust gas sensors based on electroceramics. *Internal Journal of Applied Ceramics Technology*, 2:401–413, 2005.

K. S. Narendra & A. M. Annaswamy. Stable adaptive systems. *Dover Publications*, 2005.

R. D. Nussbaum. Some remarks on a conjecture in parameter adaptive control. *Systems and Control Letters*, 3(243-246), 1983.

S. H. Oh & J. C. Cavendish. Transients of monolithic catalytic converters. response to step changes in feedstream temperature as related to controlling automobile emissions. *Industrial & Engineering Chemistry Product Research and Development*, 21(1):29–37, 1982.

L. Olsson, H. Sjövall, & R. Blint. A kinetic model for ammonia selective catalytic reduction over Cu-ZMS-5. *Applied Catalysis B: Environmental, 81, 203-217*, 2008.

L. Praly. Observation $y = x^2$. Technical report, Centre Automatique et Systmes, MINES ParisTech, April 2$^{\text{nd}}$, 1992.

C. Quérel, O. Grondin, & C. Letellier. State of the art and analysis of control oriented NO_x models. *SAE International*, 2012-01-0723, 2012.

C. Quérel, A. Bonfils, O. Grondin, & Y. Creff. Control of a SCR system using a virtual NO_x sensor. In *7th IFAC Symposium on Advances in Automotive Control*, Tokyo, Japan, Sept. 4-7, 2013.

C. M. Schär. *Control of a Selective Catalytic Reduction Process*. PhD thesis, Swiss Federal Institute of Technology Zurich, 2003.

C. M. Schär, C. H. Onder, H. P. Geering, & M. Elsener. Control-oriented model of an SCR catalytic converter system. In *Proceedings of SAE World Congress*, number 2004-01-0153. SAE International, 2004.

C. M. Schär, C. H. Onder, & H. P. Geering. Control of an SCR catalytic converter system for a mobile heavy-duty application. *IEEE Transactions on Control Systems Technology*, 14(4):641–653, 2006.

A. Schuler, M. Votsmeier, S. Malmberg, J. Gieshoff, A. Drochner, H. Vogel, & P. Kiwic. Dynamic model for the selective catalytic reduction of NO with NH_3 on Fe-zeolite catalysts. In *Proceedings of SAE World Congress*, number 2008-01-1323. SAE International, 2008.

S. Skarlis, D. Berthout, A. Nicolle, C. Dujardin, & P. Granger. Multisite modeling of NH_3 adsorption and desorption over Fe-ZSM5. *The Journal of Physical Chemistry C*, 116(15):8437–8448, 2012.

I. M. Sobol. Global sensitivity indices for nonlinear mathematical models and their Monte Carlo estimates. *Mathematics and Computers in Simulation*, 55(1-3):271–280, 2001.

H. J. Stein. Diesel oxidation catalysts for commercial vehicle engines: strategies on their application for controlling particulate emissions. *Applied Catalysis B: Environmental*, 10(1):69–82, 1996.

V. O. Strots, S. Santhanam, B. J. Adelman, G. A. Griffin, & E. M. Derybowski. Deposit formation in urea-SCR systems. *SAE International*, 2009-01-2780, 2009.

P. Tennison, C. Lambert, & M. Levin. NO_x control development with urea SCR on a diesel passenger car. In *Proceedings of SAE World Congress*, number 2004-01-1291. SAE International, 2004.

A. N. Tikhonov. Systems of differential equations containing small parameters in the derivatives. *Mat. Sb. (N.S.)*, 31(73):575–586, 1952.

D. Upadhyay & M. J. Van Nieuwstadt. Model based analysis and control design of a urea-SCR $DeNO_x$ aftertreatment system. *ASME Journal of Dynamic Systems, Measurement, and Control. Vol.128*, 2006.

M. J. Van Nieuwstadt & P. Tennison. Control method and system for diesel particulate filter regeneration, 2006. US Patent 7047 729.

T. Walde & O. Nakasone. Smart NO_x sensor - Application in diesel systems. In *5^{th} Car Training Institute Exhaust Systems Forum*, Nürtingen, Germany, 2007.

P. Way, K. Viswanathan, P. Preethi, A. Gilb, N. Zambon, & J. Blaisdell. SCR performance optimization through advancements in aftertreatment packaging. *SAE International*, 2009-01-0633, 2009.

F. Willems, R. Cloudt, E. Van Den Eijnden, M. Van Genderen, R. Verbeek, B. De Jager, W. Boomsma, & I. Van Den Heuvel. Is closed-looped SCR control required to meet future emission target? *SAE International*, 2007-01-1574, 2007.

C. Winkler, P. Flörchinger, M. D. Patil, J. Gieshoff, P. Spurk, & M. Pfeifer. Modeling of SCR DeNOx catalyst - Looking at the impact of substrate attributes. In *Proceedings of SAE World Congress*, number 2003-01-0845. SAE International, 2003.

Appendix A

Development of the SCR model

This appendix details the development of the SCR model obtained by mass balances and presented in Section 1.3.

Consider the mass balance equation for a perfectly stirred reactor, fed by a monophasic gas:

$$\dot{m}_i = F_i^{in} - F_i - \sum_{j=1}^{N_R} \gamma_{ij} r'_j V \tag{A.1}$$

where V is the total volume occupied by gases in the reactor, m_i [kg], F_i^{in} and F_i [kg.s^{-1}] are, respectively, the mass, the mass flow rates at the inlet and at the outlet of the reactor, of each species i. Here, r'_j [kg.m^{-3}.s^{-1}] is the the reaction rate for reaction j, N_R [-] is the number of reactions, and γ_{ij} [-] is the stoichiometric coefficient of each species i in the reaction j.

L [m] is the length of the reactor and S [m^2] the useful cross-sectional area. Respectively, χ_i [-], v [m.s^{-1}], m [kg] and F [kg.s^{-1}] are the mass fraction of the species i, the gas velocity, the total mass and mass flow rate of the gases in the reactor.

Note $m_i = m\chi_i = \rho_g LS\chi_i$, $F_i = F\chi_i = \rho_g Sv\chi_i$ and assume that the gases density ρ_g [kg.m^{-3}] and the volume occupied by the gases in the reactor V [m^3] are constant.

Then, (A.1) gives

$$\dot{\chi}_i = \frac{v}{L}\left(\chi_i^{in} - \chi_i\right) - \frac{1}{\rho_g}\sum_{j=1}^{N_R} \gamma_{ij} r'_j \tag{A.2}$$

The mass concentrations C_i^m [kg.m^{-3}] for each species i are given by: $C_i^m = \dfrac{m_i}{V} = \dfrac{m}{V}\chi_i = \rho_g \chi_i$.

In addition, $m = Mn$, $m_i = M_i n_i$, gives $n = \dfrac{m}{M}$ and $n_i = \dfrac{m_i}{M_i}$ where n, n_i [mol] and M, M_i [kg.mol^{-1}] are the total number of moles and the molecular mass for the

gases and a species i, respectively. Also, $n_i = ny_i$, where y_i [-] is the molar fraction of species i.

Finally, $y_i = \dfrac{n_i}{n} = \chi_i \dfrac{M}{M_i}$ and the molar concentration for a species i is $C_i = \dfrac{n_i}{V} = \dfrac{\rho_g}{M} y_i$ [mol.m^{-3}], or equivalently, $C_i = \dfrac{\rho_g}{M_i}\chi_i$.

In conclusion, the mass balances (A.1) can also be rewritten as

$$\underbrace{\dot{C}_i}_{[\text{mol.m}^{-3}.\text{s}^{-1}]} = \overbrace{\underbrace{\frac{v}{L}}_{[\text{m}]}}^{[\text{m.s}^{-1}]} \underbrace{\left(C_i^{in} - C_i\right)}_{[\text{mol.m}^{-3}]} - \underbrace{\frac{1}{M_i}}_{[\text{kg.mol}^{-1}]} \overbrace{\sum_{j=1}^{N_R} \gamma_{ij} r'_j}^{[\text{kg.m}^{-3}.\text{s}^{-1}]} \tag{A.3}$$

Generalizing the mass balances in a spatially distributed manner, one gets, for a one-dimensional plug-flow reactor model,

$$\frac{\partial C_i}{\partial t} = -v\frac{\partial C_i}{\partial s} - \frac{1}{M_i}\sum_{j=1}^{N_R} \gamma_{ij} r'_j \tag{A.4}$$

where $s \in [0, L]$ represents the axial direction of the reactor. A source term is added at the spatial boundary.

In this thesis, one is interested in the following species (considered in the SCR "reference model"): NH_3, NO, NO_2 in gas phase and adsorbed NH_3. Therefore, the adsorption/desorption process and the reactions (1.3), (1.4) and (1.6) have to be taken under consideration. Then, one focuses here on the SCR model with three states: NH_3, NO_x in gas ,phase and adsorbed NH_3 (NO and NO_2 are lumped into the total amount of NO_x; a global reaction is considered for NO_x reduction). Adaptation to the four states model (NO and NO_2) is straightforward. the $k'_j, j \in \{\text{a,d,r,o}\}$ denotes the kinetics rates for adsorption, desorption of NH_3, NO_x reduction and NH_3 direct oxidation by O_2, respectively. We now write the balance equations.

NH_3 in gas phase

$$\frac{\partial C_{\text{NH}_3}}{\partial t} = -v\frac{\partial C_{\text{NH}_3}}{\partial s} - \frac{1}{M_{\text{NH}_3}}\left(k'_{\text{a}} C_{\text{NH}_3}\Omega(1-x) - k'_{\text{d}}\Omega x\right) \tag{A.5}$$

where x [-] is the NH_3 coverage ratio (ratio between the number of occupied catalytic sites and the total number of catalytic sites) and Ω [mol.m^{-3}] is the NH_3 storage capacity.

NO_x in gas phase

$$\frac{\partial C_{NO_x}}{\partial t} = -v\frac{\partial C_{NO_x}}{\partial s} - \frac{1}{M_{NO_x}}k'_r C_{NO_x}\Omega x \tag{A.6}$$

Adsorbed NH_3 The evolution of adsorbed NH_3 is only due to the chemical reactions involving this species

$$\dot{m}_{NH_3^*} = \sum_{j=1}^{N_R}\gamma_{ij}r'_j V$$

with $m_{NH_3^*} = xV\Omega M_{NH_3}$, and $\dot{m}_{NH_3^*} = V\Omega M_{NH_3}\frac{\partial x}{\partial t} = \sum_{j=1}^{N_R}\gamma_{ij}r'_j V$, we get

$$\Omega\frac{\partial x}{\partial t} = \frac{1}{M_{NH_3}}\sum_{j=1}^{N_R}\gamma_{ij}r'_j$$

Finally, the evolution of adsorbed NH_3 along the reactor is governed by the following differential equation:

$$\Omega\frac{\partial x}{\partial t} = \frac{k'_a}{M_{NH_3}}C_{NH_3}\Omega(1-x) - \frac{k'_d}{M_{NH_3}}\Omega x - \frac{k'_r}{M_{NH_3}}\frac{M_{NH_3}}{M_{NO_x}}C_{NO_x}\Omega x - \frac{k'_o}{M_{NH_3}}\Omega x \tag{A.7}$$

Gathering (A.5), (A.6) and (A.7), denoting $z_1 = C_{NO_x}$, $z_2 = C_{NH_3}$, $k_a = \frac{k'_a}{M_{NH_3}}$, $k_d = \frac{k'_d}{M_{NH_3}}$, $k_r = \frac{k'_r}{M_{NO_x}}$ and $k_o = \frac{k'_o}{M_{NH_3}}$, the SCR one-dimensional distributed parameters model is rewritten as

$$\begin{cases} \frac{\partial x}{\partial t} = k_a z_2(1-x) - k_d x - k_r z_1 x - k_o x \\ \frac{\partial z_1}{\partial t} = -v\frac{\partial z_1}{\partial s} - \Omega k_r z_1 x \\ \frac{\partial z_2}{\partial t} = -v\frac{\partial z_2}{\partial s} - \Omega k_a z_2(1-x) + \Omega k_d x \end{cases} \tag{A.8}$$

Appendix B

Control of a non-constant coverage ratio profile

In Chapter 2 we have discussed the possibility of controlling the coverage ratio about a non equilibrium (and so non constant) profile. We now detail this discussion and investigate the potential beneficial effects of this. The discussion starts with a simple linear model and then introduces nonlinearities.

B.1 Linear case

Consider a linear model of the SCR catalyst stemming from a spatially discretization into two equal parts

$$\begin{cases} \tau_1 \dot{x}_1 &= -x_1 + K_1 u \\ \tau_2 \dot{x}_2 &= -x_2 + K_2 x_1 \end{cases} \tag{B.1}$$

where x_1 and x_2 represents the coverage ratio of each part. τ_1, τ_2, K_1 and K_2 are constant parameters.

It is simple to steer the system from the equilibrium $\begin{pmatrix} 0 \\ 0 \end{pmatrix}$ at $t = 0$ to any point $\begin{pmatrix} a \\ b \end{pmatrix}$ at time $t = T$. This is a motion planning problem for a cascade system.

For this purpose, the system can be put into the (Brunovsky) controller normal form

$$\begin{aligned} \ddot{x}_2 &= -\frac{1}{\tau_2}\dot{x}_2 + \frac{K_2}{\tau_2}\dot{x}_1 = -\frac{1}{\tau_2}\left(-x_2 + K_2 x_1\right) + \frac{K_2}{\tau_2}\left(-x_1 + K_1 u\right) \\ &= -\left(\frac{1}{\tau_1} + \frac{1}{\tau_2}\right)\dot{x}_2 - \frac{1}{\tau_1 \tau_2} x_2 + \frac{K_1 K_2}{\tau_1 \tau_2} u \end{aligned} \tag{B.2}$$

and the target expressed in the $\begin{pmatrix} x_2 \\ \dot{x}_2 \end{pmatrix}$ coordinates $\begin{cases} x_2(T) &= b \\ \dot{x}_2(T) &= -\dfrac{b}{\tau_2} + \dfrac{K_2 a}{\tau_2} \end{cases}$

Additionally, one may wish to take the following constraints into consideration

$$\begin{cases} \displaystyle\int_0^T (x_1(t) + x_2(t))\, dt \geq A \\ \displaystyle\max_{t\in[0,T]} \; x_2(t) \leq B \\ u(t) \geq 0, \text{ for } t \in [0, T] \end{cases}$$

These constraints express

i. that the total coverage averaged over the time horizon should remain above some threshold A, which guarantees some minimum NO_x reduction efficiency;

ii. that the coverage ratio close to the outlet should remain below some constant B, to avoid NH_3-slip;

iii. that the system can only be filled, and that no NH_3 can be removed.

Among all possible signals, a simple class of input signal is now considered. The input is assumed to be a sinusoid. The system being asymptotically stable (without any input), when driven by the input signal, it converges to a periodic asymptotic regime x_2^{as}.

It is a well known fact that when a biased sinusoid signal is applied as input of the asymptotically stable system (B.1) which constitutes an Input to State stable system, then the states asymptotically sinusoidally oscillate around their average values.

In details the system responds linearly to the two components of the input signal. Note $H(s)$ the transfer function of the state-space system (B.1). The output of the system is, asymptotically,

$$x_2^{\text{as}}(t) = \beta \left| H\left(i\frac{2\pi}{T}\right)\right| . \frac{1}{K_1 K_2} \sin\left(\frac{2\pi}{T}\left(t + \arg H\left(i\frac{2\pi}{T}\right)\right)\right) + \alpha . |H(0)|$$

and one directly checks that

$$\frac{1}{T}\int_0^T x_2^{\text{as}}(t)dt = \alpha K_1 K_2 = K_1 K_2 \frac{1}{T}\int_0^T u(t)dt$$

Similarly

$$\frac{1}{T}\int_0^T x_1^{\text{as}}(t)dt = \alpha K_1$$

Therefore the average reactor coverage ratio

$$\int_0^T (x_1^{\text{as}}(t) + x_2^{\text{as}}(t))\, dt = \alpha K_1 (1 + K_2)$$

The sinusoid signal (of magnitude β) has no effect on this quantity and thus no effect on the efficiency.

The same reasoning could be applied to any refined spatial discretization of the reactor. We conclude here that, in the linear representation of the system dynamics, it is useless to consider non equilibrium targets for the coverage ratio variable.

B.2 Non-linear case

In this section, the SCR model (including chemical reactions) derived from (1.30) is considered and discretized in two equal zones. This yields

$$\left\{\begin{array}{rcl} \dot{x}_1 &=& \gamma\left(u + h_1(x_1,\omega) - h_2(x_1,u) - \omega\right) - k_{\mathrm{o}} x_1 \\ \dot{x}_2 &=& \gamma\left(h_2(x_1,u) + h_1(x_2,h_1(x_1,\omega)) - h_2(x_2,h_2(x_1,u)) - h_1(x_1,\omega)\right) - k_{\mathrm{o}} x_2 \end{array}\right. \tag{B.3}$$

where x_1 and x_2 represent the coverage ratio of each part, $h_1(.)$ and $h_2(.)$ are defined in (1.29), and γ is a constant defined in § 1.4.3.

We set $W(x_1,u) \triangleq h_2(x_1,u) = \dfrac{u + k_{\mathrm{d}} x_1/\gamma}{1 + k_{\mathrm{a}}(1-x_1)/\gamma}$ viewed as a function of time.

This leads

$$\dot{W} = \frac{\partial h_2}{\partial x_1}\dot{x}_1 + \frac{\partial h_2}{\partial u}\dot{u}$$

then

$$\dot{W} = \frac{\partial h_2}{\partial x_1}\left[\gamma\left(u + h_1(x_1,\omega) - W - \omega\right) - k_{\mathrm{o}} x_1\right] + \frac{\partial h_2}{\partial u}\dot{u}$$

and finally

$$\dot{u} = \left(\frac{\partial h_2}{\partial u}\right)^{-1}\left[\dot{W} + \frac{\partial h_2}{\partial x_1}\left[\gamma\left(W - h_1(x_1,\omega) + \omega\right) + k_{\mathrm{o}} x_1\right]\right] - \gamma\left(\frac{\partial h_2}{\partial u}\right)^{-1}\frac{\partial h_2}{\partial x_1}u \tag{B.4}$$

This equation is a dynamic feedback defining the control input u (it can be viewed as a first order nonlinear filter).

We now use it to solve a motion planing problem. The trajectory on W denoted W^{sp} is defined as a function of the desired evolutions of x_2 and $\dot{x}_2$, denoted x_2^{sp} and $\dot{x}_2^{\mathrm{sp}}$, respectively.

For practical implementation, we compute W^{sp} from the second differential equation in (B.3)

$$\dot{x}_2 = \gamma\left(W + h_1(x_2,h_1(x_1,\omega)) - h_2(x_2,W) - h_1(x_1,\omega)\right)$$

This leads, implicitly, to

$$W^{\mathrm{sp}} = \Phi(x_2^{\mathrm{sp}}, \dot{x}_2^{\mathrm{sp}}, u)$$

From which we get $\dot{W}^{\text{sp}}$

$$\dot{W}^{\text{sp}} = \Psi(\ddot{x}_2^{\text{sp}}, \dot{x}_2^{\text{sp}}, x_2^{\text{sp}}, u, \Phi(x_2^{\text{sp}}, \dot{x}_2^{\text{sp}}, u))$$

Finally, we compute the control input $u(t)$ derived from dynamic feedback (B.4) and apply it to the SCR model (B.3).

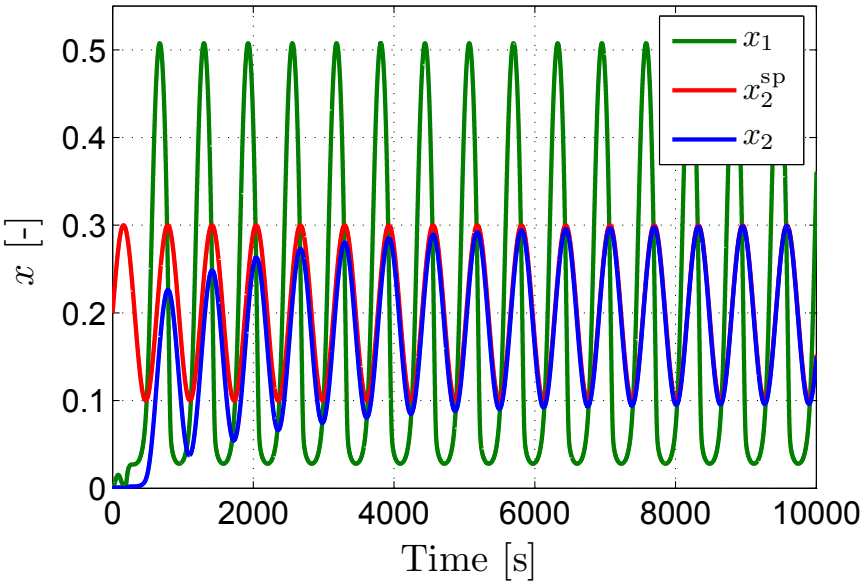

Figure B.1: Evolution of x_1, x_2 and x_2^{sp} as function of time resulting from trajectory tracking of x_2 to x_2^{ref}. Simulation results.

From the procedure described above and thanks to the stability of the dynamics, we are able to make x_2 converge to its reference trajectory x_2^{sp}, because the system is stable as shown in Figure B.1 where the histories of x_1, x_2 and x_2^{sp} are depicted. The input signal u applied to the system is reported in Figure B.2. Here the chosen output signal is $x_2^{\text{sp}} = 0.2 + 0.1 \sin\left(\frac{2\pi}{500} t\right)$.

It is therefore possible to control the coverage ratio at the end of the SCR catalyst by solving a motion planning problem and by inverting the system dynamics.

The observed nonlinear regime can be evaluated in terms of overall average efficiency. For the chosen $x_2^{\text{sp}} = 0.2 + 0.1 \sin\left(\frac{2\pi}{500} t\right)$, the average coverage ratio is, numerically,

$$\int_0^T (x_1^{\text{as}}(t) + x_2^{\text{as}}(t))\, dt = \underbrace{0.22}_{\text{equilibrium term}} + \underbrace{0.01}_{\text{nonlinear contribution}}$$

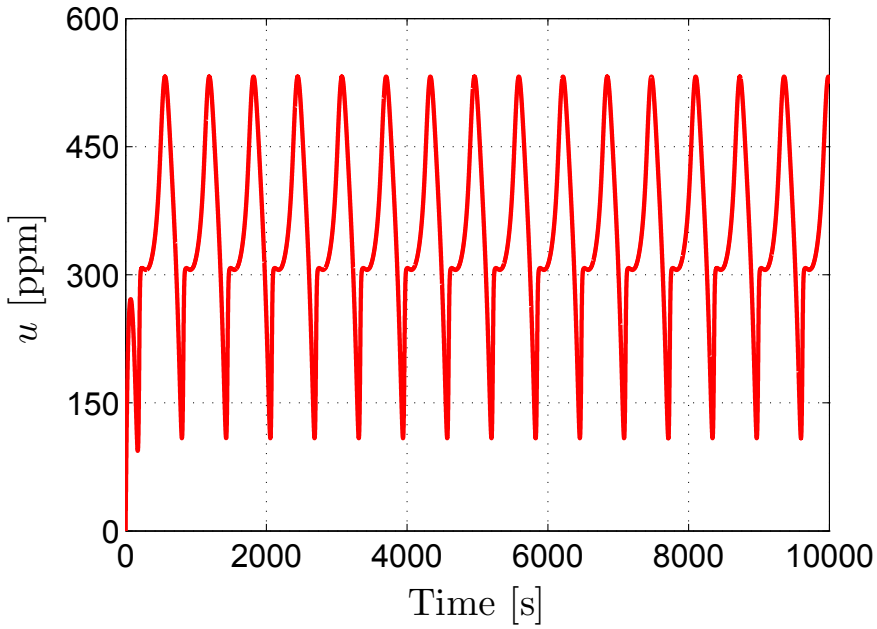

Figure B.2: Evolution of u as function of time resulting from trajectory tracking of x_2 to x_2^{ref}. Simulation results.

and the average efficiency is

$$\int_0^T \eta_{\text{NO}_\text{x}}(t)dt = \underbrace{76}_{\text{equilibrium term}} + \underbrace{0.8}_{\text{nonlinear contribution}} \quad \%$$

The premium associated considering this time varying reference is negligible, and does not balance the risks of NH_3-slip.

Appendix C

Observability analysis with an ideal NO_x sensor or a NH_3 sensor

Prior to the control design proposed in Chapter 3, the observability of the system is analyzed. First, the use of a NH_3 sensor and then of an ideal NO_x sensor are discussed.

C.1 NH_3 sensor: measurement of the outlet NH_3 molar concentration

In this part the considered measurement is

$$y = z_2 \tag{C.1}$$

To study the observability of the system consisting of (1.25) and (C.1), one considers two identical output histories z_2 and $\bar{z}_2$ over a finite time horizon $T > 0$, such that

$$\forall t \in [0, T], z_2(t) = \bar{z}_2(t) \tag{C.2}$$

and one has to study if the initial conditions are distinguishable (see Hermann & Krener (1977)).

Equation (C.2) implies $\boxed{z_2(0) = \bar{z}_2(0)}$

Then, (C.2) leads to $\forall t \in [0, T], \dot{z}_2 = \dot{\bar{z}}_2$. Or, equivalently, using the third equation of model (1.25)

$$\text{and} \quad \begin{array}{rcl} \frac{v}{L}(u - z_2) - \Omega k_a z_2 (1 - x) + \Omega k_d x & = & \frac{v}{L}(u - \bar{z}_2) - \Omega k_a \bar{z}_2 (1 - \bar{x}) + \Omega k_d \bar{x} \\ \Omega (k_a z_2 + k_d) x & = & \Omega (k_a z_2 + k_d) \bar{x} \end{array}$$

As $z_2 = \bar{z}_2$, $z_2 > 0$, $\Omega > 0$, $k_a > 0$ and $k_d > 0$, one obtains $\forall t \in [0, T], x(t) = \bar{x}(t)$ and consequently $\boxed{x(0) = \bar{x}(0)}$.

Finally, let us differentiate the condition $x(t) = \bar{x}(t)$. Due to the first equation of the system (1.25), we get

$$k_a z_2 (1 - x) - k_d x - k_r z_1 x = k_a \bar{z}_2 (1 - \bar{x}) - k_d \bar{x} - k_r \bar{z}_1 \bar{x} \tag{C.3}$$

and because we already know $z_2 = \bar{z}_2$, $x = \bar{x}$, $k_r \neq 0$. One obtains $\forall t \in [0, T], z_1(t) = \bar{z}_1(t)$ and $\boxed{z_1(0) = \bar{z}_1(0)}$

In conclusion, two identical output histories y and $\bar{y}$ such as $\forall t \in [0, T], y = \bar{y}$, with T a finite time implies $\begin{cases} z_1(0) = \bar{z}_1(0) \\ z_2(0) = \bar{z}_2(0) \\ x(0) = \bar{x}(0) \end{cases}$. Regardless of the input u, all the initial conditions are distinguishable. Thus, $\forall u \in \Re$ the system consisting of (1.25) and (C.1) is observable.

Having a NH_3 sensor located at the outlet would thus be a good sensor. This solution is discarded because a measurement of the NO_x molar concentration downstream of the SCR catalyst is needed in all cases for diagnostic requirements in Euro 6 standards. One can not add the NH_3 sensor.

C.2 Ideal NO_x sensor: measurement of the outlet NO_x molar concentration

In this part one considers a perfect NO_x sensor that implies the following measurement

$$y = z_1 \tag{C.4}$$

To study the observability of the system consisting of (1.25) and (C.4), we consider again two identical output histories z_1 and $\bar{z}_1$

$$\forall t \in [0, T], z_1(t) = \bar{z}_1(t). \tag{C.5}$$

Directly, equation (C.5) implies $\boxed{z_1(0) = \bar{z}_1(0)}$

Then, (C.5) leads to $\forall t \in [0, T], \dot{z}_1 = \dot{\bar{z}}_1$. Or equivalently, using the second equation of model (1.25)

$$\Omega k_r z_1 x = \Omega k_r \bar{z}_1 \bar{x}$$

As $z_1 = \bar{z}_1 > 0$, $\Omega > 0$ and $k_\mathrm{r} > 0$, one obtains $\forall t \in [0,T], x(t) = \bar{x}(t)$ and consequently $\boxed{x(0) = \bar{x}(0)}$.

Finally, $\forall t \in [0,T], x(t) = \bar{x}(t)$ implies, due to the first equation of the system (1.25),

$$k_\mathrm{a} z_2 (1-x) - k_\mathrm{d} x - k_\mathrm{r} z_1 x \quad = \quad k_\mathrm{a} \bar{z}_2 (1-\bar{x}) - k_\mathrm{d} \bar{x} - k_\mathrm{r} \bar{z}_1 \bar{x} \tag{C.6}$$

with $z_1 = \bar{z}_1$, $x = \bar{x}$, $k_\mathrm{a} \neq 0$ and $k_\mathrm{d} \neq 0$. One obtains provided that x remains at all time away from 1, $\forall t \in [0,T], x = \bar{x}$ implies $\forall t \in [0,T], z_2 = \bar{z}_2$ and $\boxed{z_2(0) = \bar{z}_2(0)}$

Again, the initial condition is distinguishable. Thus, $\forall u \in \Re$ and $\forall x \neq 1$, the system consisting of (1.25) and (C.4) is observable (as already noted in Upadhyay & Van Nieuwstadt (2006)).

One such sensor would be highly desirable (and is commonly considered in studies) but, unfortunately, no such sensor exists at the industrial level.

Appendix D

Stability analysis

In Chapter 3 the analysis of the closed-loop equilibria using the proposed control strategy is performed. Some computation details of this analysis are discussed in this appendix. The discussion starts with additional proofs used in the description of the (continuous time) closed-loop dynamics stability, then the case of the discrete time implementation is addressed.

D.1 Stability analysis of the continuous-time closed-loop dynamics

D.1.1 Saturated control

The equilibrium points $\left(\bar{x}, \bar{\hat{x}}\right)$ of system (3.5) are given by

$$0 = \frac{\bar{\omega}}{1+k_{\mathrm{r}}\bar{x}/\gamma} - \frac{k_{\mathrm{d}}\bar{x}/\gamma}{1+k_{\mathrm{a}}(1-\bar{x})/\gamma} - \bar{\omega} - \frac{k_{\mathrm{o}}}{\gamma}\bar{x} \tag{D.1}$$

and

$$0 = \gamma\left(\frac{\bar{\omega}}{1+k_{\mathrm{r}}\bar{x}/\gamma} + \alpha\frac{k_{\mathrm{d}}\bar{x}/\gamma}{1+k_{\mathrm{a}}(1-\bar{x})/\gamma} - \bar{\omega}\right) - k_{\mathrm{o}}\bar{\hat{x}} - k_L\left(\bar{\hat{x}} - x^{\mathrm{c}}\right) \tag{D.2}$$

Equivalently (D.2) gives

$$\bar{\hat{x}} = \frac{\gamma}{k_{\mathrm{o}}+k_L}\left(\frac{\bar{\omega}}{1+k_{\mathrm{r}}\bar{x}/\gamma} + \alpha\frac{k_{\mathrm{d}}\bar{x}/\gamma}{1+k_{\mathrm{a}}(1-\bar{x})/\gamma} - \bar{\omega}\right) + \frac{k_L}{k_{\mathrm{o}}+k_L}x^{\mathrm{c}}$$

while (D.1) gives

$$\begin{aligned} 0 = {} & \bar{\omega}\left(1+k_{\mathrm{a}}(1-\bar{x})/\gamma\right) - k_{\mathrm{d}}\bar{x}/\gamma\left(1+k_{\mathrm{r}}\bar{x}/\gamma\right) \\ & - \left(\bar{\omega} + \frac{k_{\mathrm{o}}}{\gamma}\bar{x}\right)\left(1+k_{\mathrm{a}}(1-\bar{x})/\gamma\right)\left(1+k_{\mathrm{r}}\bar{x}/\gamma\right) \end{aligned}$$

and

$$\begin{aligned} 0 &= -k_{\mathrm{d}}\bar{x}/\gamma\,(1+k_{\mathrm{r}}\bar{x}/\gamma) - \bar{\omega}\,(1+k_{\mathrm{a}}(1-\bar{x})/\gamma)\,k_{\mathrm{r}}\bar{x}/\gamma \\ &\quad -\frac{k_{\mathrm{o}}}{\gamma}\bar{x}\,(1+k_{\mathrm{a}}(1-\bar{x})/\gamma)\,(1+k_{\mathrm{r}}\bar{x}/\gamma) \end{aligned}$$

then

$$\begin{aligned} 0 &= \bar{x}\left[k_{\mathrm{d}}/\gamma\,(1+k_{\mathrm{r}}\bar{x}/\gamma) + \bar{\omega}\,(1+k_{\mathrm{a}}(1-\bar{x})/\gamma)\,k_{\mathrm{r}}/\gamma\right. \\ &\quad \left.+\frac{k_{\mathrm{o}}}{\gamma}\bar{x}\,(1+k_{\mathrm{a}}(1-\bar{x})/\gamma)\,(1+k_{\mathrm{r}}\bar{x}/\gamma)\right] \end{aligned}$$

One obtains three possible distinct roots for $\bar{x}$ which can be summarized in two distinct cases. These are detailed below:

i. The first solution is $\bar{x}=0$, to which corresponds $\bar{\hat{x}} = \dfrac{\gamma}{k_{\mathrm{o}}+k_L}(\bar{\omega}+0-\bar{\omega}) + \dfrac{k_L}{k_{\mathrm{o}}+k_L}\dfrac{\gamma\,(\bar{\omega}-\bar{\omega}-0)}{k_{\mathrm{r}}\bar{\omega}+0} = 0$. Around this equilibrium point, the Jacobian triangular form of the closed-loop dynamics has the following eigenvalues:

$$\begin{aligned} \gamma\left(\left.\frac{\partial h_1}{\partial x}\right|_{(0,\bar{\omega})}(x,\omega) - \left.\frac{\partial h_2}{\partial x}\right|_{(0,0)}(x,u)\right) - k_{\mathrm{o}} &= -\omega k_{\mathrm{r}}/\gamma \\ &\quad -\frac{1}{(1+k_{\mathrm{a}}/\gamma)^2}\left[k_{\mathrm{d}}/\gamma\,(1+k_{\mathrm{a}}/\gamma)\right] \\ &\quad -k_{\mathrm{o}} < 0 \end{aligned}$$

and $-(k_{\mathrm{o}}+k_L) < 0$.

Then, the closed-loop system is (locally) asymptotically stable around $(0\ \ 0)'$.

ii. The (two) other possible solutions are defined by

$$\begin{aligned} 0 &= k_{\mathrm{d}}/\gamma\,(1+k_{\mathrm{r}}\bar{x}/\gamma) + \bar{\omega}\,(1+k_{\mathrm{a}}(1-\bar{x})/\gamma)\,k_{\mathrm{r}}/\gamma \\ &\quad +\frac{k_{\mathrm{o}}}{\gamma}\bar{x}\,(1+k_{\mathrm{a}}(1-\bar{x})/\gamma)\,(1+k_{\mathrm{r}}\bar{x}/\gamma) \end{aligned} \tag{D.3}$$

This equation can be rewritten as a polynomial function of order 2 ($Ax^2+Bx+C=0$) which has a positive discriminant and thus has two distinct real solutions. However, one can easily understand that (D.3) has no physical solution (i.e. $\bar{x}\in[0,1]$) as, for all $\bar{x}\in[0,1]$, this equation is always positive (with $\gamma>0$, $k_{\mathrm{a}}>0$, $k_{\mathrm{d}}>0$, $k_{\mathrm{r}}>0$ and $k_{\mathrm{o}}>0$). These two non physical solutions must be discarded.

D.1.2 Unsaturated control

We now study the case where the closed-loop is not saturated. One recalls that the unsaturated control is defined as

$$u - \omega + y - \frac{1}{\gamma}\left[k_{\mathrm{o}}\hat{x} + k_L\left(\hat{x} - x^{\mathrm{c}}\right) - k_P\left(\hat{x} - x^{\mathrm{sp}}\right)\right] \triangleq \Phi = 0 \tag{D.4}$$

D.1.2.1 Proof of the equivalence of the two conditions $\lambda_1 = 0$ and $\frac{\partial k_L}{\partial x} = 0$

The condition $\frac{\partial k_L}{\partial x} = 0$ can be rewritten under the equivalent form

$$0 = \left(\frac{\partial u}{\partial x} + \frac{\partial y}{\partial x}\right)\left(x^{\mathrm{sp}} - x^{\mathrm{c}}\right) + \left[\left(u - \omega + y\right) - k_{\mathrm{o}}x^{\mathrm{sp}}\right]\frac{\partial x^{\mathrm{c}}}{\partial x}$$

and, by exploiting the partial derivative of the feedback law, we get

$$0 = \frac{\partial u}{\partial x} + \frac{\partial y}{\partial x} + \frac{k_L}{\gamma}\frac{\partial x^{\mathrm{c}}}{\partial x}$$

then, using the definition of x^{c}, one obtains

$$k_L = \frac{k_{\mathrm{r}}y^2}{\omega}\left(1 + \frac{\dfrac{\partial u}{\partial x}}{\dfrac{\partial y}{\partial x}}\right)$$

and, finally

$$k_L = \frac{k_{\mathrm{r}}y^2}{\omega}\left(1 + \frac{\dfrac{\partial h_1}{\partial x} - \dfrac{\partial h_{21}}{\partial x} - \dfrac{\partial h_{22}}{\partial x}u - \dfrac{k_{\mathrm{o}}}{\gamma}}{\left(h_{22}(1+\alpha) - 1\right)\dfrac{\partial h_1}{\partial x} - \alpha\left(\dfrac{\partial h_{21}}{\partial x} + \dfrac{\partial h_{22}}{\partial x}u\right) - \alpha h_{22}\dfrac{k_{\mathrm{o}}}{\gamma}}\right) \tag{D.5}$$

On the other hand, the condition on λ_1 (eigenvalue of the closed-loop dynamics along the x axis), $\lambda_1 = 0$ can be rewritten, equivalently, with

$$f \triangleq \gamma\left(u + h_1(x,\omega) - h_{21}(x) - h_{22}(x)u - \omega\right) - k_{\mathrm{o}}x \tag{D.6}$$

and Φ defined in (D.4),

$$\begin{aligned}
0 &= \frac{\partial f}{\partial x} - \frac{\partial f}{\partial u}\left(\frac{\partial \Phi}{\partial u}\right)^{-1}\frac{\partial \Phi}{\partial x} \\
0 &= \left(1+\alpha\frac{\partial h_2}{\partial u}+\frac{k_L}{\gamma}\frac{\partial x^{\mathrm{c}}}{\partial u}\right)\frac{\partial f}{\partial x} - \frac{\partial f}{\partial u}\left(\frac{\partial h_1}{\partial x}+\alpha\frac{\partial h_2}{\partial x}+\frac{k_L}{\gamma}\frac{\partial x^{\mathrm{c}}}{\partial x}\right) \\
0 &= \frac{k_L\omega}{k_{\mathrm{r}}y^2}\left(\frac{\partial y}{\partial u}\frac{\partial f}{\partial x}-\frac{\partial f}{\partial u}\frac{\partial y}{\partial x}\right)-\left(1+\frac{\partial y}{\partial u}\right)\frac{\partial f}{\partial x}+\frac{\partial f}{\partial u}\frac{\partial y}{\partial x} \\
k_L &= \frac{k_{\mathrm{r}}y^2}{\omega}\frac{\left(1+\frac{\partial y}{\partial u}\right)\frac{\partial f}{\partial x}-\frac{\partial f}{\partial u}\frac{\partial y}{\partial x}}{\frac{\partial y}{\partial u}\frac{\partial f}{\partial x}-\frac{\partial f}{\partial u}\frac{\partial y}{\partial x}} = \frac{k_{\mathrm{r}}y^2}{\omega}\left(1+\frac{\frac{\partial f}{\partial x}}{\frac{\partial y}{\partial u}\frac{\partial f}{\partial x}-\frac{\partial f}{\partial u}\frac{\partial y}{\partial x}}\right)
\end{aligned}$$

and finally

$$k_L = \frac{k_{\mathrm{r}}y^2}{\omega}\left(1+\frac{\frac{\partial h_1}{\partial x}-\frac{\partial h_{21}}{\partial x}-\frac{\partial h_{22}}{\partial x}u-\frac{k_{\mathrm{o}}}{\gamma}}{(h_{22}(1+\alpha)-1)\frac{\partial h_1}{\partial x}-\alpha\left(\frac{\partial h_{21}}{\partial x}+\frac{\partial h_{22}}{\partial x}u\right)-\alpha h_{22}\frac{k_{\mathrm{o}}}{\gamma}}\right) \quad \text{(D.7)}$$

which is exactly (D.5).

The two conditions $\lambda_1 = 0$ and $\dfrac{\partial k_L}{\partial x} = 0$ are equivalent.

D.1.2.2 Solution of $\dfrac{\partial \Phi}{\partial u} = 0$

The condition $\dfrac{\partial \Phi}{\partial u} = 0$ can be rewritten, equivalently, as

$$\begin{aligned}
0 &= 1+\alpha\frac{\partial h_2}{\partial u}+\frac{k_L}{\gamma}\frac{\partial x^{\mathrm{c}}}{\partial u} \\
\text{then,}\quad k_L &= \frac{k_{\mathrm{r}}\bar{y}^2}{\omega}\left(1+\alpha+k_{\mathrm{a}}(1-\bar{x})/\gamma\right)
\end{aligned} \quad \text{(D.8)}$$

D.2 Stability analysis of the discrete-time closed-loop dynamics

One considers the following Euler explicit implementation in discrete time of the proposed feedback controller with the unsaturated control law:

$$
\begin{cases}
x_{k+1} = x_k + \Delta_t f(x_k, h(x_k, \omega_k, u_k), u_k, \omega_k) & \text{(D.9)} \\
\quad = x_k + \Delta_t \gamma \left(u_k + h_1\left(x_k, \omega_k\right) - h_2\left(x_k, u_k\right) - \omega_k\right) - k_{\mathrm{o}} x_k & \\
\hat{x}_{k+1} = \hat{x}_k + \Delta_t \ell(u_k, y_k(x_k, \omega_k, u_k), \hat{x}_k, \omega_k) & \\
\quad = \hat{x}_k + \Delta_t \left[\gamma \left(u_k + h_1\left(x_k, \omega_k\right) + \alpha h_2\left(x_k, u_k\right) - \omega_k\right) - k_{\mathrm{o}} \hat{x}_k\right. & \text{(D.10)} \\
\qquad \left. - k_L\left(\hat{x}_k - x_k^{\mathrm{c}}\right)\right] & \\
u_{k+1} = \omega_k - h_1(x_k, \omega_k) - \alpha h_2(x_k, u_k) & \text{(D.11)} \\
\qquad + \dfrac{1}{\gamma}\left(k_{\mathrm{o}} \hat{x}_{k+1} + k_L\left(\hat{x}_{k+1} - x_k^{\mathrm{c}}\right) - k_P\left(\hat{x}_{k+1} - x_k^{\mathrm{sp}}\right)\right) &
\end{cases}
$$

The corresponding Jacobian matrix is described as follows

$$
\begin{pmatrix}
J_{11} & J_{12} & J_{13} \\
J_{21} & J_{22} & J_{23} \\
J_{31} & J_{32} & J_{33}
\end{pmatrix} \tag{D.12}
$$

where

$$
\begin{cases}
J_{11} &= 1 + \Delta_t \dfrac{\partial f}{\partial x} \\
J_{12} &= 0 \\
J_{13} &= \Delta_t \dfrac{\partial f}{\partial u} \\
\\
J_{21} &= \Delta_t \dfrac{\partial \ell}{\partial x} \\
J_{22} &= 1 - \Delta_t \left(k_{\mathrm{o}} + k_L\right) \\
J_{23} &= \Delta_t \dfrac{\partial \ell}{\partial u} \\
\\
J_{31} &= -\dfrac{\partial \Phi}{\partial x} + \Delta_t \dfrac{\left(k_{\mathrm{o}} + k_L - k_P\right)}{\gamma} \dfrac{\partial \ell}{\partial x} \\
J_{32} &= \dfrac{\left(k_{\mathrm{o}} + k_L - k_P\right)}{\gamma}\left(1 - \Delta_t\left(k_{\mathrm{o}} + k_L\right)\right) \\
J_{33} &= 1 - \dfrac{\partial \Phi}{\partial u} + \Delta_t \dfrac{\left(k_{\mathrm{o}} + k_L - k_P\right)}{\gamma} \dfrac{\partial \ell}{\partial u}
\end{cases}
$$

Neglecting the effects of the observer convergence, under the assumption $\hat{x}_k = x_k^{\mathrm{sp}}$, we restrict our analysis to the necessary and sufficient condition for the reduced dynamics having the following matrix governing its discrete-time dynamics

$$
J = \begin{pmatrix} 1 + \epsilon c & \epsilon d \\ -b + \epsilon e & 1 - a + \epsilon q \end{pmatrix} = \begin{pmatrix} J_{11} & J_{13} \\ J_{31} & J_{33} \end{pmatrix} \tag{D.13}
$$

where $a = \dfrac{\partial \Phi}{\partial u}$, $b = \dfrac{\partial \Phi}{\partial x}$, $c = \dfrac{\partial f}{\partial x}$, $d = \dfrac{\partial f}{\partial u}$, $e = \dfrac{(k_o + k_L - k_P)}{\gamma}\dfrac{\partial \ell}{\partial x}$, $q = \dfrac{(k_o + k_L - k_P)}{\gamma}\dfrac{\partial \ell}{\partial u}$ and $\epsilon = \Delta_t$

This matrix could be studied using Jury's criterion of stability of discrete time dynamics. However, there exists a change of coordinates to put the previous matrix under triangular form. Thus

$$\begin{array}{l} \det|sI - J| \; = \\ \begin{vmatrix} s - (1 + \epsilon c - \beta(-b + \epsilon e)) & 0 \\ -(-b + \epsilon e) & s - (1 - a + \epsilon q + \beta(-b + \epsilon e)) \end{vmatrix} \end{array} \tag{D.14}$$

where β is defined by $\beta^2(-b + \epsilon e) - \beta(a + \epsilon(c - q)) - \epsilon d = 0$

$$\Rightarrow \left\{ \begin{array}{rcl} \beta & = & a + \epsilon(c - q) \pm \sqrt{\Delta_\beta} \\ \Delta_\beta & = & a^2 + 2a\epsilon\left(c - q - \dfrac{2bd}{a}\right) + \epsilon^2\left((c - q)^2 + 4ed\right) \\ & = & \left(a + \epsilon\left(c - q - \dfrac{2bd}{a}\right)\right)^2 + O(\epsilon^2) \end{array} \right. \tag{D.15}$$

As a result, the eigenvalues are

$$\left\{ \begin{array}{rcl} \tilde{\lambda}_1 & = & 1 - \epsilon c - \beta(-b + \epsilon e) \\ & = & 1 - a/2 + \epsilon c/2 + \epsilon q/2 + \sqrt{\Delta_\beta} \\ & = & \underbrace{1 + \epsilon\left(\dfrac{ca - db}{a}\right)}_{\text{dominant part}} + O(\epsilon^2) \\ \tilde{\lambda}_2 & = & 1 - a + \epsilon q - \beta(-b + \epsilon e) \\ & = & 1 - a/2 + \epsilon c/2 + \epsilon q/2 - \sqrt{\Delta_\beta} \\ & = & \underbrace{1 - a}_{\text{dominant part}} + \epsilon\left(\dfrac{qa - db}{a}\right) + O(\epsilon^2) \end{array} \right. \tag{D.16}$$

In conclusion, for $\Delta_t = \epsilon$ sufficiently small, the necessary and sufficient conditions of asymptotic stability are

$$\left\{ \begin{array}{rcl} |1 - a| & < & 1 \\ ca - db & < & 0 \end{array} \right. \tag{D.17}$$

Remark 1. $\tilde{\lambda}_1 = 1 + \Delta_t\left(\dfrac{ca - db}{a}\right) = 1 + \Delta_t\lambda_1$. The eigenvalue $\tilde{\lambda}_1$ of the discrete time dynamics evolves in the same way that the eigenvalue λ_1 of continuous dynamics.

Appendix E

Control of a SCR system using an inlet virtual NO_x sensor

As discussed earlier, an on-board inlet NO_x sensor is generally used to provide an accurate measurement of the inlet SCR NO_x value. However, the replacement of the upstream NO_x sensor by a virtual sensor still represents an important interest for car manufacturers in terms of system cost limitation, in particular in the case of light-duty vehicles (Dolanc et al. (2001), Hayat & Georgiadis (2012)). Whatever the method employed to get the NO_x concentration upstream of the SCR system, an accurate value of this concentration is necessary for the control of urea dosing. The accuracy of NO_x estimation is affected by modeling errors but also by uncertainties in the measurement or the estimation of the input variables of the models, due to sensors drifts. The measurement of NO_x concentration using a sensor is not perfect neither. The impact of a misevaluation of the upstream NO_x concentration on the SCR conversion efficiency has not been fully discussed so far. This issue is addressed in this Appendix.

In the sequel, the models used to estimate NO_x concentration upstream of the SCR system are presented following Quérel et al. (2012). Afterwards, a robustness analysis of the SCR control towards NO_x measurement or estimation errors is proposed (Quérel et al. (2013)). Finally, simulation results are presented which compare NO_x reduction efficiency achieved with and without upstream NO_x sensor and show the impact of a misevaluation of the upstream NO_x concentration on the SCR conversion efficiency.

E.1 NO_x estimation

In this section, the models used to predict NO_x emissions upstream of the SCR system are introduced. The first step consists in estimating engine-out NO_x emis-

sions. In steady state operating conditions, similar NO_x concentrations are measured upstream and downstream of the DOC (Hsieh & Wang (2011)). In a second step, NO_x concentration upstream of the SCR system is thus calculated from engine-out NO_x emissions by taking into account the exhaust gas transport dynamics.

E.1.1 Engine-out NO_x emissions modeling

A semi-physical mean value model proposed by Benz et al. (2011) is employed to estimate engine-out NO_x emissions. A detailed analysis of this model is proposed by Quérel et al. (2012). In stationary driving conditions, NO_x emissions NO_x^{ss} are obtained by a static map depending on engine speed N_e and torque set point Γ_e^{sp}:

$$NO_x^{ss} = f_{NO_x}(N_e, \Gamma_e^{sp}) \tag{E.1}$$

Then, NO_x concentrations are corrected to take into account air path and combustion phasing deviations from their static values:

$$NO_x^{cyl} = \gamma_{NO_x}\ NO_x^{ss}. \tag{E.2}$$

The correction factor γ_{NO_x} is calculated from the engine speed, the aspirated mass flow $\dot{m}_{in}$, the air fraction in the cylinder at Intake Valve Closing (IVC) x_{air} and the crank angle at which 50% of the injected fuel mass has been burned θ_{50}:

$$\gamma_{NO_x} = \left(\gamma_{\theta_{50}}\ {\gamma_{x_{air}}}^{\gamma_{x_{air}}+\beta_3}\right)^{\beta_5 ab} \tag{E.3}$$

where $a = \left(\dfrac{\gamma_{\theta_{50}}}{\gamma_{x_{air}}}\right)^{\beta_2\ \gamma_{\dot{m}_{in}}+\beta_1}$, $b = \dfrac{\gamma_{\theta_{50}}}{N_e} + \beta_4$ and γ_x represents the ratio of the actual values of the variable x to its static values stored in two-dimensional maps depending on engine speed and torque.

The aspirated mass flow is obtained from the temperature T_1 and the pressure p_1 measured in the intake manifold:

$$\dot{m}_{in} = \eta_v\left(N_e, p_1\right)\frac{p_1 V_d}{r\ T_1}\frac{N_e}{120}n_{cyl} \tag{E.4}$$

where V_d is the displaced volume, η_v the volumetric efficiency, r the gas constant and n_{cyl} the number of cylinders.

The air fraction in the cylinder at IVC is given by:

$$x_{air} = 1 - F_1, \tag{E.5}$$

The intake manifold Burned Gas Ratio (BGR) F_1 is not measured but an estimated value $\widehat{F}_1$ is obtained using a state observer (Chauvin et al. (2006)):

$$\begin{cases} \dot{\widehat{p}}_1 &= \frac{rT_1}{V_1}\left(\dot{m}_{air} + S_{egr}\dot{\widehat{\theta}}_{egr} - \eta_v \frac{V_d}{rT_1}\frac{N_e}{120}\widehat{p}_1\right) \\ & \quad - (l_1 - \eta_v)\frac{V_d}{V_1}\frac{N_e}{120}(\widehat{p}_1 - p_1) \\ \dot{\widehat{F}}_1 &= \frac{rT_1}{p_1 V_1}\left(F_2 S_{egr}\widehat{\theta}_{egr} - (\dot{m}_{air} + S_{egr}\widehat{\theta}_{egr})\widehat{F}_1\right) \\ \dot{\widehat{\theta}}_{egr} &= -l_3 \frac{rT_1}{V_1} S_{egr}(\widehat{p}_1 - p_1) \end{cases} \tag{E.6}$$

where V_1 is the intake manifold volume, F_2 the exhaust equivalence ratio, $\dot{m}_{air}$ the air mass flow, S_{egr} the EGR valve effective area and θ_{egr} the normalized EGR mass flow defined as the ratio between the EGR mass flow and the EGR valve effective area. l_1 and l_3 are the tunable observer gains.

θ_{50} is computed from a combustion analysis based on the measured instantaneous in-cylinder pressure (Heywood (1988)).

The coefficients β_i are calibration parameters learnt from experimental data. The values obtained for the diesel engine considered in this paper are given in Table E.1.

Table E.1: NO_x model parameters.

β_1	β_2	β_3	β_4	β_5
9.15	-7.67	-9.86	-0.04	-0.98

E.1.2 Exhaust gas dynamics modeling

NO_x concentration upstream of the SCR system is calculated from the engine-out NO_x concentration by taking into account the exhaust gas dynamics. The simplified approach presented by Ajtay (2005) is employed: the exhaust gas dynamics is modeled by a delayed first order filter, thus taking into account a perfect gas mixing and a transport delay.

E.2 Sensitivity analysis of the NO_x estimator

Whatever the measurement setup, NO_x concentration upstream of the SCR system is affected by uncertainties caused by sensors drifts. In this section, the dispersion in upstream NO_x concentration is evaluated. The accuracy of the NO_x sensor

is directly provided by the supplier and given in section 2.1.2. A sensitivity analysis of the NO_x model is done in order to evaluate the dispersion in estimated upstream NO_x concentration. The sensitivity analysis is performed using a statistical method based on Monte Carlo simulations. The goal is to evaluate the uncertainty in NO_x estimation due to uncertainties in the inputs and to determine the contribution of each input variable to the dispersion in NO_x concentration. The contribution of each input variable X_i to the dispersion of the model output Y is evaluated using the first order Sobol indices (Sobol (2001)) defined by:

$$S_i(Y) = \frac{V(E(Y|X_i))}{V(Y)} \tag{E.7}$$

where $E(Y)$ and $V(Y)$ are respectively the mean and variance of Y and $E(Y|X_i)$ is the conditional expectancy.

The application of the Monte Carlo method consists of four steps: i) the determination of the probability laws that characterize the dispersions in the inputs; ii) the generation of a sample for each input variable which is consistent with the corresponding probability law; iii) the simulation of the model with the generated samples; iv) the analysis of the output dispersion.

Table E.2: Sensor dispersions.

Variables	Standard deviation 3σ	Dispersion form
Air mass flow	6%	$\dot{m}_{air}^d = \dot{m}_{air}\,(1 + \delta\dot{m}_{air})$
Intake manifold pressure	23 mbar	$p_1^d = p_1 + \delta p_1$
Intake manifold temperature	10 K	$T_1^d = T_1 + \delta T_1$
Exhaust equivalence ratio	4%	$F_2^d = F_2\left(1 + \left(1 - \frac{1}{F_2}\right)\delta F_2\right)$
Volumetric efficiency	3%	$\eta_v^d = \eta_v + \delta\eta_v$
Middle of combustion	$1°V$	$\theta_{50}^d = \theta_{50} + \delta\theta_{50}$

Firstly, the uncertainties in the aspirated mass flow estimation using the model described in (E.4) as well as in the BGR estimation from the state observer (E.6) are determined. They are due to the dispersions in the measurement of $\dot{m}_{air}$, T_1, p_1 and F_2 and in the estimation of η_v. In this study, these dispersions are supposed to be Gaussian and the inputs are considered independent. The dispersions of

the sensors, given by the suppliers, are summarized in Table E.2. Secondly, the uncertainty in NO_x estimation (E.2), due to the dispersions in aspirated mass flow and BGR estimations, as well as in the calculation of θ_{50}, is evaluated. In this study, 3000 runs of the Monte-Carlo simulation have been performed.

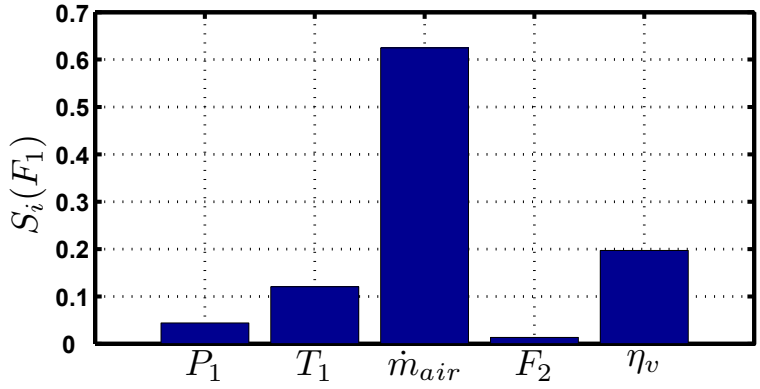

Figure E.1: Contribution of each input variable to F_1 estimation dispersion (BGR estimation dispersion).

The dispersions of the aspirated mass flow and the intake manifold composition are found to follow Gaussian distributions, with relative three standard deviations of 6% in the first case and absolute three standard deviations of 6% in the second case. The uncertainty in BGR estimation (E.6) is mainly due to the dispersion of the air mass flow sensor (see Figure E.1). The intake manifold burned gas ratio appears to be the most critical parameter for NO_x estimation (E.2). As the dispersion in

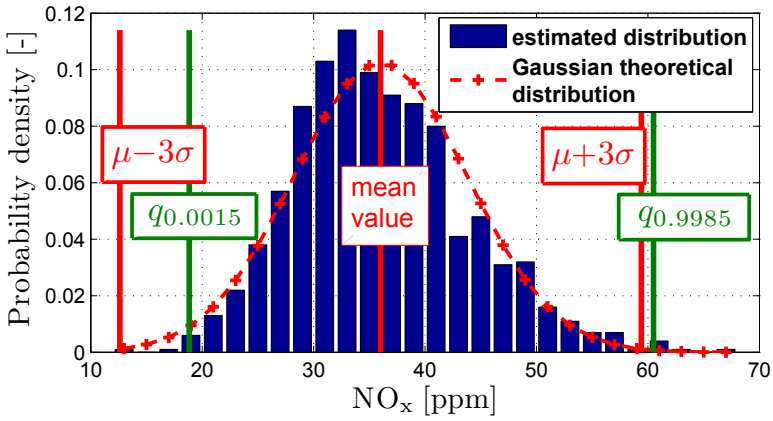

Figure E.2: Probability density of the estimated NO_x concentration. μ and q_a are the mean and the quantile of order a of the distribution, respectively.

NO_x estimation is not centered, an interval corresponding to a confidence level of 99.7% is given (refer to Figure E.2): an underestimation of 6% of the BGR leads to an overestimation of about 75% of the NO_x emissions whereas an overestimation of 6% of the BGR leads to an underestimation of about 50% of the NO_x emissions.

E.3 Simulation results

In this section, the robustness of the control strategy proposed in Chapter 3 to NO_x measurement or estimation errors is assessed in simulation. The controller consisting of (3.2), (3.3) and (3.4) is coupled with the SCR model (1.21) discretized into twenty equal parts. The real NO_x signal, measured with the upstream NO_x sensor, is always applied at the inlet of the model. The NO_x reduction efficiency is calculated from the real upstream NO_x concentration (measured) and the real downstream NO_x concentration (given by the SCR model). The robustness of the control strategy is assessed by dispersing the upstream NO_x concentration signal applied as input of the controller. The aim of this study is to determine the impact of NO_x measurement or estimation errors on the control of urea dosing and its consequence in terms of NO_x reduction efficiency. All the inputs of the model are experimental data obtained by performing a NEDC cycle with warm start on a roller test bench. The NO_x reduction efficiencies and the NH_3-slip resulting from the application of several dispersions on the NO_x input signal are exposed in Table E.3 and compared to the nominal case. The cases under consideration are:

- The dispersions in upstream NO_x concentration given by the sensor specifications (negative and positive);
- The dispersions of the estimator due to BGR variations, denoted ΔBGR (variation on $\hat{F}_1$), about: -6%, 0%, 4%, 5% and 6% (since NO_x estimation uncertainty has been shown to be essentially due to inaccuracy in BGR estimation $\hat{F}_1$).

In Figure E.3 are depicted the six upstream NO_x signals, used as inputs for the controller to test its robustness. On the one hand, the estimator presented in § E.1 without dispersion due to BGR variations gives an accurate prediction of the cumulative upstream NO_x concentration (estimation error: less than 2%, see Table E.3). On the other hand, applying BGR variations of $\pm 6\%$, results in large upstream NO_x concentration errors ($\Delta\text{BGR} = -6\% \Rightarrow \Delta NO_x = 77\%$ and $\Delta\text{BGR} = 6\% \Rightarrow \Delta NO_x = -48\%$). Nevertheless, an overestimation of upstream NO_x concentration can be compensated for by a fairly robust control law and the case of NO_x underestimation should be treated with more caution as depicted in Figure E.4.

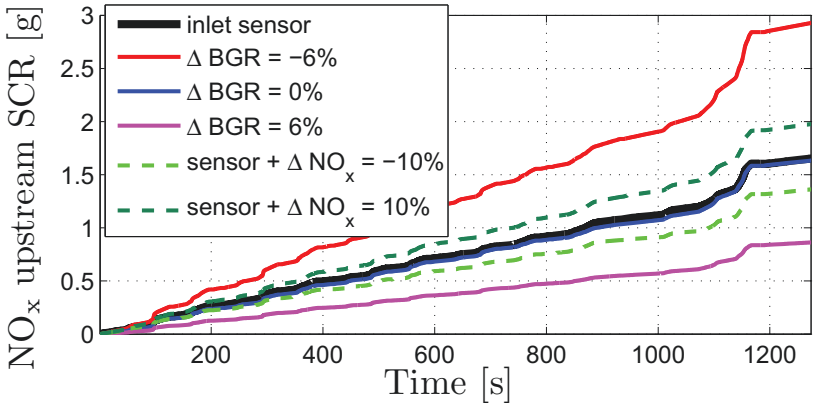

Figure E.3: Cumulative inlet NO_x emissions on a warm start NEDC cycle. The upstream NO_x concentration signal applied as input of the controller is replaced by dispersed values (model based estimate with dispersion and inlet NO_x sensor signal with dispersion). Simulation results.

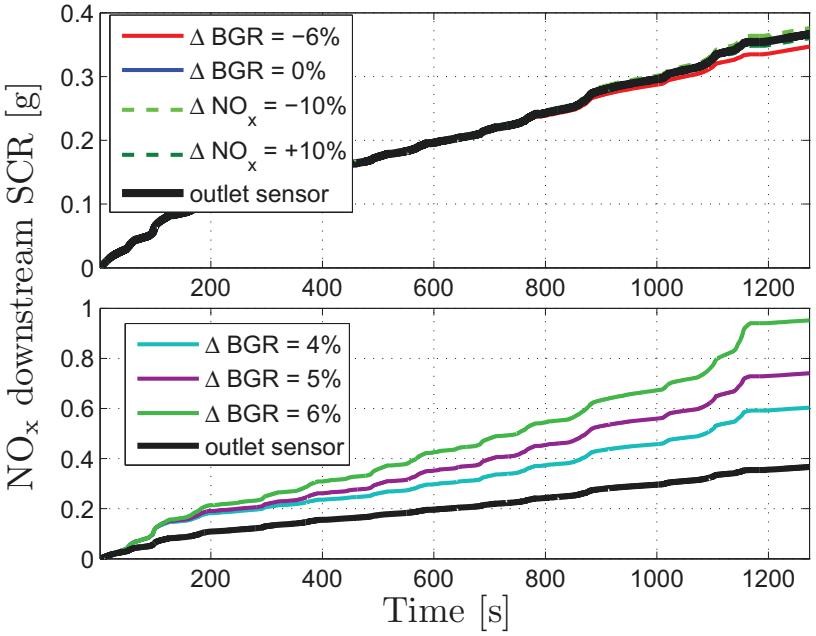

Figure E.4: Cumulative outlet NO_x emissions on a warm start NEDC cycle induced by dispersing the upstream NO_x concentration signal applied as input of the controller and compared to the nominal case. Based on the NO_x reduction efficiency, an overestimation of the NO_x concentration leads to a negligible variation on the proposed strategy performance while an underestimation of the concentration has a more critical impact. Simulation results.

When the NO_x sensor gives the NO_x upstream concentration, with or without dispersions, the efficiency of the SCR system is about 78% on the NEDC cycle. The results obtained in terms of NO_x reduction are almost equivalent when the virtual sensor is used to estimate the inlet NO_x concentration even with $\Delta BGR = -6\%$ (overestimation of the real concentration). This robustness can be explained by the large NH_3 adsorption capacity of the SCR catalyst which allows to sufficiently reduce the amount of NO_x, while maintaining release of NH_3 within acceptable levels. However, the underestimation of inlet NO_x concentration is more challenging

Table E.3: NO_x reduction efficiency and NH_3-slip during the NEDC cycle, depending on dispersions of the NO_x upstream signal applied as input of the controller. The NO_x inlet value of the model is always 150 ppm.

		inlet NO_x [mg/km]	outlet NO_x [mg/km]	NO_x reduction efficiency [%]	outlet NH_3 [ppm]	
					average	peaks
	ΔNO_x					
NO_x sensor	10%	178	32	78	< 1	7
	0%	150	33	78	< 1	6
	-10%	124	34	77	< 1	6
	ΔBGR					
NO_x estimation	-6%	266	31	79	2	23
	0%	148	33	78	< 1	6
	4%	98	55	63	< 1	3
	5%	88	67	55	< 1	1
	6%	79	87	42	< 1	< 1

for control. Indeed, in this case the controller performance degrades rapidly but is still acceptable until BGR variations of about 4%. Starting from $\Delta BGR = 5\%$, the estimation error of inlet NO_x is greater than 42% and the NO_x reduction efficiency is about 55%. Under these conditions, the NH_3-slip detection mechanism is activated regularly and incorrectly (this is specific to the proposed control strategy). This leads to NH_3 injection cut off on a large part of the cycle. *The critical point not to be exceeded corresponds to an inlet estimation of 50%* of the real value, and a *NO_x reduction efficiency of 50%* (the upstream and downstream NO_x signals are then equal from the controller point of view). This is a very pessimistic scenario.

Finally, with an Euro 5 calibrated engine (NO_x emissions < 180 mg/km), replacing the upstream measurement by a virtual sensor, requires a specific accuracy of the air path sensors to meet NO_x emission standards. Indeed, getting a sufficient efficiency of NO_x reduction by coupling this upstream estimation and this control

strategy requires an accuracy on the BGR value of ±4%. Based on the sensitivity analysis of the NO_x model proposed in this study, one can consider necessary to have an aspirated mass flow with a relative three standard deviations of 4%.

This robustness analysis of the controller toward NO_x measurement or estimation errors leads to give the required accuracy of the air path sensors in the perspective of replacing the upstream NO_x measurement by a virtual sensor and thus reduce the production costs of the vehicles. In the future, these simulations have to be validated experimentally. Furthermore, knowing the maximal NO_x uncertainties induced by the virtual sensor, it would be interesting to determine the engine calibration minimizing the particles emissions (moving the trade off NO_x/particles) while meeting NO_x emission standards.

Commande expérimentale en boucle fermée des systèmes SCR en utilisant des sondes à NO_x sensibles au NH_3

Résumé : Le problème étudié dans cette thèse est la commande en boucle fermée d'un système SCR (Réduction Sélective Catalytique) par l'urée tel qu'utilisé dans les systèmes de dépollution des gaz d'échappement des moteurs diesel automobiles. Une première contribution du manuscrit est en un modèle détaillé de la SCR, soulignant de la nature distribuée (1D) du système considéré, et plusieurs réductions successives de ce modèle de simulation conduisant à un modèle plus simple, utilisable à des f ns de synthèse de contrôleur. Une seconde contribution consiste à prendre en compte la sensibilité au NH_3 du capteur de NO_x utilisé pour la rétroaction lors du développement d'algorithmes de commande (observateur d'état, boucle de rétroaction, séquencement de gain, interprétation du signal capteur). L'observateur-contrôleur présenté possède plusieurs points d'équilibre dues à la sensibilité du capteur de sortie. On montre que seul le point d'intérêt pratique est asymptotiquement stable, les autres étant instables naturellement, rendus instables par une implémentation spécif que ou aisément détectés comme indésirables. Ces deux contributions ont été testées expérimentalement et validées. En résumé, la méthode de contrôle proposée dans cette thèse permet, à partir d'un moteur conforme aux exigences Euro 5 et avec une procédure de pré-conditionnement du catalyseur, de satisfaire la norme Euro 6.

Mots clés : Commande en boucle fermée, observateur, émissions automobiles, moteur diesel, Réduction Sélective Catalytique par l'urée, sonde à NO_x, sensibilité croisée.

Experimental closed-loop control of SCR systems using NO_x sensors cross-sensitive to NH_3

Abstract: The problem studied in this thesis is the closed-loop control of a urea-SCR (urea Selective Catalytic Reduction) as used in aftertreatment systems of diesel vehicles. A f rst contribution of the thesis is a detailed model for the SCR, highlighting the distributed (1D) nature of the considered system, and several successive reductions of this simulation model leading to a simpler one, better-suited for control design purposes. A second contribution consists in considering the sensitivity to NH_3 of the NO_x sensor used in a feedback loop, in the development of the control algorithms (state observer, feedback, gain scheduling, measurement interpretation). The ambiguity of the output measurement could be detrimental to the closed loop response, as it generates multiple equilibrium points (artefacts), besides the point of practical interest. A study of the closed-loop dynamics is performed in the vicinity of each point, which shows that the closed loop system naturally converges to the point of interest not to the artefacts. Both contributions have been tested and validated experimentally. In summary, the method proposed in this thesis might allow an engine equipped with Euro 5 hardware to satisfy Euro 6 standard using a preconditioning procedure of the catalyst.

Keywords: Closed-loop control, observer, automotive emissions, diesel engine, urea Selective Catalytic Reduction, NO_x sensor, Cross-sensitivity.

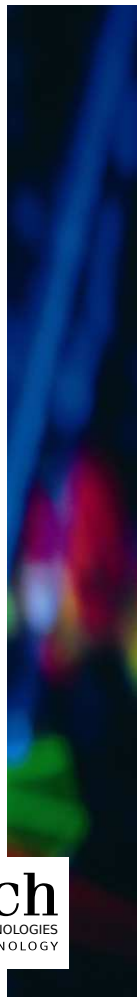

MINES ParisTech

ParisTech
INSTITUT DES SCIENCES ET TECHNOLOGIES
PARIS INSTITUTE OF TECHNOLOGY